Università
degli Studi
di Catania

Dottorato di Ricerca in Scienza
dei Materiali XXV Ciclo
2009-2012

New Strategies for the Synthesis of 2D Nanomaterials

Marco Giovanni Sinatra

Tutor:
Chiar.mo Prof. G. Compagnini

Coordinatore:
Chiar.mo Prof. A. Licciardello

CONTENTS

INTRODUCTION

In the past decade, the interest in nanoscale materials had an enormous impact and industrial potential deriving from the fact that new properties are acquired at this length scale and also these properties change whit their size or shape. Future progress could change our advances to assembling, communications technology and electronics, making previous technology redundant and leading to applications which could not have been developed or even thought about, without this new approach.

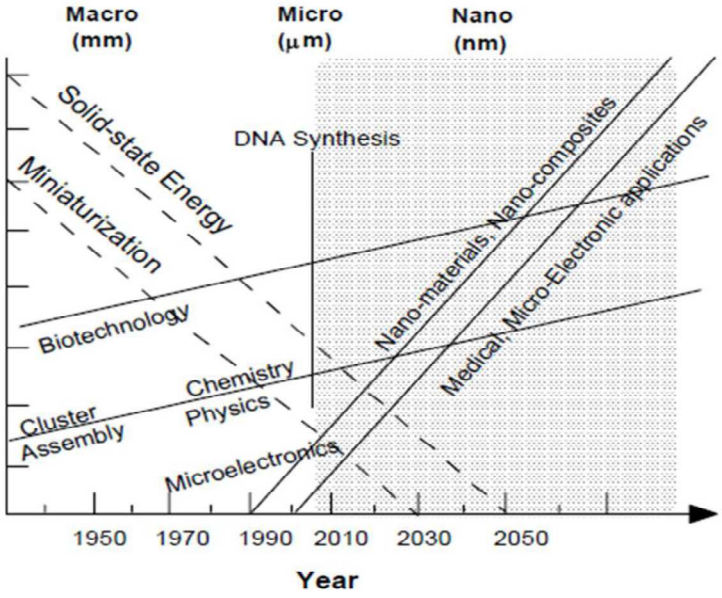

Figure 1. Trend of the miniaturization in the years

A nanostructured material is defined as a solid material characterized by at least one dimension in the nanometer range. Size effects establish an exceptional and intriguing aspect of nanomaterials.

The effects determined by size are part of the evolution of structural, electronic, electromagnetic, spectroscopic, thermodynamic and chemical features of these restricted systems with changing size. The properties of a material are based on the type of movement its electrons can perform, which depends on the space available for them. Therefore, the properties of a material are identified by a specific "length scale", commonly on the nanometer dimension. If the physical size of the material is decreased below this length scale, its properties change and become sensitive to size and shape. In any material, considerable modification of intrinsic optical and electrical properties with decreased size will be noticed when the energy spacing between the electronic levels is superior to the thermal energy (kT). For instance, in the bulk material, the electronic energy levels are continuous while in nanomaterials are discrete (finite density of states), and this behavior is due to the confinement of the electronic wave function to the physical dimensions of the particles. This phenomenon is called *quantum confinement* and therefore nanocrystals are also referred to as **quantum dots (QDs)**. Moreover, nanocrystals presents a high surface area and a large percentage of the atoms in this material is on its surface. Since this percentage depends considerably on the size of the particle, it can give rise to size effects in physical and chemical properties of this material.

When we talk about nanomaterials we indicate a substance with an extreme small size, at least one dimension 100 nm or less. Nanomaterials can be classified in zero dimensional as quantum dots, one dimensional as MoSI nanowires or polyynes, two dimensional, as MoS_2 sheets or carbon nanowalls, or three dimensional as metallic colloids.

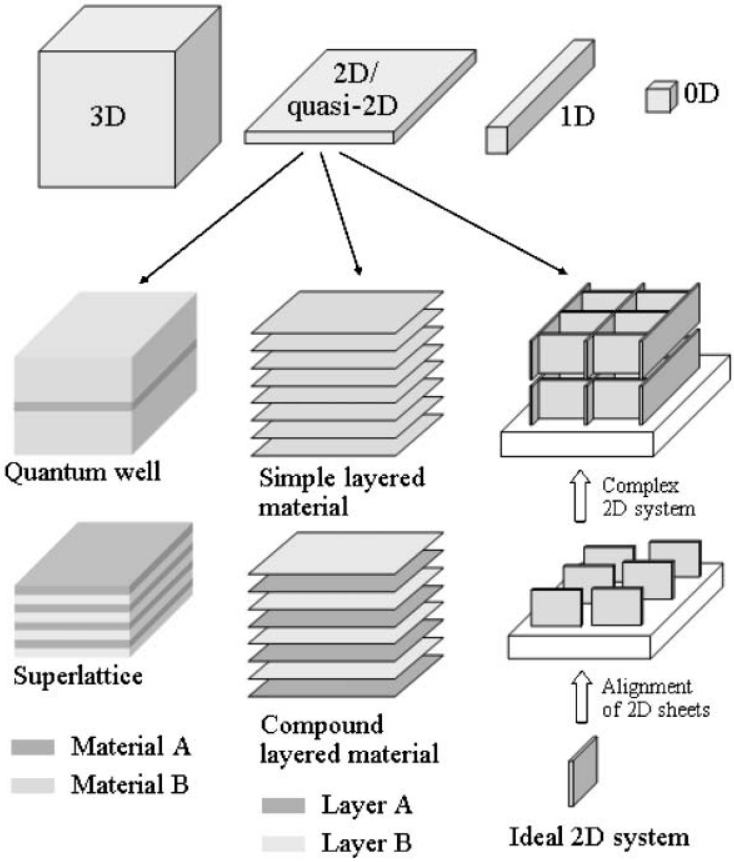

Figure 2. Classification of Nanomaterials (a) 0D spheres and clusters, (b) 1D nanofibers, wires, and rods, (c) 2D films, plates, and networks, (d) 3D nanomaterials. [1]

These materials have aroused a high interest in the last years by advantage of their singular electrical, optical, mechanical and magnetic properties. Following will be shown some examples of these nanomaterials:

For instance, nanophase ceramics are very interesting because they are more ductile at elevated temperatures as compared to the coarse-grained ceramics. Another example is nanostructured semiconductors. These materials present various non-linear optical properties and can be used as windows layers in solar cells. Semiconductor Q-particles also exhibit quantum confinement effects which may cause to particular properties, for instance silicon germanium quantum dots as infrared optoelectronic devices and the photoluminescence in MoS_2 monolayers deposited on silicon substrate.

Nanostructured metal colloids could play a fundamental role in catalytic applications. Their substantial advantages are about activity, selectivity and lifetime in chemical transformations and electrocatalysis (fuel cells). Enantioselective catalysis was also achieved using chiral modifiers on the surface of nanoscale metal particles [2].

In literature many different kind of synthesis are present. In particular the science community adopted two different approaches to produce nanomaterials, top-down and bottom up methods.

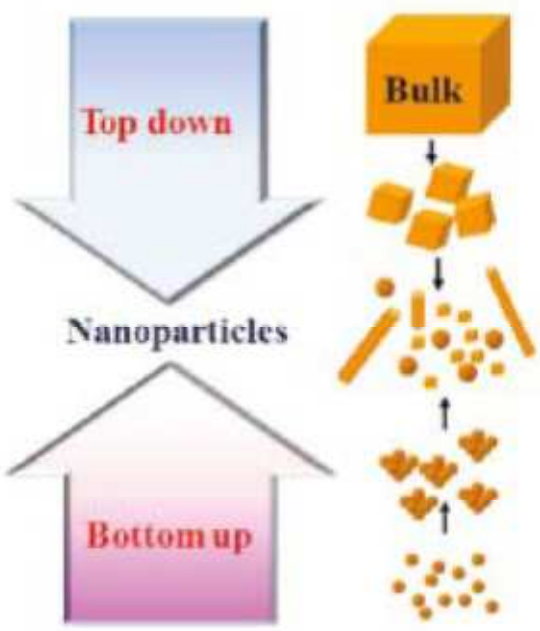

Figure 3. Outline of top down/bottom up approaches

In figure 3 I reported the outline of top down bottom up approaches. In practice, these two methods may be considered as a different ways of thinking. In particular top-down is estimated as a mode of analysis or decomposition, while bottom-up is considered as a kind of synthesis.

A top-down approach is fundamentally the breaking down of a system, commonly called bulk material, to obtain information about the system composition. With this method we can define an overview of the system, acquiring specific details about first-level subsystems. After that, each subsystem is analyzed in greater detail until the entire bulk material is reduced to base elements. One of the most important example of this approach is represented by the scotch tape exfoliation of graphene.

It consists in a piling off of graphite in order to reduce its thickness and split graphite crystals into increasingly thinner pieces to produce graphene's layers. [3] A bottom-up approach is the assembling together of the base elements, usually called building blocks, to create the nanostructure. The nanomaterial features shall be laid before the synthesis and in this way we can lead the growth in order to obtain a particular nanostructure with a specific property. The synthesis by laser ablation in liquid, for instance, is an example of this type of approach. It consists by irradiating a solid target submerged in a liquid with a laser beam. During this phenomena it's generated a plasma in which there are some reactive species. The interaction of these species with each other forms some new nanomaterial. For instance metal colloids are produced by laser ablation in water. [4]

In this thesis I'm going to report the obtained results during my PhD experience. I was able to synthesize some kinds of 2D nanomaterials by using new strategies for their synthesis. In particular I used pulsed laser ablation in liquid (PLAL) to synthesize nanostructures made of MoS_2 with a particular structure fullerene-like and I produced MoS_2 few-layers materials by applying mechanical exfoliation of MoS_2 powder assisted by ultrasonic treatments. Using PLAL and applying an electric field after the synthesis process I was able to produce a new and interesting carbon-based nanostructure called Carbon Nanowalls (CNWs) made of vertically oriented graphene sheets on a substrate. I have also produced a hybrid 2D composite by mixing MoSI nanowires with gold nanoparticles and I have studied the chemical bonding state of this interaction by using

of X-Ray Photoelectron Spectroscopy (XPS). Moreover I have studied the spectroscopy, morphology and chemical bonding features of all nanostructures obtained. I used following techniques as Raman spectroscopy, UV-VIS spectroscopy, Atomic Force Microscopy (AFM), Scanning/Transmission Electron Microscopy (SEM/TEM) and the aforementioned XPS.

During the next chapter, I'm going to describe the standard synthesis methods and the main properties and application of 2D nanostructures, which I have studied during my experience, and after that I'm going to show you my experimental work and my experimental results.

1 SYNTHESIS AND PROPERTIES OF TWO DIMENSIONAL NANOMATERIALS AND RELATED STRUCTURES: STATE OF THE ART

As said before, during my PhD experience, I focused my attention on the new strategies for the synthesis of 2D nanomaterials in order to improve the standard synthesis routes. Indeed, usually, to create a nanostructure we need, or to work under vacuum and at high temperature or to employ some reactants which we have to remove after the synthesis. In this chapter I'm going to show you some different standard synthesis routes to produce nanomaterials as MoS_2 fullerene-like or carbon nanowalls.

First I'm going to analyze synthesis properties and application of molybdenum disulphide nanomaterials after that I will discuss the case of carbon nanowalls and in the end of this chapter I will focus my attention on the manufacturing of conductive nano-network made of MoSI functionalized with gold nanoparticles.

1.1 MOLYBDENUM DISULPHIDE NANOMATERIALS

The dimension of an object is one of the most important material parameters; the same chemical compound could manifest impressively different properties depending on if it is organized in a 0D, 1D, 2D, or 3D crystal structure. Materials with layered structures continue a broadly studied topic in actual chemistry and physics. Most of the auspicious technological applications even though attend to intercalation compounds of layers materials. The transition metal dichalcogenides manifest appreciable multiplicity in their physical properties, from the fields of metals, to semiconductors, insulator and superconductors. A significant characteristic of these materials is that they crystallize in a quasi two-dimensional type of layered structure that gives considerable anisotropy to many of their properties. In addition, the layered structure of MoS_2 is very similar to graphite structure. This particular aspect allows to synthesize fullerene-like structures and nanotubes from inorganic compounds with a crystal structure akin to graphite.

Nanoparticles of compounds with a layered structure go under the large surface energy correlated with the external atoms and fold into hollow cage-like structures. To get over the large elastic energy associated with the folding process, considerable activation energy must be supported for the process to take place, otherwise the reaction is very slow. [5]

1.1.1 MoS_2 FULLERENE-LIKE

The fullerenes, among nanophase materials, take up a special place, first because they presents high symmetry and have an unique hollow-cage topologies. The predisposition of graphite nanoclusters to form the C_{60} molecule (see Figure 4) has been ascribed to the large surface energy of the external sp^2 bonded carbon atoms. Adding rings composed to five atoms into the hexagonal network structure of graphite it's induced bending and strain into the structure.

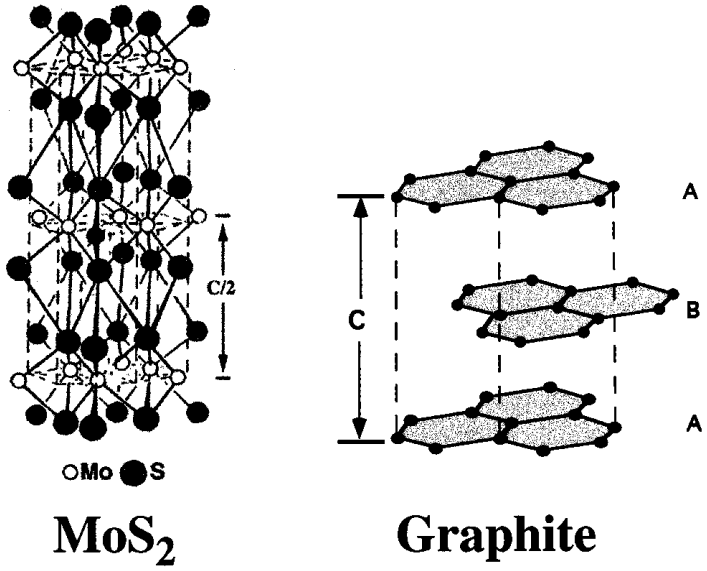

Figure 4. Schematic structures of graphite and MoS_2 nanoclusters. Note that in both cases the surface energy, that weakens the planar topology of the structure, is concentrated in the edge planes parallel to the c-axis (|| c).

The great stability of the C_{60} molecule (Figure 5) was attributed to the fact that this is the smallest carbon cluster with twelve disjoint pentagons [6].

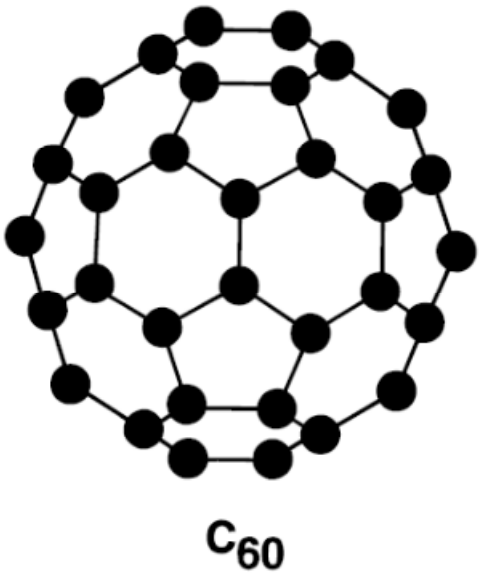

Figure 5. Schematic structures of the C_{60} molecule

Earlier than the discovery of the C_{60} molecule, Iijima et al. [7] proposed that carbon "onions" (see Figure 6A) are composed of various carbon cages, each with 12 pentagonal rings disposed in the carbon hexagonal (graphite) network.

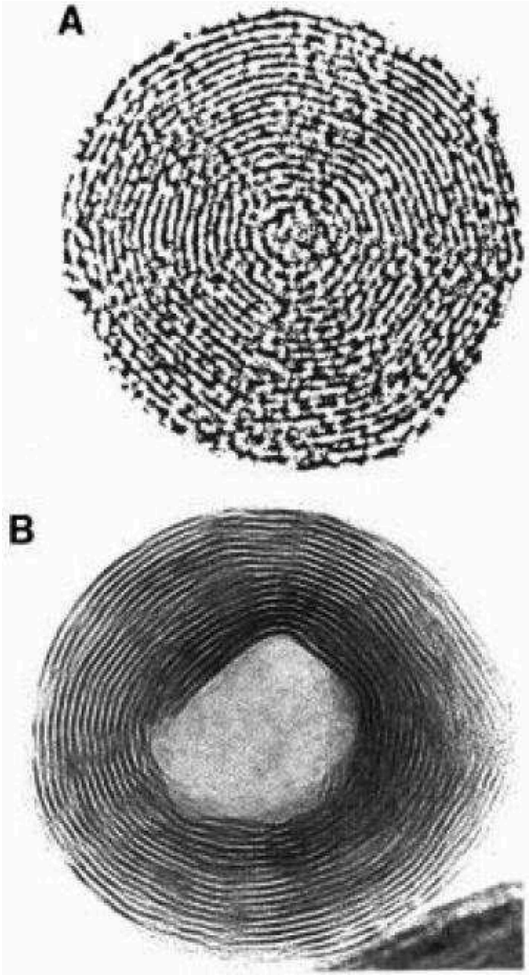

Figure 6. Transmission Electron images of (A) carbon fullerene and (B) MoS_2 fullerene-like

Similarly to graphite, layered compounds like MoS_2, do not exhibit dangling bonds on the basal (0001) plane ($\perp$c), that establishes itself with very inert and low energy (0001) surface (Figure 4). On the contrary, the

dangling bonds of the prismatic face perpendicular to the basal plane (|| c), are very reactive. Therefore, nanoclusters of 2-D materials have high percentage of their atoms on the prismatic edges with unsaturated bonds and this aspect gives them an instability in the planar structure. Accordingly, these materials form hollow-cage nanostructures without dangling bonds. This analogy between carbon and 2-D (layered) compounds was indicated first for WS_2 nanoclusters [8] and later for MoS_2 [9-10-11].

These materials are very important for their interesting properties. For instance MoS_2 is one of the most important solid lubricants and this characteristic is enhanced by the nanosize [12].

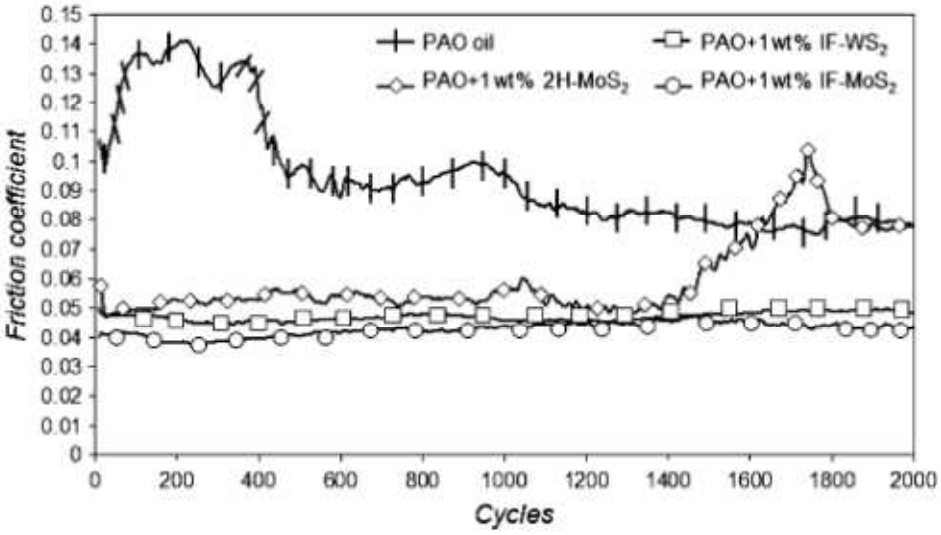

Figure 7. Comparison of the friction coefficient behavior among different lubricants.

It's possible to notice in the figure 7 that the friction coefficient of a commercial oil (PAO) with or without the additive is different. In particular by comparing the behavior of PAO with MoS_2 as bulk material and MoS_2 as fullerene.like (IF MoS_2), we can notice that the friction coefficient is better in the case of PAO with IF MoS_2.

In analogy to carbon fullerenes, the main reason of the formation of hollow cage structures of these compounds is due to the dangling bonds on the prismatic face (|| c) of the metal dichalcogenide (MX_2) nanocluster (Figure 5). The deflections from planarity of the nanocluster during the formation of a hollow cage structure is due to the elastic strain involved in tilting the chemical bonds. Therefore, a source of energy input increase the yield of the synthesis of inorganic fullerenes [13]. Different kinds of synthesis were adopted for the formation of hollow closed structures from layered compounds. It's possible to divide into two kinds of procedures: (a) synthetic procedures that arise far from equilibrium, and (b) synthetic procedures that are near to equilibrium conditions. The most commonly synthesis used to production these materials is not very different from the gas-phase reaction. This method is a progressively sulphurization of MoO_3 in gas phase [5]. The procedure is described by Tenne et al. in one of their more relevant work: "Molybdenum oxide is volatile under reducing conditions >700 °C, and hence a gas-phase reaction was adopted for the synthesis of IF-MoS_2. Typically, a 30-mg portion of MoO_3 powder (>99% pure) is heated (>800 °C) and is slowly reduced to MoO_{3-x} by a stream of forming gas (typically 5%H_2/95%N_2). The suboxide sublimes and effuses out of a nozzle where it crosses a

stream of H_2S gas mixed with a forming gas. The reaction products are collected on a quartz scepter, which is positioned 3 cm away from the crossing point of the two gas streams and is maintained at the same temperature (>800 °C). The collected nanoparticles are progressively converted into nested IF polyhedra within 30 min of firing time. The average size of the oxide nanoparticle and the ensuing IF-MoS_2 increases with temperature. It was found that at >900 °C, platelets with the 2H-MoS_2 structure abound and become the sole product at >950 °C."

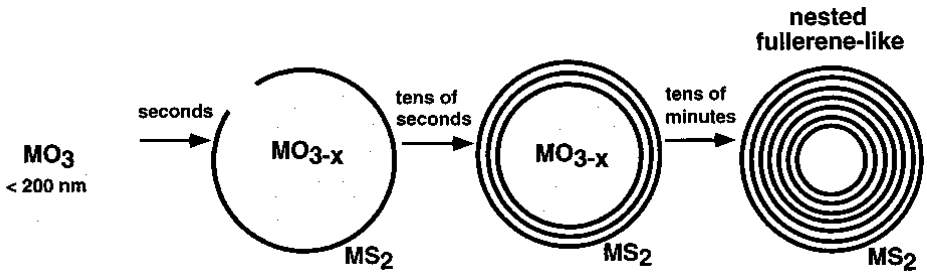

Figure 8. Scheme of the growth model of the inorganic fullerene-like from oxide nanoparticles.

The growth mechanism of quasi-spherical nested nanoparticles is reported in Figure 8. In the first moment of the reaction, the molybdenum oxide nanoparticle reacts with H_2S gas, which conducts to the growth of a complete sulfide shell composed of one or two MoS_2 atomic layers absorbing the entire oxide nanoparticle. This sulfide shell isolates the nanoparticle from its nearest neighbors thereby prohibiting coalescence

of the nanoparticles, which would lead to the formation of 2H-MS_2 platelets. Within more or less a minute, hydrogen diffusion into the nanoparticles (and oxygen out diffusion) allows to reduction of the oxide core and permits the formation of crystallographic plans. In the second part of the reaction, which can carry on 120 min and even more, sulfur diffuses slowly into the core of the nanoparticle and slowly converts the sub-oxide into sulfide, which becomes hollow at the end of the process. This synthesis actually consists of two independent processes. The rapid radial diffusion of sulfur atoms inward through dislocation at the outer MoS_2 layers and the slow diffusion of the sulfur atoms along the layers into the single-growth front of the sulfide. This process provides a continuous MoS_2 shell that grows inward into the oxide core.

The main problem of this synthesis is the need to work under vacuum with high temperature and, primarily, the presence of dangerous gas reagents like H_2S and H_2. For this reason I decided to develop a new synthesis route, for MoS_2 fullerene-like, in order to work in a safer, cheaper and faster way by using the PLAL.

1.1.2 MoS_2 MONOLAYERS

Another important bi-dimensional nanostructure of MoS_2 is represented by mono-layer material. Recent developments in synthesis of ultrathin layered materials in monolayer thickness have allowed examinations of new low-dimensional physics, as demonstrated by massless Dirac fermions and anomalous quantum Hall effects observed in monolayer graphene [14]. Layered transition metal dichalcogenides, like MoS_2, are another kind of materials, in which the interactions of the d-electrons' can produce to new physical phenomena. This material is composed of covalently bonded S-Mo-S sheets that interact each other by weak van der Waals forces. Molybdenum disulphide, like bulk material, is a semiconductor with an indirect bandgap of about 1eV and it has been employed for photocatalytic and photovoltaic applications due the high absorption in the solar spectrum region. Optical properties and quantum confinement effects on the electronic structure of MoS_2 have well known and noticed in MoS_2 thin films as well as in MoS_2 nanoplates and nanotubes [15]. In particular Splendiani et al. [16] report the emergence of photoluminescence in ultrathin layers of MoS_2. They founded that MoS_2 photoluminescence, increased with decreasing layer thickness, and that luminescence from a monolayer was the strongest while it was absent in bulk material. The cause of this luminescence behavior is due to the fact that MoS_2 change into a direct bandgap semiconductor when thinned to a monolayer.

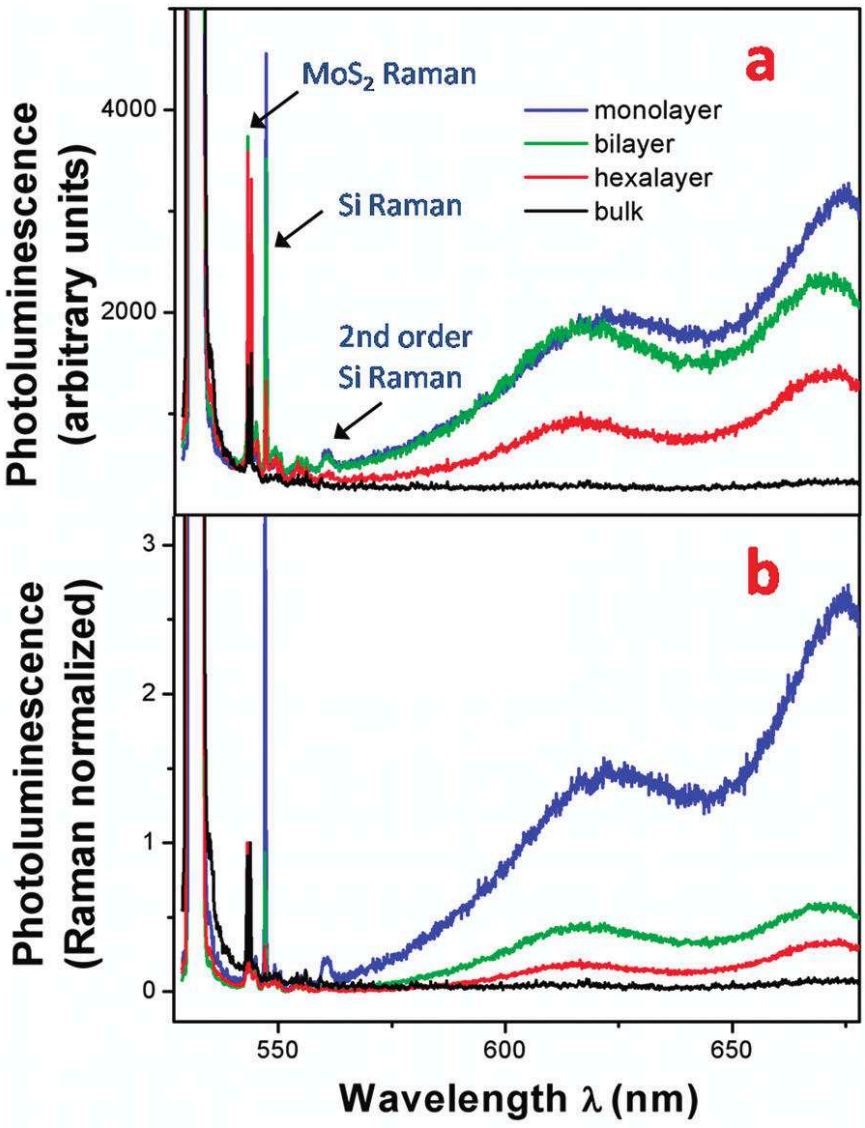

Figure 9. Photoluminescence and Raman spectra of MoS_2 monolayer, bilayer, hexalayer, and bulk sample.

In Figure 9a, it's reported photoluminescence spectra from monolayer, bilayer, hexalayer, and bulk MoS_2. In bulk MoS_2, no photoluminescence is present while for MoS_2 monolayers the Raman and photoluminescence intensities show a dependence from the layer: MoS_2 Raman signal is weaker in the monolayer MoS_2, due to lower quantity of material, than in the bulk material, while photoluminescence is higher regardless of the reduced amount of material. For this reasons MoS_2 monolayer photoluminescence is due to an intrinsic material property while the luminescence resonances is attributable to the direct excitonic transitions. For this reason the exfoliation methods, to produce two dimensional crystals, whose present interesting properties for different application like energy storage and electronics, are under investigation. These exfoliations can be divided in two different approaches: first mechanical method, like for instance scotch tape, that produces a small amount of layers, as reported in the figure 10 [17]

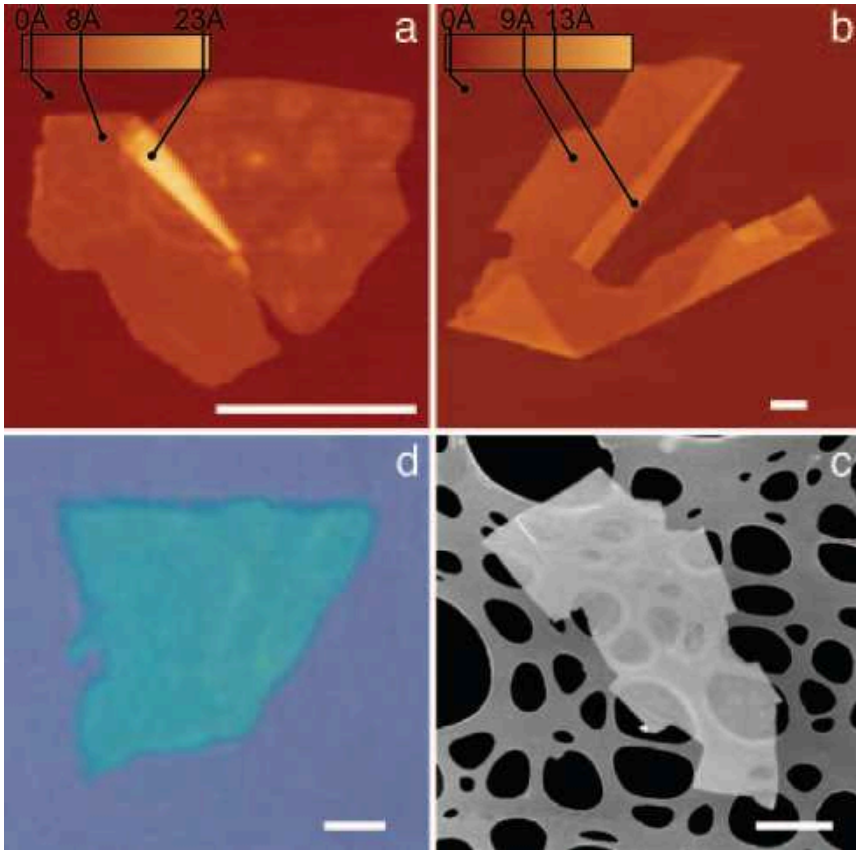

Figure 10. Scanning electron and atomic force images of 2D crystal matter

and second liquid-phase exfoliation methods would allow the formation of higher amount of material and the production of novel hybrid and composite materials [18].

Coleman et al. have exfoliated different kinds of two dimensional materials in a novel liquid-phase method using different common solvents. First they dispersed bulk material in a solvent by sonication and after that they centrifugated the sample in order to remove the bulk

materials from the dispersed one. Some of the more promising solvents were Nmethyl-pyrrolidone (NMP) and isopropanol (IPA) and the improvement of the exfoliation procedure gave concentrations as high as 0.3 mg/ml for MoS_2. This method allowed to prepare films of BN, MoS_2, and WS_2 by vacuum filtration or spraying, with thickness ranging from a few nanometers to hundreds of micrometers. To verified what they produced Coleman et al. made different kinds of analysis reported in figure 11. They used scanning electron and helium ion microscopy of the surface and edges of these films (Fig. 11, B and C).

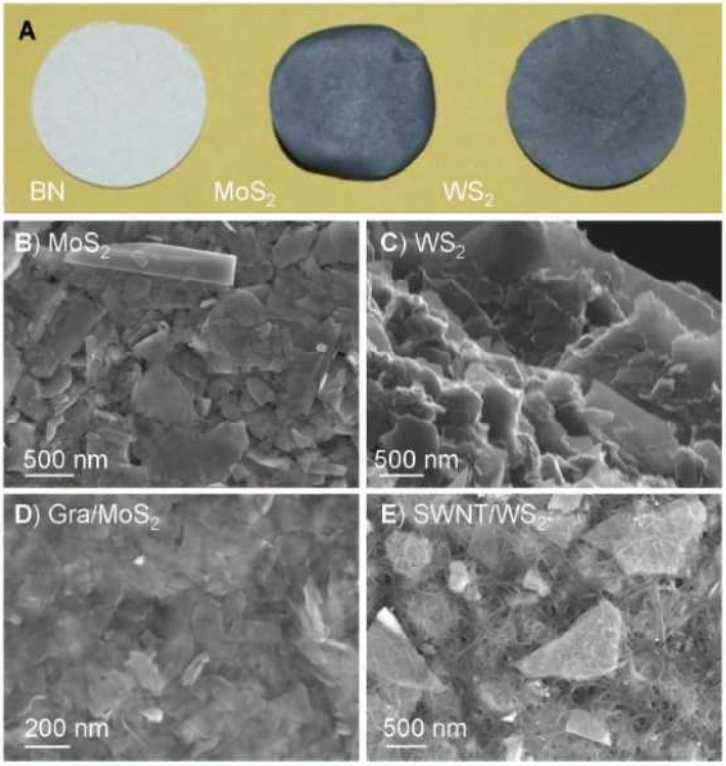

Figure 11. Pictures of different produced materials

They illustrated this by preparing hybrid dispersions and so films of MoS_2 or WS_2 mixed with graphene or single-walled nanotubes (SWNTs) (Fig. 11, D and E).

I decided to perform the same procedure to exfoliate MoS_2 but I tried to change solvent by the using of water and a surfactant. It was necessary to prevent the re-aggregation of the layer after the sonication. Furthermore I employed the centrifugation procedure to maximize the process yield.

1.2 CARBON BASED NANOMATERIALS

The discovery of graphene has stimulated enormous interest on 2D carbon nanostructure in view of their extraordinary properties and potential applications [19]. A challenge has always been to identify a high yield production pathway, suitable to give graphene or graphene-like structures without collateral structural damage and with the possibility to manipulate the layers (individually or collectively) in order to have a particular arrangement and position for given applications [20]. Alternative to single layer graphenes, the so called carbon nanowalls (CNWs) have been discovered and investigated [21]. They consist of aligned graphene sheets standing on a substrate with large surface areas and sharp edges. For these reasons they are expected to be good catalyst support structures for fuel cells as well as electron field emitters for lithium ion batteries. So far, research groups have explored different synthesis methods of CNWs essentially based on plasma-enhanced chemical vapour deposition approaches [22].

1.2.1 CARBON NANOWALLS:

The first paper, on the preparation of two-dimensional carbon nanostructures, was wrote more than 10 years. Ando et al. [23] found something like “carbon roses” during the synthesis of carbon nanotubes in 1997. In 2002, Wu et al. [24] reported the formation of two-dimensional carbon nanostructures, “carbon nanowalls,” growing vertically on catalyzed substrates. In figure 12 [25] it’s reported a scheme of Carbon nanowalls structures in order to give an understanding of the organization of the layers.

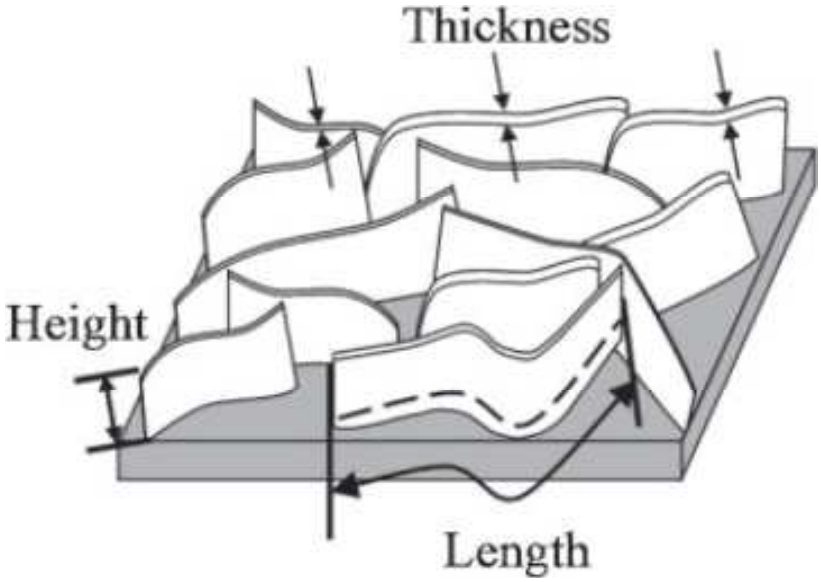

Figure 12. Schematic structure of Carbon Nanowalls grown on a substrate

This material shows a very interesting properties in many field like field emission, catalysis and electrochemical applications. For instance CNWs decorated with Pt nanoparticles have shown good electrocatalytic properties as reported in the work of Giorgi et al. [26]. They noticed that enhanced activity for methanol oxidation was not linked to the increase of platinum load and specific surface area, but rather it was depended from the microstructure of the Pt cluster at level of nanoparticles (<10 nm). The carbon nanowalls structures acted as a good substrate for Pt electrocatalyst for methanol oxidation with a remarkable enhancement respect to the state of art carbon powder.

Another important application of these systems is the formation of 3D field emission array as reported by Stratakis et al. [27]. They noticed that the field emission performance and long-term stability of the CNWs structures is more superior to that of planar carbon nanowall mats and comparable to that reported for optimized carbon nanotube based emitters.

Carbon nanowalls usually have been grown using various CVD methods such as microwave plasma, radio frequency (RF) inductively coupled plasma [28], and even by sputtering of a glassy carbon target. This synthesis methods are the same procedure used to prepare diamond films and carbon nanotubes. Commonly, a combine of hydrocarbon (CH_4) and hydrogen, is used as precursor gases for the preparation of carbon nanowalls. High-density plasmas like inductively coupled plasma and microwave plasma are applicable for the synthesis of CNWs because they present a good behavior in the decomposing H_2 molecules. This

phenomena it's very important in the formation of CNWs because it is considered that a large amount of H atoms is required for the growth of the nanostructures, which is similar to the case for diamond growth. The growth of CNWs doesn't require metal catalysts like other carbon nanostructures (carbon nanotubes). Consequently, carbon nanowalls have been fabricated on several substrates, including Si, at substrate temperatures of 500–700°C without the use of catalysts [29].

Figure 13 a, b show two types of microwave plasma-enhanced chemical vapor deposition (MWPCVD). In particular fig. 13 a show the NIRIM apparatus (the National Institute of Research of Inorganic Materials, Japan) while in fig. 13b it's reported ASTeX scheme (Applied Science and Technology, Inc.). In the case of NIRIM-type MWPCVD system, the CH_4/H_2 plasma is generated in a cylindrical quartz tube, which meets a rectangular waveguide, fig 13a. The most important advantages of NIRIM-type reactors are (1) easy reactor design with low set-up costs and (2) possibility to vary the position of substrate respect to the plasma. On the other hand, the diameter of the cylindrical quartz tube limited the size of substrate to approximately a few cm^2. The ASTex-type reactor consists of a cylindrical stainless steel chamber. Above the substrate there is a discharge called a "plasma ball". In this system, the CVD process could be operated at high pressures ($\sim 10^3$ Pa), but it's impossible to vary independently the reactor pressure and microwave power. At too high pressure or low microwave power, plasma cannot be sustained.

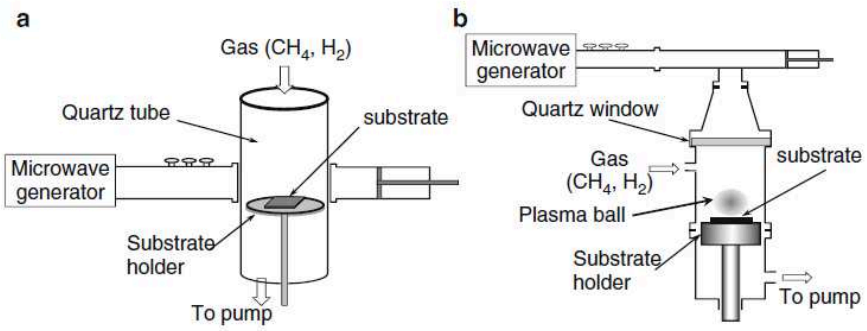

Figure 13. Schematic of microwave plasma-enhanced CVD systems. (a) NIRIM (National Institute of Research of Inorganic Materials) type, (b) ASTeX (Applied Science and Technology, Inc.) type

Wu et al. reported the synthesis of carbon nanowalls on the catalyzed substrate using the NIRIM-type MWPCVD reactor [24].

For the first time carbon nanowalls was synthesized during the growth of carbon nanotubes; but now Wu et al. successfully synthesized carbon nanowalls on various substrates using MWPCVD, and analyzed the formation of carbon nanowalls with different gas flow rate ratio and electrical field. Typical carbon nanowalls were grown employing a mixture of H_2 and CH_4 in the flow rate ratio of 4 and substrate temperatures of 650–700C. In figure 14 are reported SEM images of carbon nanostructures grown at different H_2/CH_4 flow rate ratios. This parameter causes many changes to the morphology of the nanocarbon films. Typical carbon nanowall film was grown at the H_2/CH_4 flow rate ratio of 4, as shown in Fig. 14 e.

Chuang et al., using a source mixture made of ammonia and acetylene, reported the growth of carbon nanowalls in 3D aggregates by MWPCVD using ASTex-type reactor. They also studied field emission properties of this structures [30].

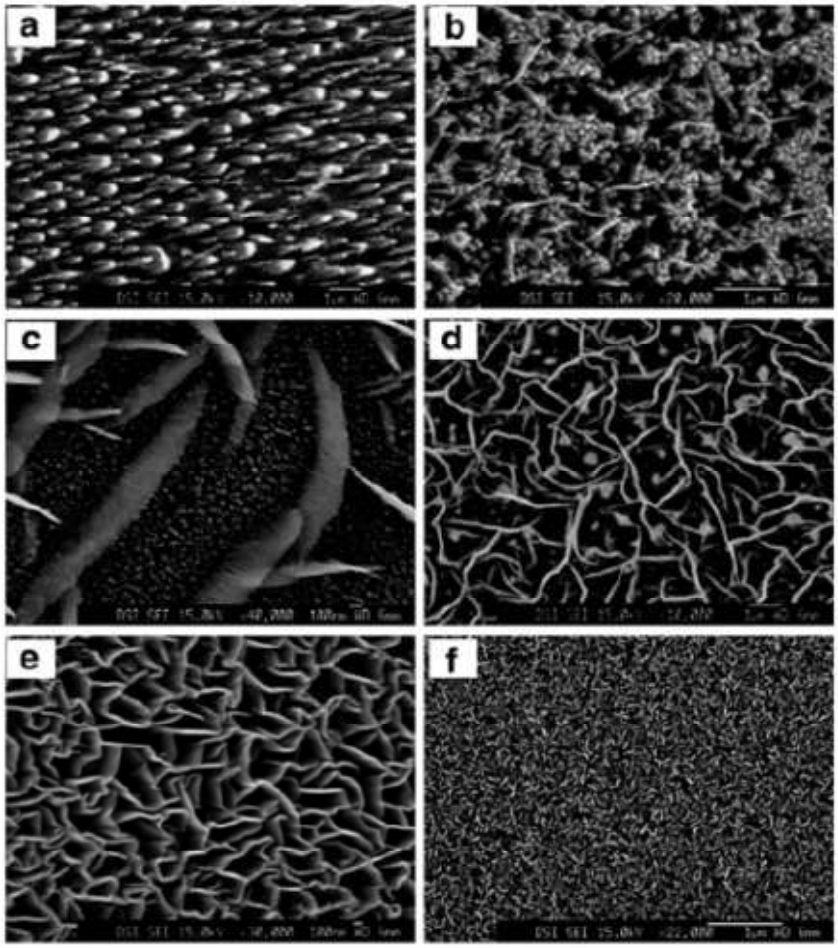

Figure 14. SEM images of carbon nanostructures grown at different H_2/CH_4 flow rate ratios

The gas flow rate ratio NH_3/C_2H_2 below 1 allows to create microstructures of carbon nanowalls. In their method, growth of carbon nanowalls was catalyst-free. Similar structures obtained with this technique are reported in Fig. 15.

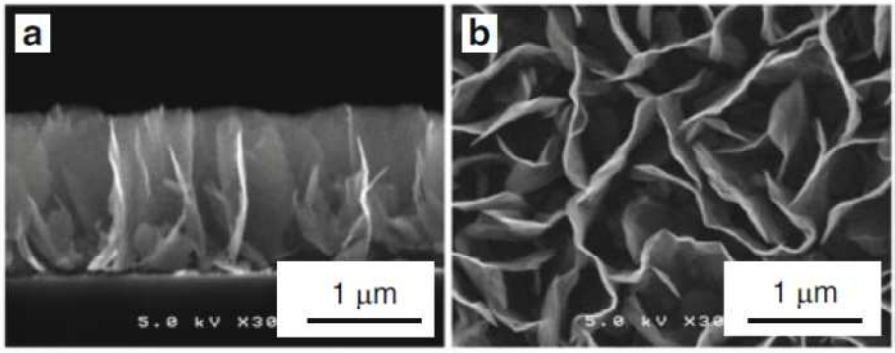

Figure 15. SEM images of carbon nanowalls grown by MWPCVD using ASTex-type reactor

All of the techniques reported above need to high temperature to work and also they need to gas flows that means it's obliged to use complicated vacuum systems. For these reasons we tried to obtained CNWs in a way without the necessity to employ vacuum systems or high temperature. We obtained CNWs by using PLAL and after that we applied an electric field in order to start the growth of nanostructures onto the electrodes.

1.3 CONDUCTIVE NANO-NETWORK

The fast development of nanotechnology has conducted to requests on new 1D materials with new functional properties. Carbon nanotubes have obtained most attention, followed by nanowires of very different kinds. In the last years inorganic molecular wires, in particular molybdenum halide, have appeared as a new type of 1D materials with conspicuous molecular-scale functionality. These molecular nanowires are single in terms of molecular properties and structure. Their one-dimensional polymer structure gives rise to some very unusual physical properties. Anionic bridges which engage Mo clusters together into one-dimensional chains are exceptionally strong, yet highly deformable, giving rise to extraordinarily high Young's moduli and nonlinear mechanical properties respectively. The sulfur atoms within the structure facilitate diverse functionalization chemistry to thiol-containing molecules, such as proteins. The connectivity of the molecular wire ends to gold nanoparticles and surfaces with covalent bonds and good electronic coupling enable self-assembled molecular-scale connections to be made between individual molecules [31].

1.3.1 MoSI FUNCTIONALIZED WITH GOLD NANOPARTICLES

$Mo_6S_{9-x}I_x$ (MoSI) molecular nanowires have been recently shown to form intriguing large-scale self-assembled networks using specific bonding with gold nanoparticles in solution.

In figure 16 it's shown a schematic representation of the major studied stoichiometry of this material in particular $Mo_6S_3I_6$ structure in which it's possible to observe how molybdenum composes a cage made of six atoms and sulphur atoms form bridges bond with molybdenum atoms.

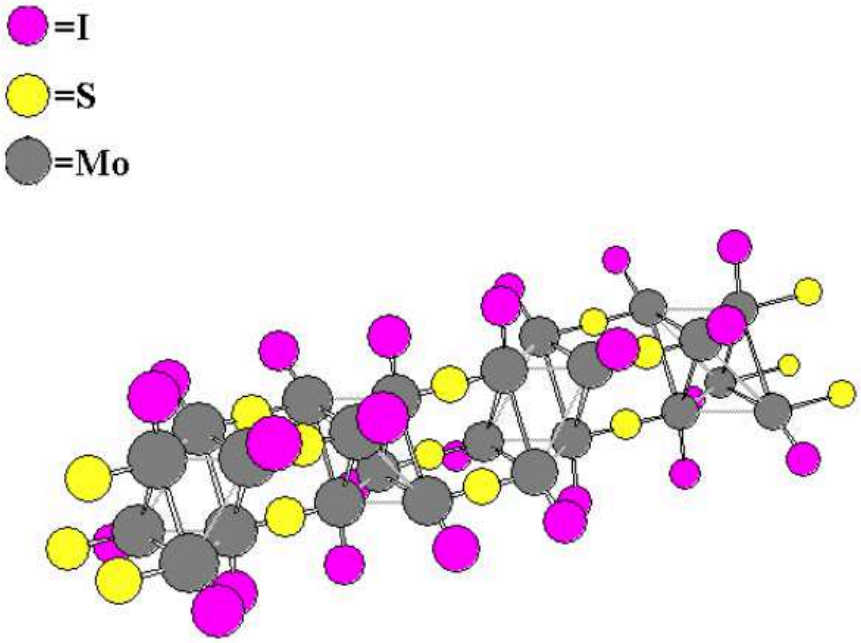

Figure 16. Schematic representation of $Mo_6S_3I_6$ structure

These systems have intriguing properties for the field emission applications as reported by Zumer et al. [32] in which a single nanowire was mounted on an indium-coated nickel holder by dielectrophoresis in isopropyl alcohol as shown in figure 17

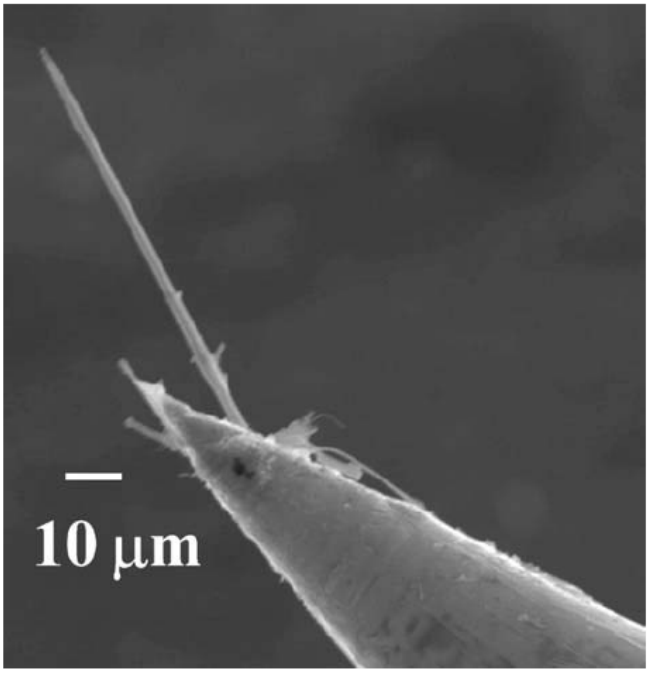

Figure 17. Single nanowire mounted on indium-coated nickel holder for testing field emission

After that they measured, by field emission microscope (FEM), the current through the wire and it was of 1μA. One of the most promising and exciting application for MoSI is the formation of molecular-scale

connectors for molecular electronics. For this application it's need to work with a real thin nanowire.

Generally MoSI are synthesized, in bundle of nanowires, through heating treatment of molybdenum, sulphur powder and iodine in a sealed and evacuated quartz ampoule at 1070 °C. The resulting material has a where the diameter of individual bundles ranges from 100 nm to 1000 nm (Fig. 18). The bundles can have a wide range of lengths, up to >5 mm. The as-produced material is rather tough, and individual bundles are not easily broken on handling, instead they appear to smear easily, indicating that exfoliation takes place.

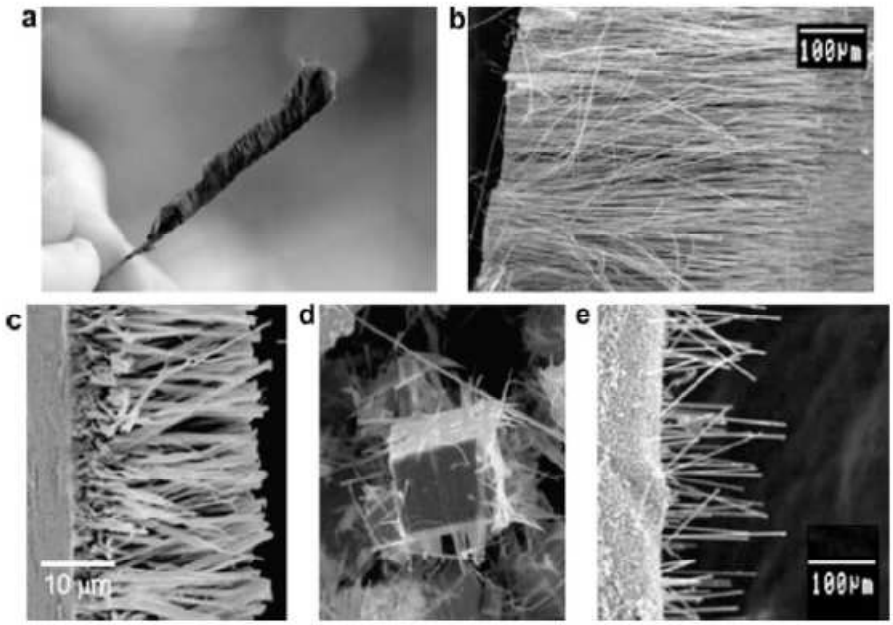

Figure 18. Some pictures of the obtained material after the synthesis

The material obtained with this method cannot used for nano-application and furthermore the purification is not so easy. For this reason I went to work at Josef Stephan institute Ljulbjana and during my experience I tried to develop the synthesis route in order to obtain real thin nanowires for the application in the electronics field without the need to purify them. I have also try to understand the structure of these networks, made of MoSI functionalized with gold nanoparticles prepared by Laser ablation in liquid, through a detailed bonding state analysis. We demonstrate that during the network formation, there is a strong chemical interaction between gold atoms belonging to the nanoparticles and the elements constituting the nanowire's skeleton. Moreover, it is shown that part of the nanowire's integrity is lost. Evidence for such behavior is reported through spectroscopic and microscopic observations using the $Mo_6S_{4.5}I_{4.5}$ stoichiometry [33].

REFERENCES

[1] Wu et al. *Journal of Material Chemistry*, (2004), **14**, 469-477

[2] Hofmann et al. *Powder Technology Laboratory*, IMX EPFL (2009)

[3] Geim. *Science*, (2009), **324**, 1530-1534

[4] Compagnini et al. *Chemical Physics Letters*, (2008), **457**, 386-390

[5] Tenne. *Elsevier Science Ltd*. Fullerene-like structures and nanotubes from inorganic compounds

[6] Kroto et al. *Nature*, (1987), **329**, 529-531

[7] Iijima et al. *Journal of Crystal Growth*, (1980), **50**, 675-683

[8] Tenne et al. *Nature,* (1992), **360**, 444-446

[9] Margulies et al. *Nature,* (1993), **365**, 113-114

[10] Hershfinkel et al. *Journal of American Chemical Society,* (1994), **116**, 1914-1917.

[11] Tenne et al. *Advanced Materials,* (1995), **7**, 965-995

[12] Rosentsveig et al. *Tribology Letters*, (2009), **36**,175-182

[13] Yakobson et al. *American Scientist*, (1997), **85**, 324-337

[14] Novoselov et al. *Nature* (2005), **438**, 197-200

[15] Remskar et al. *Science* (2001), **292**, 479-481

[16] Splendiani et al. *Nano Letters*, (2010), **10 (4)**, 1271-1275

[17] Novoselov et al. *Proceedings of the National Academy of Sciences U.S.A.,*(2005), **102**, 10451-10453

[18] Coleman et al. *Science*, (2011), **331**,568-571

[19] Geim et al. *Nature Materials,* (2007), **6**, 183-191

[20] Compagnini et al. *Carbon,* (2009), **47**, 3201-3207

[21] Yihong et al. *Journal of Matererial Chemistry*, (2004), **14**, 469-477

[22] Compagnini et al. *Carbon,* (2012), **50**, 2347–2374

[23] Ando et al. *Carbon*, (1997), **35**, 153-158

[24] Wu et al. *Advanced Materials*, (2002), **14**, 64-67

[25] Suzuki et al. *Japanese Journal of Applied Physics*, (2011), **50**, 01AF08-1- 01AF08-2

[26] Giorgi et al. *Sensors and Actuators B,* (2007), **126**, 144-152

[27] Stratakis et al. *Applied Physics Letters*, (2010), **96**, 043110-1-043110-3

[28] Wang et al. *Applied Physics Letters,* (2004), **85**, 1265-1267

[29] Shiji et al. *Diamond Related Materials*, (2005), **14**, 831-834

[30] Chuang et al. *Diamond Related Materials,* (2006), **15**, 1103-1106

[31] Mihailovic et al. *Progress in Materials Science*, (2009), **54**, 309-350

[32] Žumer et al. *Nanotechnology,* (2005), **16**, 1619-1622

[33] Compagnini et al. *Journal of Physical Chemistry Letters*, (2010), **1**, 393-397

2 SYNTHESIS AND CHARACTERIZATION OF MoS_2 NANOSTRUCTURES

As said before, MoS_2 nanostructures are usually synthesized through gas phase reactions with appropriate reactors, high pressure systems and gas reagents. The mains problems of these procedures are: the difficult to work in gas phases with dangerous gases, for instance H_2S needful for the sulphurization of molybdenum particles, the need to work at high temperature, above 950 °C, that results very expensive, and the necessity to work with complicated high pressure systems.

We tried to obviate each of these problems carrying out the synthesis in a liquid phase and at room temperature without the use of H_2S or something dangerous like this. We were able to perform this through the laser ablation in water.

Laser ablation of solid targets in liquid media is emerging as a simple, clean and reproducible way to generate a large number of intriguing nanometric structures with peculiar properties. The method is intrinsically environmental friendly and allows the formation of nanostructures which are free of any waste by-product. Moreover the non-equilibrium conditions typically observed during the ablation process open the way to new synthetic routes. Such a top–down approach

can be considered greener than standard sulphidization reactions and represents an intriguing single step procedure.

The transition-metal dichalcogenide semiconductor MoS_2 has engaged enormous attention due to its particulars properties in many application as electronic, optical, and catalytic fields, as well as its importance for dry lubrication [1]. The bulk MoS_2 crystal is an indirect-gap semiconductor with a band gap of 1.29 eV [2], and presents a layered structure in which there are some van-der-Waals bonds between two layers made of S-Mo-S units. Each of these stable units consists of two hexagonal planes of S atoms and an intermediate hexagonal plane of Mo atoms coordinated through covalent interactions with the S atoms in a trigonal prismatic arrangement [3]. Thanks to these relatively weak interactions between these layers and the strong interlayer interactions, it's possible to form some ultrathin crystals of MoS_2 by the micromechanical cleavage technique, as demonstrated by Novoselov et al. [4].

2.1 MoS_2 fullerene-like

It has been demonstrated [5] that laser ablation of MoS_2 in water could lead to the formation of IF-MoS_2 nanoparticles. This interesting result opens a possible route to the application of laser ablation as a large scale synthesis method, since most of the synthetic approaches for the formation of IF-MoS_2 need the use of hazardous compounds such as H_2S and H_2 with difficulties in handling and storage [6], and high pressure and temperature conditions. Laser ablation in liquid phase can be considered as a valid alternative, capable to conjugate a gram-scale production of highly stable nanomaterials, under a rigorous control of the process parameters, with environmental sustainability [7].

Before talking about the experimental work I would to focus the attention on the mechanism of PLAL with its advantages and disadvantages.

During the laser ablation of a target both in gas phase and in liquid phase it's generated a plasma made of the atoms constituting the target. Indeed the plasma plume is generated by laser pulse irradiating the surface of the solid target as shown in fig.19 (b). Since the temperature in the vapor plume can rise to much high values, a plasma plume will be generated during the front part of the incident laser pulse irradiating the solid target as shown Fig. 19 (a) and (b). The condensation of this plasma generates the products of PLA. Yang et al. [8] report in our work a scheme of the most important steps in the formation of the products in a PLA process in gas phase.

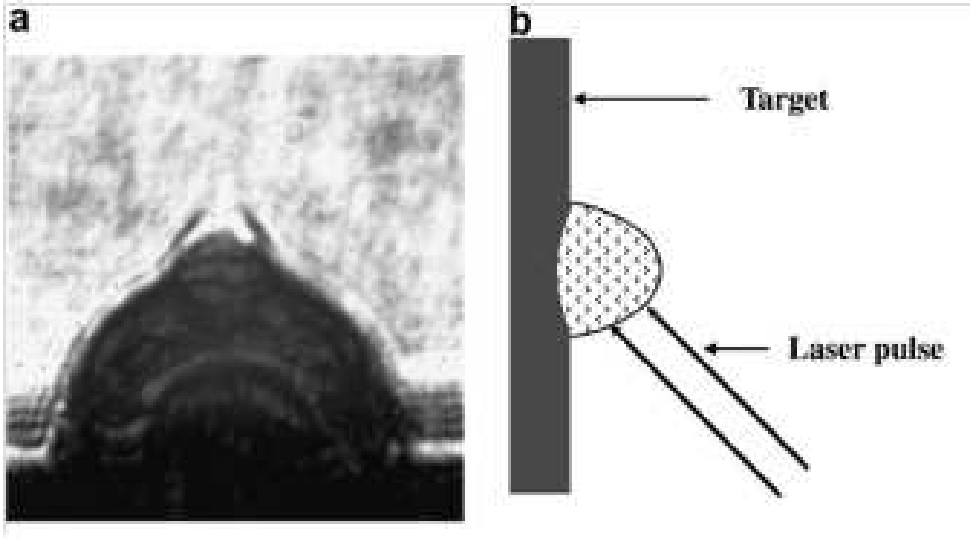

Figure 19. (a) The shadowgraph image of the plasma plume from the laser ablation in the gas phase. (b) The generation of the laser-induced plasma on the surface when the front part of the laser pulse ablating the target

First, as said before, we notice the formation of plasma plume due to the interaction between laser pulse and target material. It is known that, the ablation mechanisms generating the formation of the plasma plume are different for the nanosecond and picosecond and femtosecond, laser pulses. We are interested about the ablation of the nanosecond laser, in which the material expulsion is controlled by thermal processes [9].

In the case of nanosecond laser ablation, photons can couple with both electronic and vibrational modes of the target material and moreover, this interaction produces an immediate rise in the electron temperature and eventual vaporization of the target as reported in fig. 20

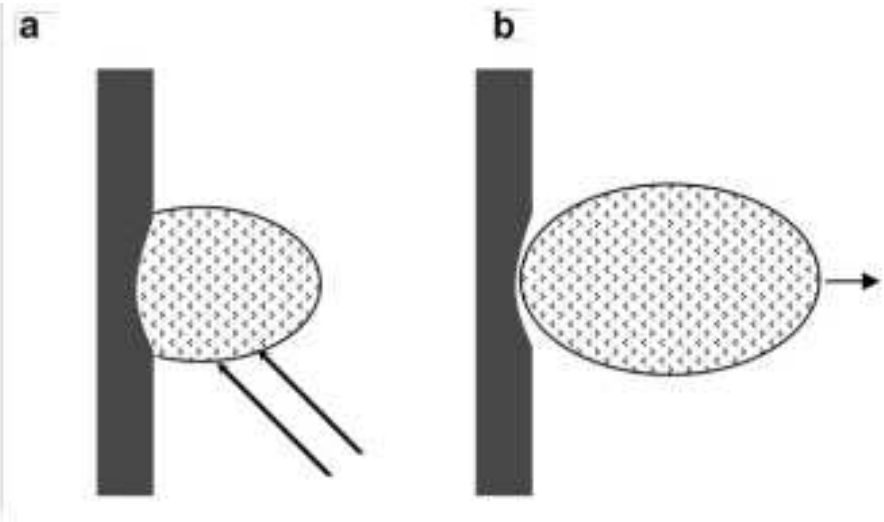

Figure 20. (a) The free expansion of the laser-induced plasma in vacuum or gas when the plasma absorbed the later part of the laser pulse. (b) The ejection of the plasma plume from the target

The evaporated material after the vaporization process, will interact with background gas, yielding the confinement of the plume, whereas the background gas is pushed further away from the solid target. Inside the plasma plume there are many neutral atoms, ions, and electrons deriving from the target solid. The electron contribution is usually present in the formation of the plasma plume only in the case of nanosecond laser

ablation, and this behavior is due to the photon-electron coupling could lead to a rapid excitation of the electron distribution. Usually the interface between the plasma plume and solid target, during the laser ablation, is in the gas state because of the high temperature of the plasma, due to irradiation by the laser pulse. The temperature of the plasma plume could rapidly reach the equilibrium and this phenomena is due to the interaction of ion and electron which accelerating their movement increase the collisions in the plasma plume [10]. Therefore, during the ablation using the nanosecond laser pulse, after the creation of the plasma plume, the later part of the incident laser pulse both directly irradiates the plasma plume and continually ablates the solid target through the plume. So in the case of nanosecond laser this plays two roles in the transformation stage of the plasma plume. The first one is, the irradiation of the target with the excitation and ionization of the species in the plume and in the second step, the later part of the laser pulse continually irradiates the interface between the plasma plume and the target and this phenomena continue to ablate more species into the plume, and then causes the plume to expand further. This second step leads to a rapid expansion of the plasma plume in vacuum, and also heats the plasma plume at higher temperature and higher species' density as shown in Fig. 20(a) . Due to the react effect [11], the plasma plume is ejected from the surface of the target as shown Fig. 20(b). The last step of the evolution of the plasma plume created by PLA is cooling down and condensation in vacuum and the ambient gas.

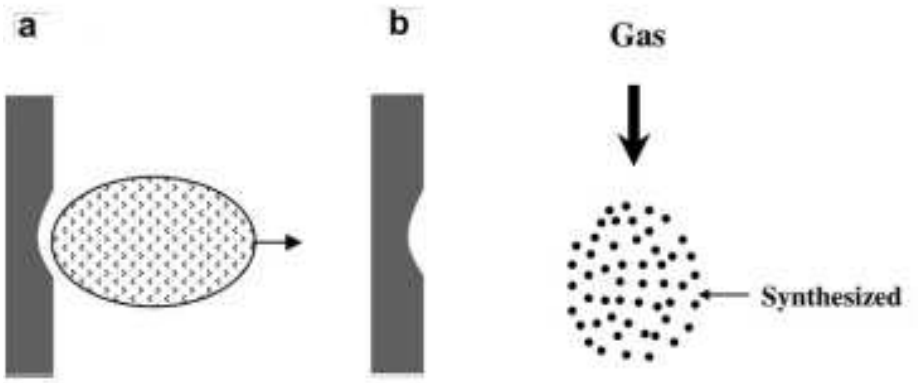

Figure 21. (a) The ejection of the plasma plume from the target and (b) condensations of the laser-induced plasma

The fig. 21(a) and (b) shows the evaporation and formation of the plasma plume in gas phase. In fig. 21 (a) is reported simply the evaporation of plasma plume and in fig. 21 (b) it's reported the condensation of the plasma freely assisted by a cool ambient gas to form nanoparticulates. The laser ablation of a target in liquid presents some difference in the formation and evolution of plasma plume. The most important difference between laser ablation of solids in vacuum or diluted gas and in liquids is that liquids confine the movement of the plasma plume. The liquid confinement, in the case of laser ablation of solids in liquid environments, change some series of processes, previously analyzed, as for instance generation, transformation, and condensation of the plasma

plume in the case of laser ablation of solids in gas phases. This confinement from liquids can induce some changing in the kinetic and thermodynamic properties of the evolution of the plasma plume and for this reason it's possible to distinguish, from these changes, the different environments used in laser ablation. Therefore, studying the evolution of the plasma plume in laser ablation in liquids it's possible to know the potential in technology such as materials processing.

The generation of the plasma plume from the solid target it's caused by the interaction between the laser pulse and the surface of the solid target like in the case of the ablation in gas phase, with only one difference rather the confinement of the plasma plume by the surface tension of the liquid environment. This is schematically illustrated in Fig. 22(a).

The main difference between the two environments is in the growing and expansion of the plume. In the case of PLA in vacuum and in diluted gas, the expansion of the plasma induced by the laser is confined by the liquid. The confinement of liquids induces the plasma into a different thermodynamic state compared to the laser ablation in gas environments. This confinement is reported in the figure 20 (b).

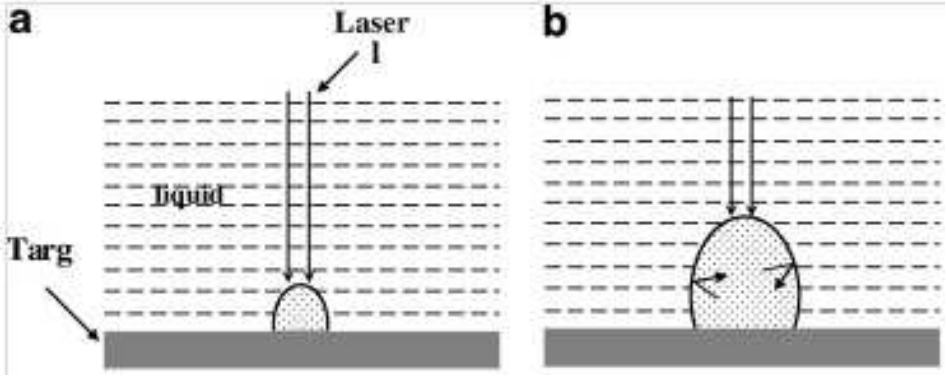

Figure 22. The evolution of the laser-induced plasma in liquid. (a) The generation of the laser-induced plasma. (b) The expansion of the plasma plume in liquid

Fabbro et al. studied that the confinement of the plume caused by liquid environment produce a shock wave inside the plasma plume induced by the laser ablation.

The plasma plume expands its volume at a supersonic velocity and this phenomena creates a shock wave under the confinement of liquid. When the later part of the laser pulse hits the solid target another amount of the vaporizing species is generated. Then, this shock wave produces an extra pressure in the plasma and this pressure causes an increasing of the temperature of the plume.

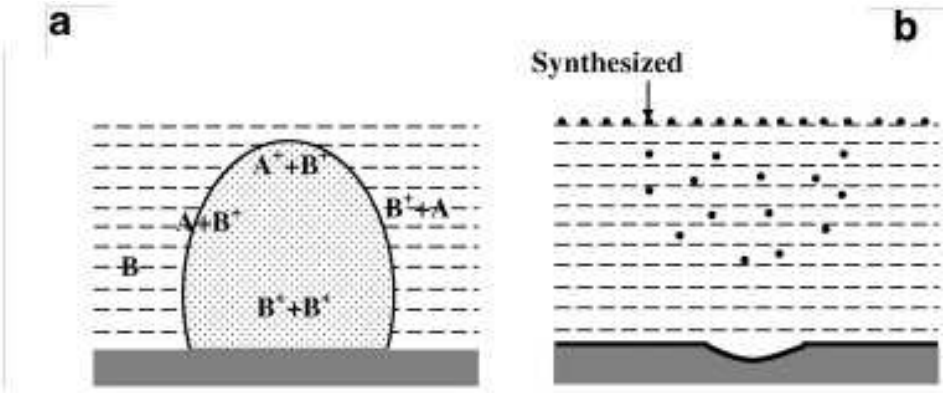

Figure 23. (a) Some example of chemical reactions during the laser ablation of a target in liquid. (b) Condensations of the plasma plume in liquid

Therefore, this growth mechanism of plasma plume due to the confinement of liquid leads it into a thermodynamic state of the higher temperature, higher pressure and higher density, see fig. 22 (b), than that the plasma plume generated in the case of the laser ablation in gas phase. From studies conducted by Peyre et al. et al. [12] they noticed a pressure of the plasma plume in liquid of 5 GPa for a period of the laser pulse of 30 ns but they also noticed that for the shorter laser pulse of 3 ns allows to have a pressure of 10 GPa. Indeed, the wavelength, the power and the duration of the laser pulse can influence the value of the plasma-induced pressure [13]. Inside the plasma there is a temperature of 4000–5000 K, when a 532 nm Nd:YAG laser with pulse duration of 10 ns and power of 1010 W is used to ablate a isotropic graphite target in water. I would underline that the thermodynamic state with high pressure, high

temperature, and high density promote the formation of the metastable phases that are in the high-temperature and high-pressure region on their thermodynamic equilibrium phase diagram.

Yang shows in figure 23 (a) some kinds of chemical reactions would take place in the plasma plume and the interface between the liquid and the laser-induced plasma. The first kind of chemical reaction appears inside the laser-induced plasma. When inside high-density plasma there is high temperature and high pressure, the new phase, especially the metastable phase, is formed by the high temperature chemical reactions between the ablations from the target. Another kind of chemical reaction, between the reactant species are from the target and the liquid, also takes place inside the laser-induced plasma. As said before, the high pressure and high temperature in front of the laser-induced plasma lead to the excitation and evaporation of the liquid molecules at the interface between the laser-induced plasma and the liquid, and create the new plasma of the liquid molecules at the interface. After that there will be some chemical reactions between the species from the laser ablating target and the species from the liquid molecules creating some chemical species which are different from the species constituting the target and the liquid.

The last step of the evolution of the plasma plume in a process of PLA of a target in liquids is cooling down and condensation in the confining liquid shown in Fig. 23(b).

As described above laser ablation of a target in liquid environment permits us to fabricate and create some chemical compounds which are different from the composition of the target. Indeed by the reactions

occurring between the plasma plume and the liquid environments it's possible to form some kind of interesting nanostructures exploiting the metastable conditions available inside the plasma.

For these reasons we decided to synthesize MoS_2 fullerene-like by the using of PLAL and following I'm going to describe my experimental work.

The experimental evidences allow us to propose a growth mechanisms for the MoS_2 nanostructures formation in agreement with literature data.

Solutions were prepared ablating a polycrystalline MoS_2 target (the absorption coefficient at 532 nm $\sim 10^5$ cm^{-1}) was obtained pressing MoS_2 commercial powder (Aldrich) for 10 min at 10 t. The ablation has been conducted using a 532 nm radiation coming from a Neodymium-Yttrium Aluminum Garnet (Nd:YAG) laser with a 5 ns pulse duration and a 10-Hz repetition rate. A sintered MoS_2 target was cleaned in an ultrasonic bath using several solvents to remove organic contaminations and it was placed at the bottom of a glass vessel filled with the chosen liquid. The thickness of the liquid above the target was about 15 mm, and the ablation time was maintained at around 15 min. The laser beam was focused on the target using a 10 cm focal lens placed above the vessel as shown in the figure 24. After 15 min of irradiation a brownish solution is obtained. Used fluences ranged between 1 and 10 J/cm^2 in order to test the best production rate. Ablation was performed in water (Millipore grade) and n-decane (Analytical grade from Carlo Erba).

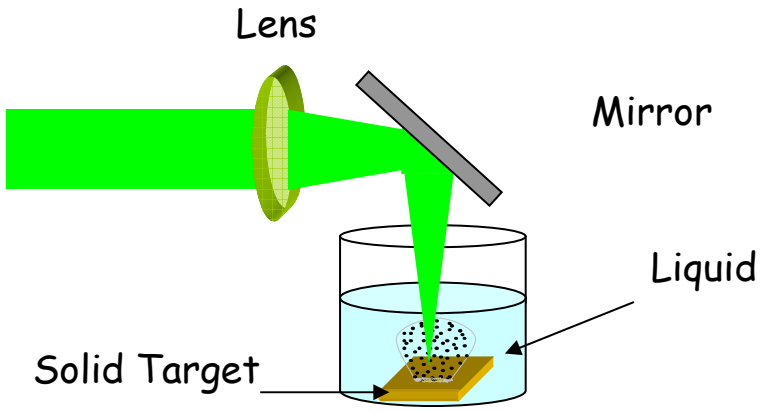

Figure 24. Typical experimental setup to ablate a solid target in a liquid environment

After the ablation, as-produced solutions have been filtered with 0.2 μm pore size filters to remove any gross particulate matter and then drop-casted on HF cleaned silicon substrates in order to perform X-Ray Photoelectron Spectroscopy (XPS) analysis. XPS spectra have been recorded using an AXIS-ULTRA spectrometer with a basic pressure of 10^{-9} Torr. The X-ray radiation was generated by an Al Kα line decay (1486 eV) at operating conditions of 18 kV and 13 mA. Emitted photoelectrons were analyzed with a hemispherical electron energy analyzer. Detailed spectra have been acquired with a resolution below 1 eV. The obtained solutions were also drop-casted on copper grids for

Transmission Electron Microscopy (TEM) characterization. Images were acquired using a JEM 2010F JEOL microscope operating with an acceleration voltage of 200 kV.

TEM images, reported in Fig. 25, reveal a large number of structures produced at the nanometric size range.

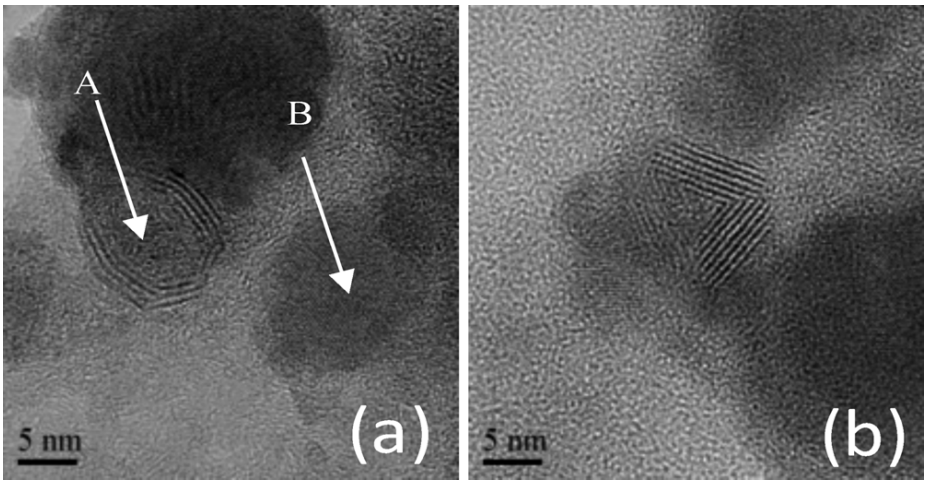

Figure 25. (a) TEM image of MoS_2 (A) and MoO_3 (B) IF-nanostructures; (b) TEM image of MoS_2structures with different shape

At least two of them were identified and labeled with letters a and b in Fig. 25 a. The first one (a) can be attributed to hollow fullerene-like MoS_2 clusters [14]. The identification is due to the presence of peculiar features, such as the interlayer spacing of 0.6 nm and the polyhedral closed cage structure, thermodynamically more stable than the isolated

basal sheets of a sulphide lamellar structure [15]. The inner part of the cages seems to present a solid core. In some cases MoS_2 nanostructures with different shapes have been observed as well. For instance, Fig. 25 b reports multi-walled clusters where sulphide layers (same interlayer distance of 0.6 nm) are stacked to form flat planes instead of curved surfaces. Such kind of nanoparticles could be the result of direct fragmentation processes of the target or of a successive size reduction due to laser (re)irradiation. Indeed the phenomenon of progressive laser fragmentation during PLAL has been already observed during the irradiation of metallic targets and has been recognized as an active mechanism during PLAL at appropriate wavelengths [16].

Furthermore nanoparticles size distributions are reported in the graphic 1 in which is possible to notice that the distribution for MoS_2 and MoO_3 , even though slightly shifted, are located in the same size range suggesting a correlation between the formation of sulphides and oxides.

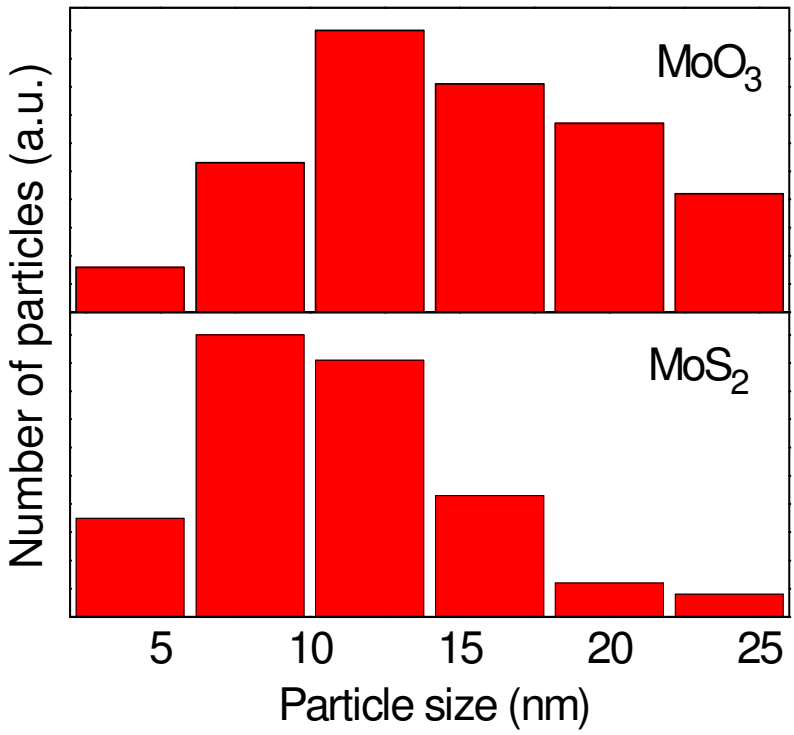

Graphic 1. Size distribution of the nanoparticles produced after laser ablation in water

Other particles with different crystalline arrangement have been evidenced by TEM observations and labeled with the letter B in Fig. 25 a. Lattice fringes are evident in the image and suggest that the particle is a single crystalline MoO_3 cluster on the basis of the interlayer distances (0.35nm), in agreement with literature data [17]. A nanoscopic elemental analysis has been also reported in Fig. 26.

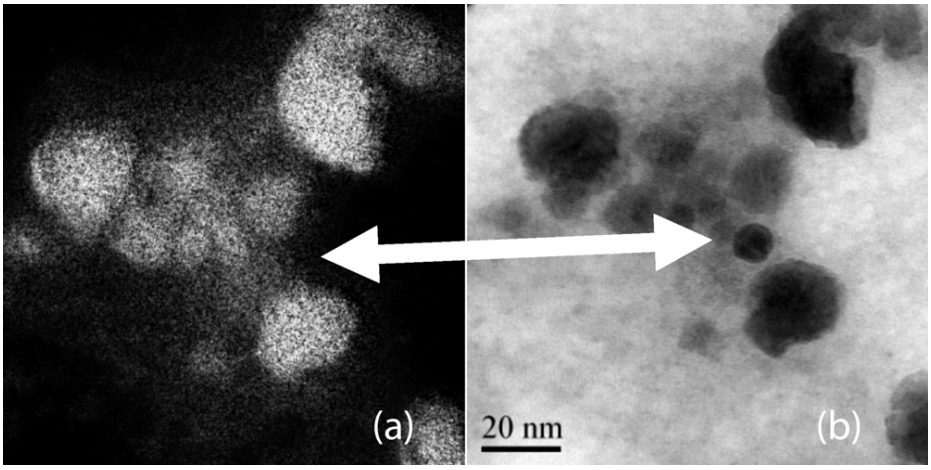

Figure 26. Comparison between the elemental sulphur map (a) and the electron image (b) in the same region. The arrow indicates a MoO_3 nanoparticle

There we display a large area which includes several nanoparticles, comparing an electron image (Fig. 26b) with the respective sulphur map (Fig. 26a). The arrow indicates an oxide nanoparticle where the sulphur signal is absent. Such a result is at the same time obvious and intriguing. First of all it must be observed that, during the ablation of the MoS_2 target by nanosecond laser pulses, the interaction of the front part of the laser pulse creates vapours above the target surface which are irradiated by the tail part of the same pulse. This leads to photoionizations and to the creation of a dense, high-temperature, and high-pressure laser plasma plume, which expands into the liquid. During this expansion phase, the plasma plume interacts with the surrounding liquid, creating cavitation bubbles, which, upon their collapse, give rise to extremely high temperature and pressure see Figure 27.

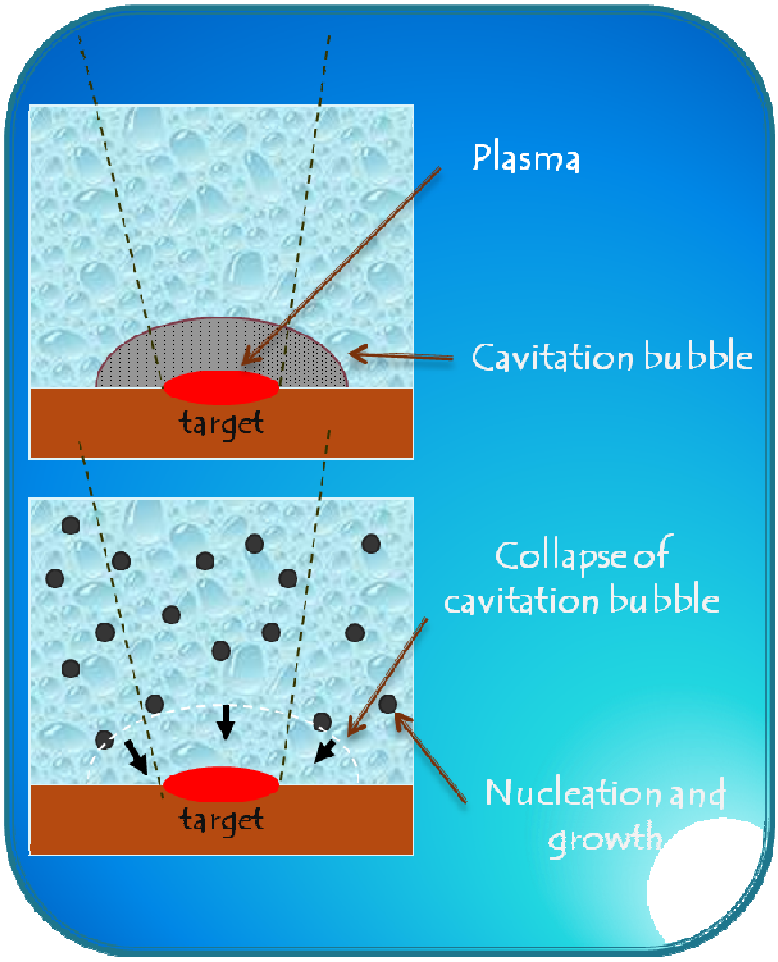

Figure 27. Cartoon of the cavitation bubble and nucleation and growth of the nanoparticles during the PLAL

As previously mentioned in the beginning of this chapter in such a condition, dissociation of MoS_2 and water happens, giving rise to the presence of molybdenum ions and reactive oxygen species. Of course,

these conditions are compatible with the formation of stable oxide species and the formation of MoO_3 is highly probable. As reported in literature, molybdenum oxides are essential precursors for the formation of IF-MoS_2 nanostructures [18]. As said before the reaction path is generally divided into two distinguishable stages: a first surface reaction during which the surface oxide nanoparticle is converted into 1-2 closed monolayers of metal disulphide [19] and a second step consisting in a slow diffusion of sulphur atoms from the vapour plume through the growing sulphide layers to the oxide core of the nanoparticle. Considering that atomic diffusion rates vary exponentially with temperature, it is clear that high temperatures (several thousand of degrees) reached during the PLAL process dramatically shorten the time required to complete the reaction. The conversion of molybdenum oxide into IF-MoS_2 implies the condensation of molecular Mo_3O_9 clusters into substoichiometric MoO_{3-x} nanosize particles, which undergo subsequent sulphidization. From what said before, it is really hard to affirm if the formation of IF-MoS_2 is due to direct condensation of atomic/molecular species in the plasma or to a multistep process which involves the synthesis of oxides or suboxides species. Moreover, it seems that no literature data report specific information about the bonding states and the chemical nature of material produced in the case of IF-MoS_2 synthesis with far-fromequilibrium processes (laser ablation, arc discharge and electron beam irradiation), so XPS analysis were carried out in order to obtain further information about the chemical nature of

obtained species and to try to elucidate the possible reaction routes involved in the formation of IF-MoS_2.

Mo3d signal (left side, Fig. 28) indicates the presence of a predominant amount of Mo^{VI} signals, assigned to MoO_3.

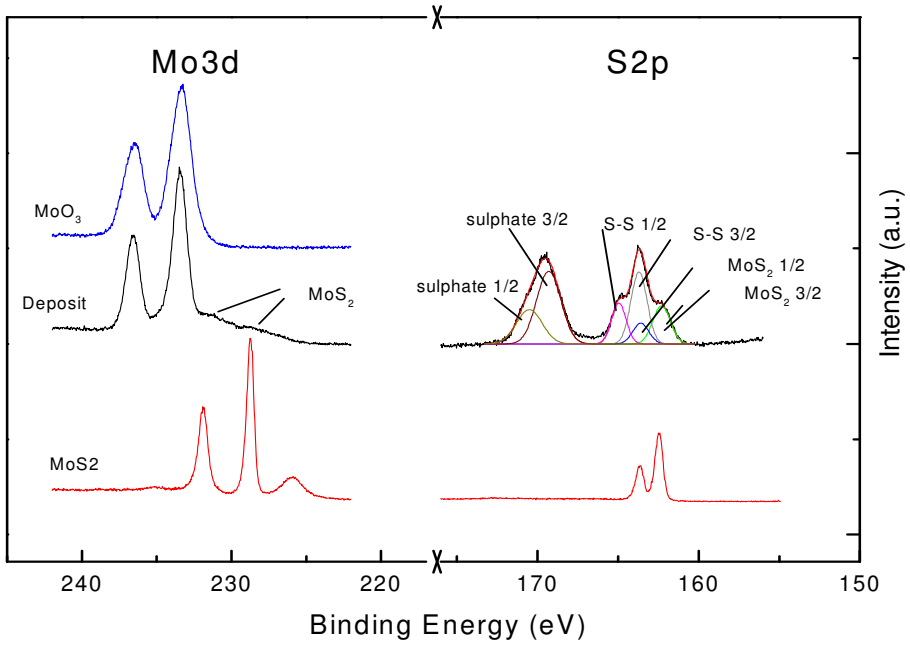

Figure 28. Mo3d and S2p XPS spectra obtained on the ablated materials in pure water, after filtration and deposition onto a substrate (black line). The S2p signals have been decomposed according to literature data. The figure also reports the spectra relative to MoS_2 (red line) and MoO_3 (blue line) bulk target

Signals belonging to MoS_2 are located at lower binding energies as shown in the same figure. In this range of energy XPS spectra show a

continuum of electronic states which could belong either to MoS_2, to oxysulphates or to metal oxides at a lower oxidation state. The observation of the S2p region seems to offer to an easier interpretation. It is possible to point out three different sulphur-containing chemical species, each one giving 3/2 and 1/2 spin–orbit doublets. These doublets fall at 162.3-163.6 eV, 163.7-164.9 eV and 169.2-170.5 eV and can be easily assigned to MoS_2, external sulphur and sulphates respectively, on the basis of literature data [20]. With the attribution of "external sulphur" we indicate both polysulphides and elemental sulphur, since these two compounds are not distinguishable in the XPS spectrum on the basis of B.E. values. Elemental sulphur could be present in our system in the form of linear chains with sulphate groups at the end of each chain. As reported by Steudel [21], such structures have been already found in aqueous solution. The presence of the sulphur is due to the incongruent melting of MoS_2 which decomposes above 1185 °C. The formation of stable molybdenum oxide species including MoO_3, sub-oxides and oxysulphates raises a problem about the nature of oxidation of molybdenum, which is if oxide has to be considered as by-product or if it plays a crucial role in the formation of MoS_2 fullerene-like nanostructures. As previously mentioned, MoO_3 and molybdenum suboxides (MoO_{3-x}) can react at high temperature with sulphur to produce MoS_2:

$$MoO_3 + \frac{x}{2}S \rightarrow MoO_{3-x} + \frac{x}{2}SO_2$$

$$MoO_{3-x} + \frac{7-x}{2}S \rightarrow MoS_2 + \frac{3-x}{2}SO_2$$

From what described, we suppose that IF-MoS_2 nanoparticles found by TEM have been formed in a multistep process at high temperatures during the ablation process.

When the ablation ends, the multistep reaction stops and all the species involved in the reaction path (MoO_3, MoO_{3-x} and MoS_2) can be found in the obtained solution. Based on these considerations, the proposed reaction path would not be possible in an oxygen-free solvent, since the formation of the MoO_3 species in the plasma would be inhibited. To confirm this, laser ablation of MoS_2 was performed also in n-decane, at the same conditions as in the previous experiment. In this case, TEM analysis does not show any relevant structure. Moreover XPS spectra of the filtered system do not reveal the presence of Mo signals. These results can be explained in two ways. It could be possible that carbonaceous contaminations (coming from the partial pyrolysis of the hydrocarbon during the ablation process) form a shell surrounding each produced particle, that avoid the detection of the underlying molybdenum. This effect has been already observed during the ablation of silver and iron targets and reported so far [22]. If the carbon shell is thicker than 5 nm, no electrons from the Mo atoms can be detected, due to the low mean-free path of electrons in the material.

On the other hand, if the formation of MoO_3 is a fundamental intermediate step for the growth of IF-MoS_2, no Mo-containing nanostructures are formed in the plasma during ablation and only "macrofragments" of MoS_2 sheets bigger than 200 nm, are removed from the target.

These fragments are retained in the filtration step before the XPS analysis. If the ablation is performed in water, the presence of reactive oxygen species during the particle formation could come from the breakdown of water molecules and the presence of molecular oxygen dissolved in the liquid. For this reason we performed an ablation experiment purging the liquid with molecular nitrogen, which is one of the most common and effective techniques for the removal of dissolved oxygen from water. This certainly reduces the amount of reactive oxygen available. In such a case, while TEM observations do not reveal any significant variations with respect to the un-purged case, XPS data show some significant differences. In Fig. 29a Mo3d and S2p XPS regions of the sample obtained by ablating the MoS_2 target in water under nitrogen flux are shown.

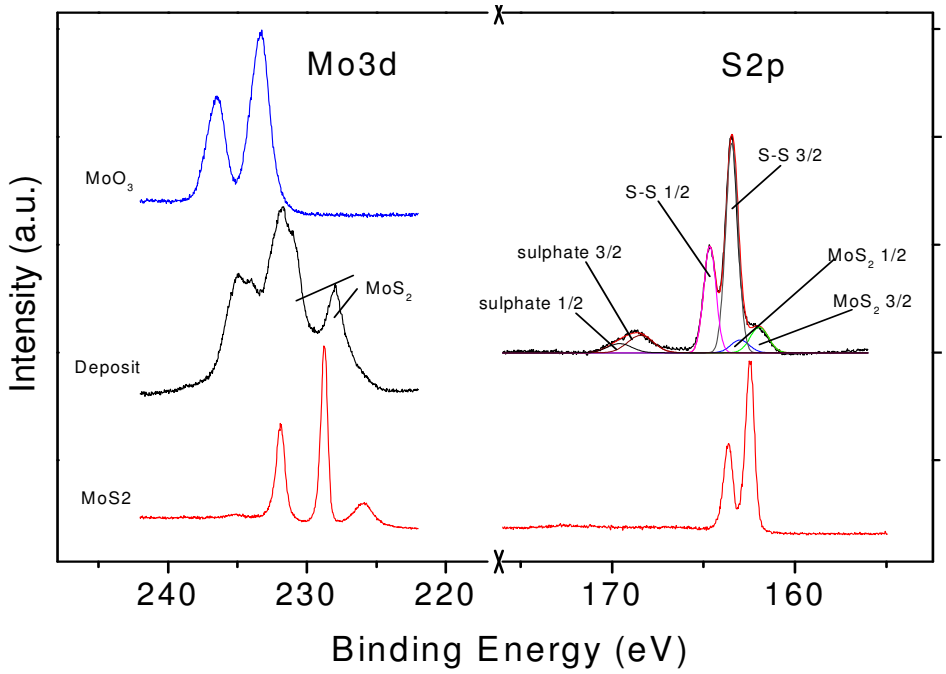

Figure 29. Mo3d and S2p XPS spectra obtained on the ablated materials in pure water purged with a N_2flux (black line). The filtrated sample has been deposited onto a substrate. The S2p signals have been decomposed according to literature data. The figure also reports the spectra relative to MoS_2 (red line) and MoO_3 (blue line) bulk target

The S2p region shows that the amount of MoS_2 and sulphates are significantly lower with respect to external sulphur if compared with those observed in absence of nitrogen purging (see Table 1).

sulphate	S-S bonds	MoS_2	
11 at. %	76 at. %	13 at. %	Not purged
49 at. %	32 at. %	19 at. %	Purged

Table 1. Quantitative XPS results obtained comparing N_2 purged and unpurged

This clearly indicates that, in a poor oxidant medium, only a small fraction of the material ablated leads to the formation of MoS_2 nanostructures, while the most part of it gives the formation of S-S bonds (polysulphides or elemental sulphur). Moreover, we can observe that the Mo3d spectrum reported in Fig. 29 is completely different from the one in Fig. 28. In details, the spectrum in Fig. 29 presents nearly a continuum of states at higher B.E. values, indicating that, together with completely oxidized Mo, different lower oxidation states can be found and suggesting the presence of a larger quantity of substoichiometric oxides. These species are observed with an oxidation state between Mo^{4+} (MoS_2) and Mo^{6+} (MoO_3) and, for this reason, the Mo signal is shifted with respect to the reference signal in Fig. 28. A proper deconvolution of the obtained spectra based on literature assignation [21] can be found in the (Fig. 30).

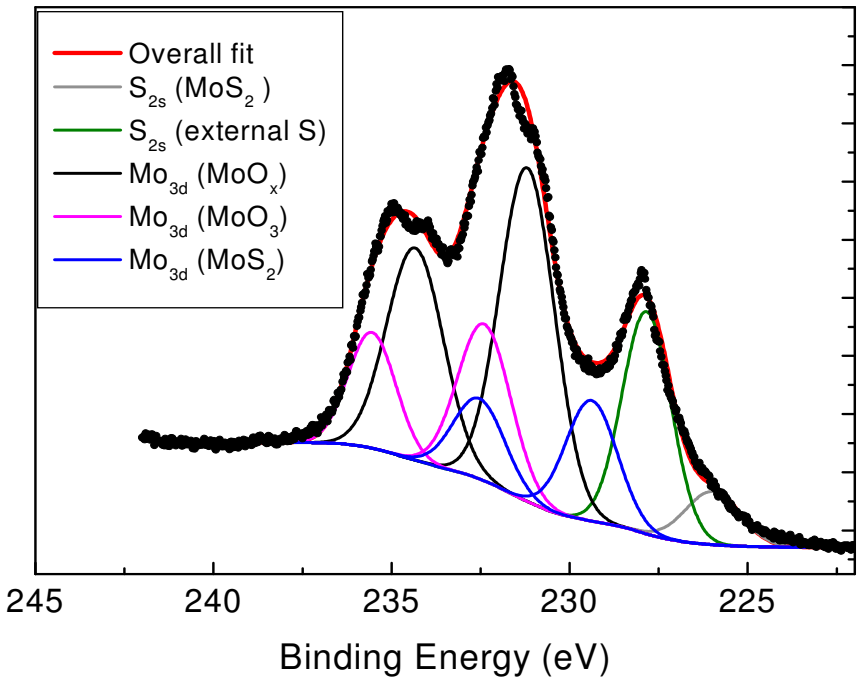

Figure 30. XPS spectrum in the Mo3d region relative to the ablated material obtained by a PLAL procedure in pure water, purged with a N_2 flux

The figure shows a deconvolution into several components as suggested by literature data. This deconvolution takes into account the presence of either stoichiometry molybdenum oxide and sub-stoichiometry species (spin-orbit doublets with the same colour in the figure). In the same spectral region S2p signals (single component) have to be considered taking into account the presence of external sulphur, sulphates and

molybdenum disulphide. The deconvolution clearly indicates the presence of suboxides at lower binding energies. The amount is relevant due to oxygen deficiency during plasma formation and evolution. This last consideration strongly corroborates our assumptions and confirms our model. To resume:

- If oxygen is available, Mo is present in a great quantity in the sample analyzed and most of it is completely oxidized (Mo^{VI}). In this case a great part of the S2p signals is related to the IF-MoS_2 species. Some samples has been annealed in vacuum at temperatures up to 500 °C (see Fig. 31) and the results of the thermal annealing experiments have shown that the situation, partially frozen during the extinction of the plasma plume, continues to evolve towards the formation of crystalline MoS_2 at annealing temperatures above 300 °C. Indeed the system tends to evolve towards MoS_2 either loosing the sulphate component and drastically reducing the amount of external sulphur.

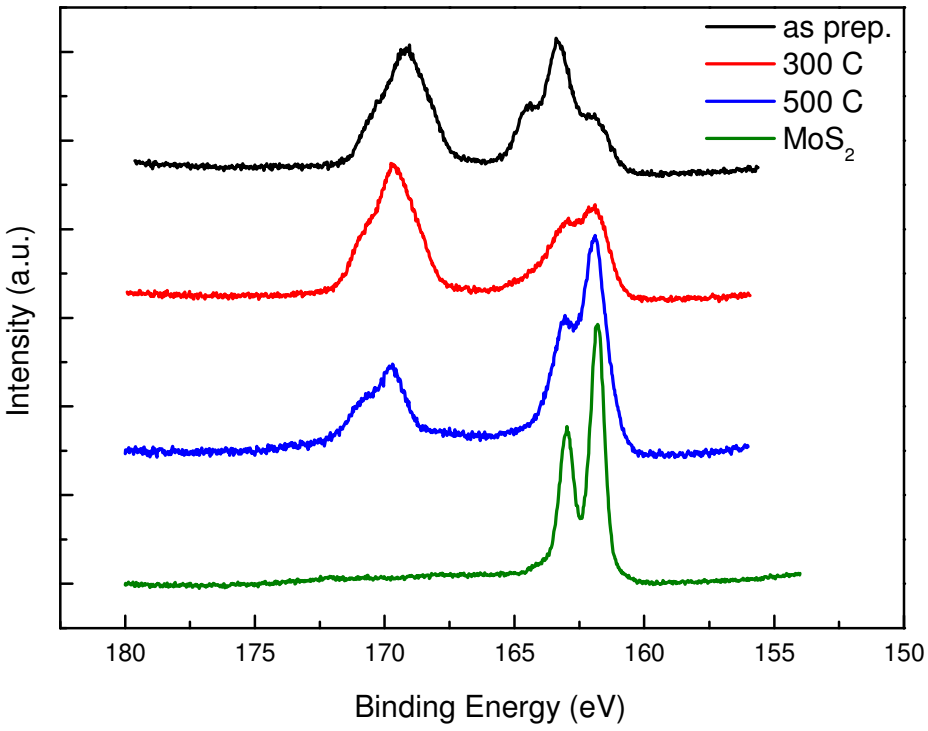

Figure 31. XPS data relative to the S2p region as a function of the annealing temperature

- When the medium is poorly oxidant, mostly Mo suboxides are observed. The S2p signals indicate the formation of few IF-MoS_2, while S-S bond is predominant.

- When no oxygen is available (laser ablation in n-decane), no MoS_2 are formed since no MoO_3 is produced during the plasma generated by the laser irradiation of the target. This assumption can be considered true if we assume that the absence of Mo signal is not due to carbon coverage, as discussed above.

Finally this work is an important study of the formation mechanism of nanostructures using pulsed laser ablation in liquids in which it's possible to notice the importance of the interactions between the species deriving from the ablation of the target, inside the plasma plume, and the species produced by the laser pulse with the solvent molecules.

2.2 MoS_2 layered materials

The electronic properties of ultrathin crystals of molybdenum disulfide consisting of N = 1, 2, ... 6 S-Mo-S monolayers have been investigated by optical spectroscopy. Through characterization by absorption, photoluminescence, and photoconductivity spectroscopy, Kin et al. was able to trace the effect of quantum confinement on the material's electronic structure. With decreasing thickness, the indirect band gap, which lies below the direct gap in the bulk material, shifts upwards in energy by more than 0.6 eV. This leads to a crossover to a direct-gap material in the limit of the single monolayer. Unlike the bulk material, the MoS_2 monolayer emits light strongly. The freestanding monolayer exhibits an increase in luminescence quantum efficiency by more than a factor of 1000 compared with the bulk material [3].

Exist different approaches to fabricate MoS_2 with small layer thickness. Some researchers produce it by mechanical exfoliation using the scotch tape method, others by chemical exfoliation with lithium intercalation and so on.

We decided to operate this synthesis in liquid phase by the using of solvents environmental friendly like isopropyl alcohol (IPA), n-methylpyrrolidone (NMP) and H_2O with a surfactant sodium dodecil sulphate (SDS). The using of the surfactant is necessary because the

surface tension of water is different from the energy between the layers which made of the structures of MoS_2 bulk material. In order to bring near this two parameters we had to use a surfactant in water.

First we dispersed MoS_2 powder (60mg) in the solvents (20ml) by ultrasonic bath at low power (100 W) in order to disrupt the material in an heterogeneous suspension. The sonic treatment was performed at 140W for 90 minutes.

After that we made a centrifugation with medium rcf (750) for 10 minutes in order to remove the big particles deriving from the bulk not disrupted.

In this way we obtained three different samples dispersed respectively in IPA, NMP and H_2O + SDS. Every samples are called “bulk” in UV spectra to distinguish them from the other samples exfoliated. Indeed after this step, we have obtained an homogeneous dispersion of MoS_2 bulk material.

The second step of this procedure was another ultrasonic bath treatment to start the real exfoliation. This time we worked at high power (around 180 W) for 3 hours, to forced the exfoliation of the material presents in the suspension. After the sonic treatments we centrifugated our samples with high rate (5400 rcf) and, in this way, we could eliminate the pieces more thick, obtaining a suspension of only few layer material.

We analyzed every samples by UV-VIS spectrophotometer and we obtained the following spectra (figures 32-33).

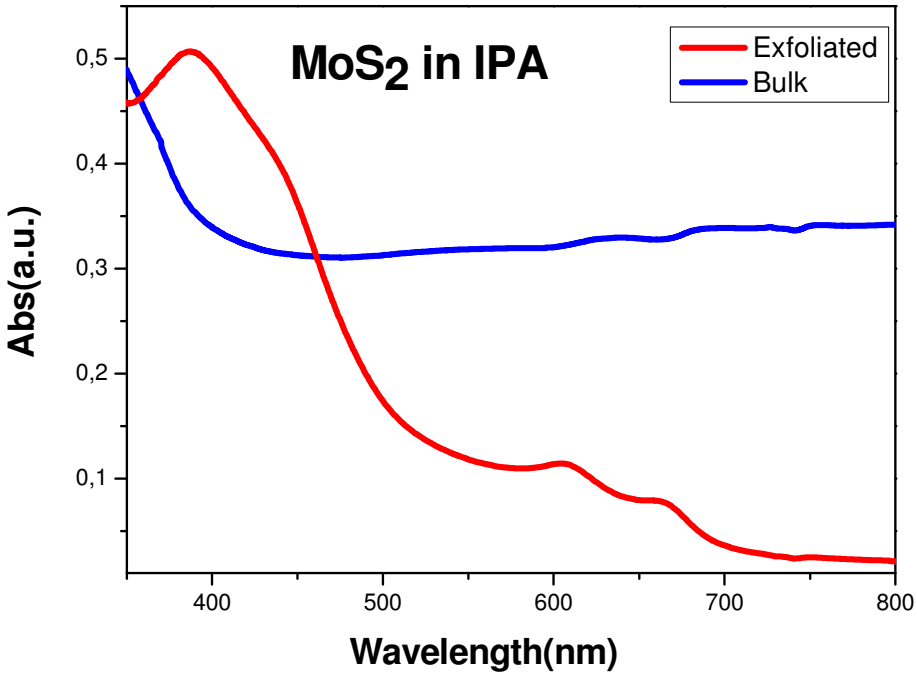

Figure 32. UV spectra of sample dispersed (blue) and exfoliated (red) in IPA

The spectra reported in figures 32 and 33 show a comparison between the spectrum of the samples after the first synthesis step (reported in black

line) and the spectrum of the samples after the second synthesis step (reported in red line).

It's possible to notice that from the spectrum in black line to the spectrum in red appear two signals at 620 and 650 nm respectively.

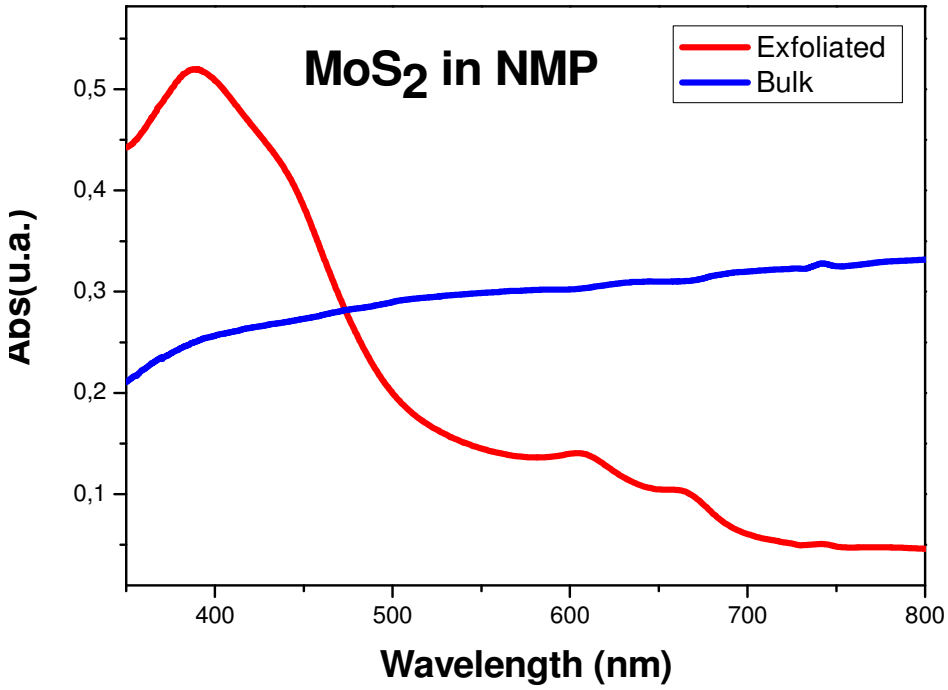

Figure 33. UV spectra of sample dispersed (blue) and exfoliated (red) in NMP

We can also observe the presence of another signals at around 415 nm. This signal it's attributed at the bulk material dispersed in the solvent.

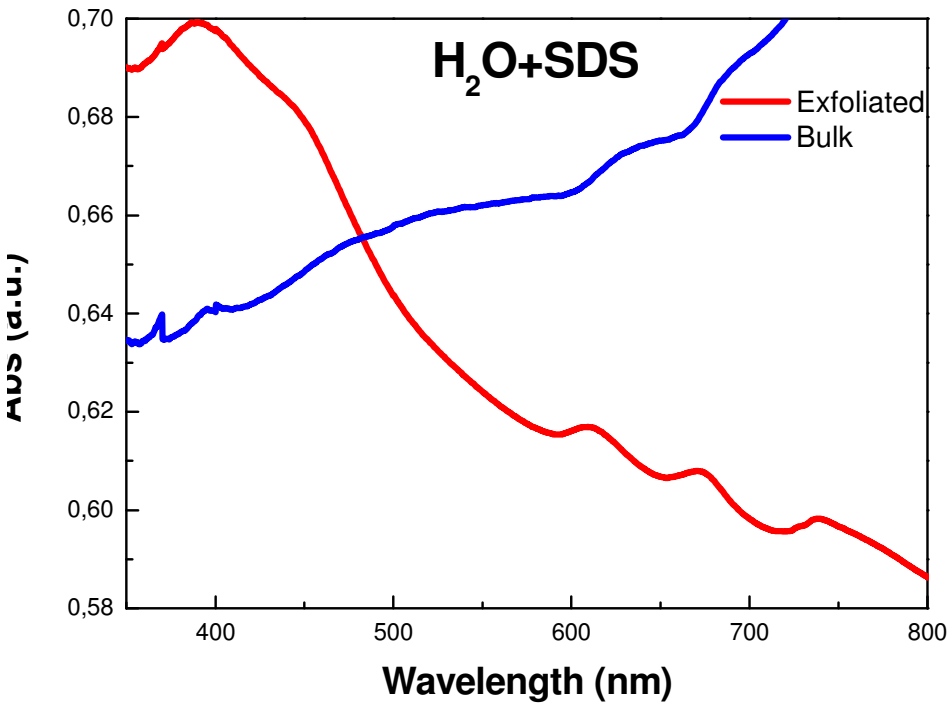

Figure 34. UV spectra of sample dispersed (blue) and exfoliated (red) in H_2O+SDS

In figure 34 it's reported the UV-VIS spectra of the material dispersed and exfoliated in water with the surfactant. Also in this case there is the presence of the two typical signals of MoS_2 layered material.

Comparison these results with the literature spectrum, it's clear that this signals are relative at layered material dispersed in solution.

Indeed, as reported in Fig 35, Coleman et al. [23] demonstrate that these signals are the excitons due to the layered materials and for this reason is an evidence of the presence in dispersion of few-layer of MoS_2.

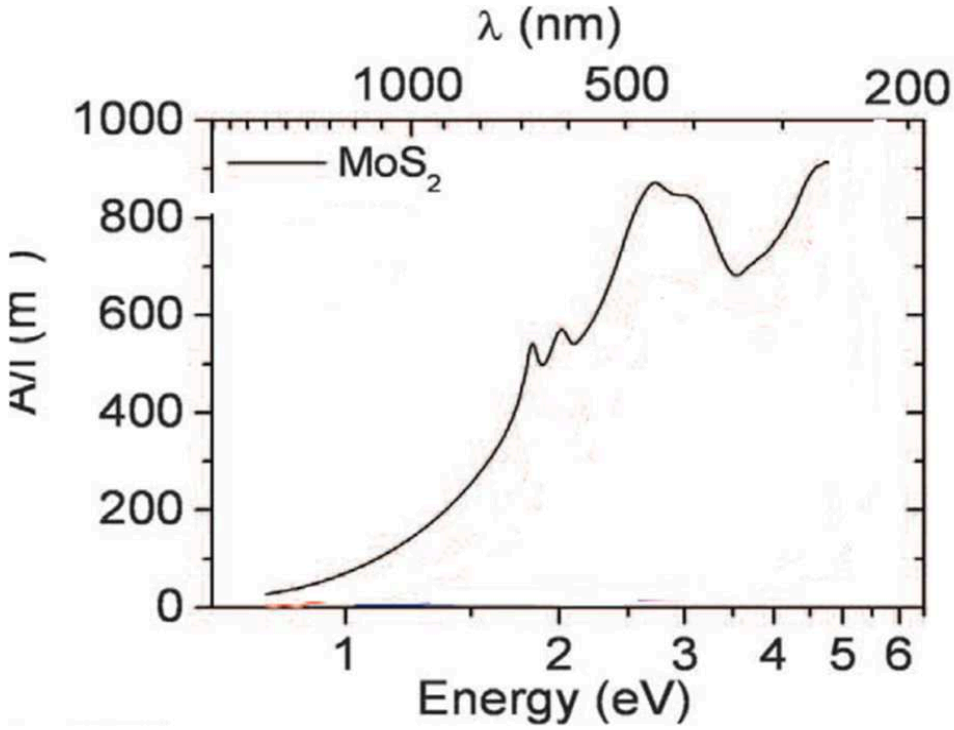

Figure 35. UV analysis of MoS_2 few-layer material reported in literature

Indeed this two prominent absorption peaks can be identified at 670 and 627 nm in the spectrum. These two resonances have been well established to be the direct excitonic transitions (Figure 36a inset) at the Brillouin zone K point by Splendiani et al. Their energy difference is due

to the spin-orbital splitting of the valence band, and the two resonances are known as A1 and B1 excitons, respectively.

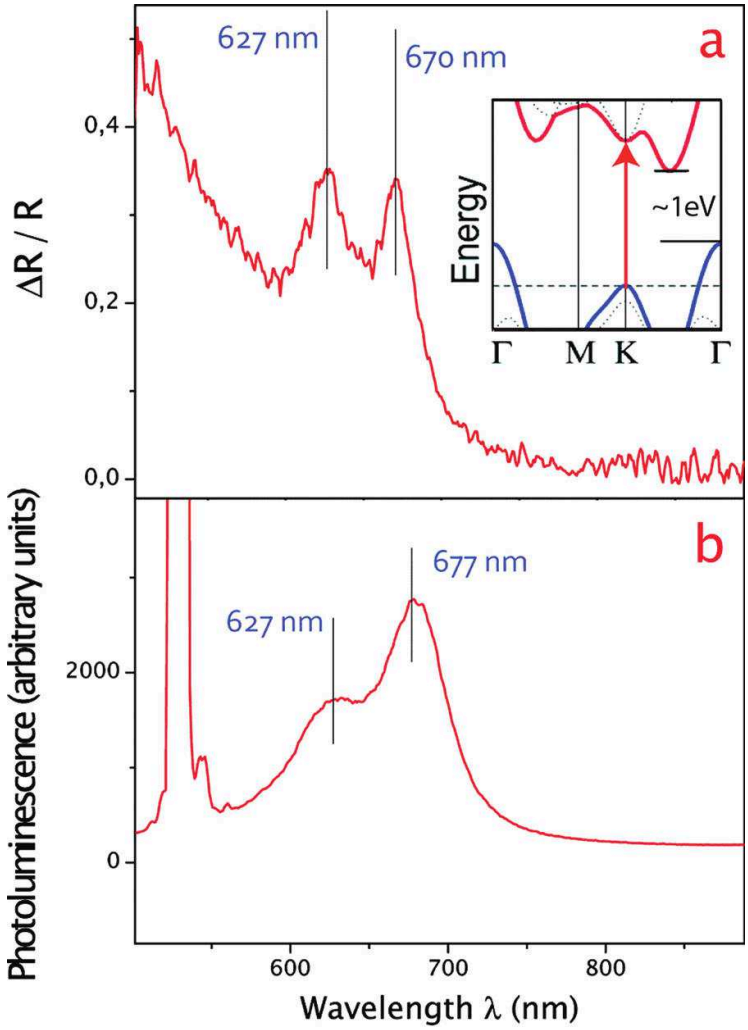

Figure 36. Reflection and photoluminescence spectra of ultrathin MoS_2 layers

Optical absorption at energies between the direct excitonic transitions and the indirect bandgap (~ 1 eV) is very weak. For thin layers of MoS_2, absorption peaks from the direct excitonic states exhibit little change with layer thicknesses [24].

This is the first result of the good exfoliation of our systems but at this point we decided to deposit this materials onto a substrate (silicon) to make morphologic analysis by the using of Atomic Force microscopy (AFM).

We decided to employed three different deposition methods and in particular we used drop casting, deep submerging and aerographic method of the substrate. The first method consists in a simple deposition of a solution drop onto the substrate but in this way we cannot control the order of the nanostructures packing in the solid phase. In the second method the substrate is submerged inside the solution for ten times and it stays in solution for thirty seconds for each submersions. Also in this case we cannot control the arrangement of nanostructures on the surface of the substrate. The last method that we analyzed is the aerosparying and with this technique it's possible to deposit a small amount of material and in this way there are not packing events and we can obtain an homogeneous deposition onto the surface of substrate. After this research we deposited all samples and we performed AFM analysis and I reported the relative results below.

I would to underline that the AFM analysis is operated in tapping mode to avoid the possibility to destroy the layers obtained after the exfoliation procedure.

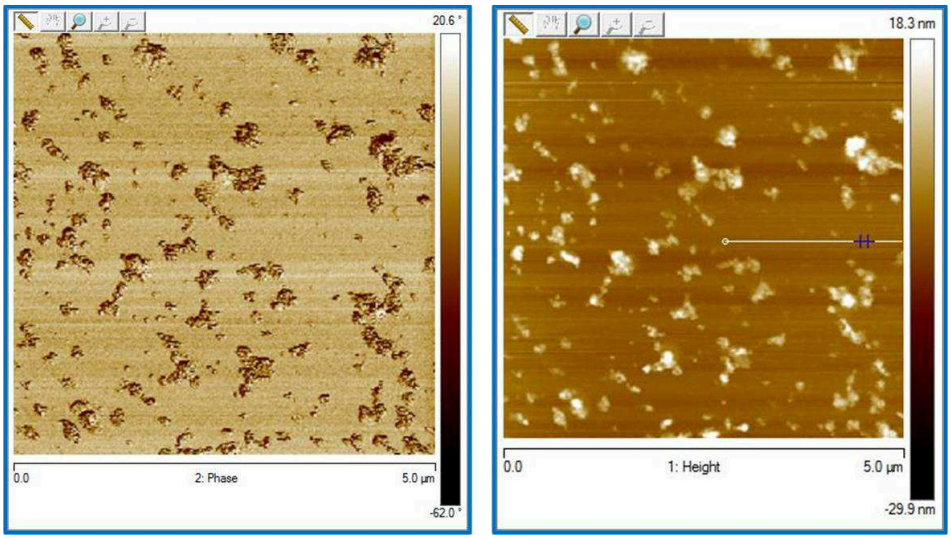

Figure 37. AFM images of MoS_2 exfoliated in IPA

On the left side in the figure 37 we can observe the phase analysis of the sample obtained in NMP. With this technique we obtain information on the density of our deposit. The darkest part in the image is represented by silicon substrate which presents the some density while the lightest is made of the MoS_2 layers. On the right side I show the height analysis in which the darkest part represents the lower part of deposit while the lightest part represents the higher part of the deposit.

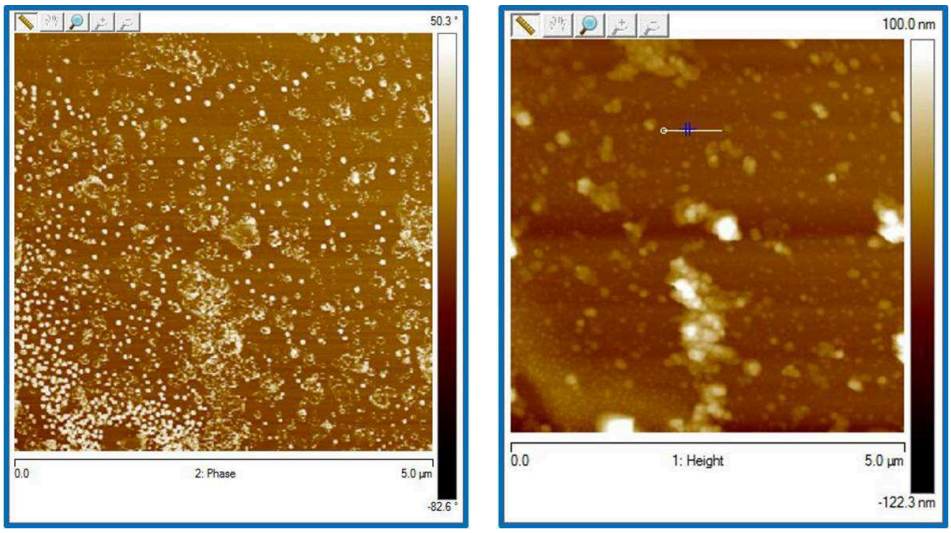

Figure 38. AFM images of MoS_2 exfoliated in NMP

Analyzing the images reported above it's possible to notice the correlation between the structures with highest density (in the left side of the image 38) and the structures having highest height (in the right side of the image 38).

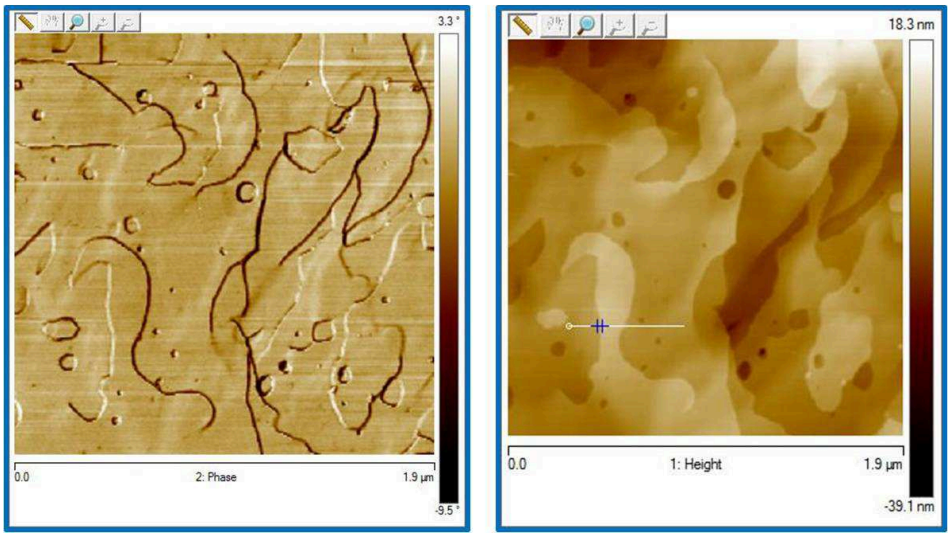

Figure 39. AFM images of MoS_2 exfoliated in H_2O+SDS

In the figure 39 it's reported the AFM analysis for the sample obtained in water with the surfactant. After these considerations we operated the thickness analysis and I reported the results below.

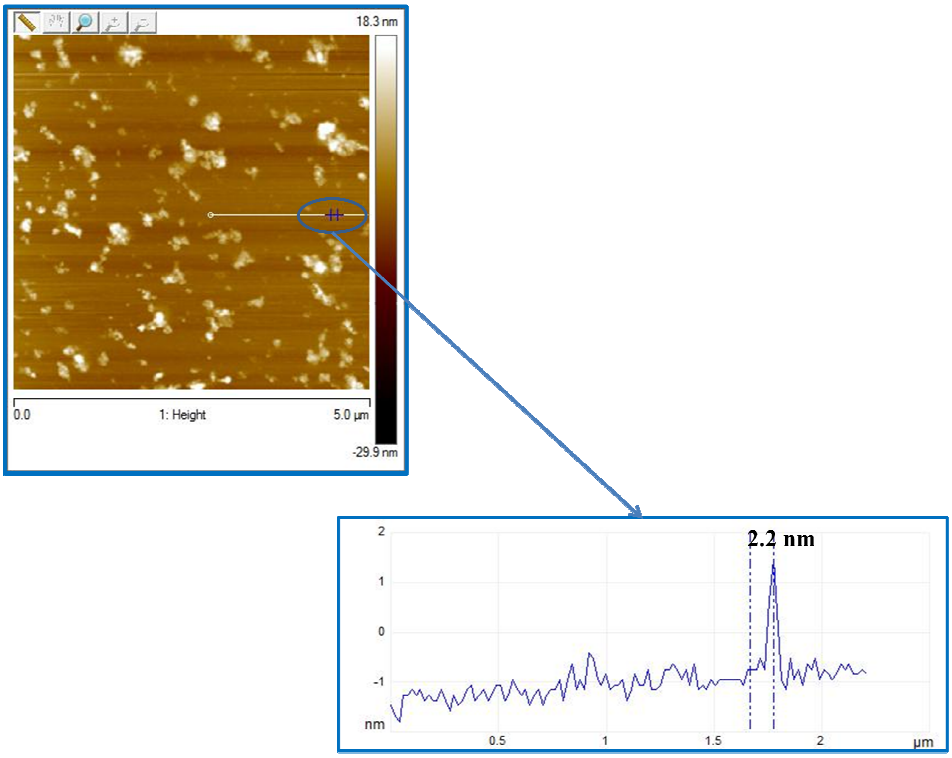

Figure 40. Section analysis of layered material obtained in IPA

Analyzing the thickness of the sample obtained using IPA as a solvent we obtained thickness values lower than the samples prepared in NMP and this result it's shown in fig. 40 IPA. It's clear, from the section analysis, the thick of around 2.2 nm corresponding to more or less 4 layers.

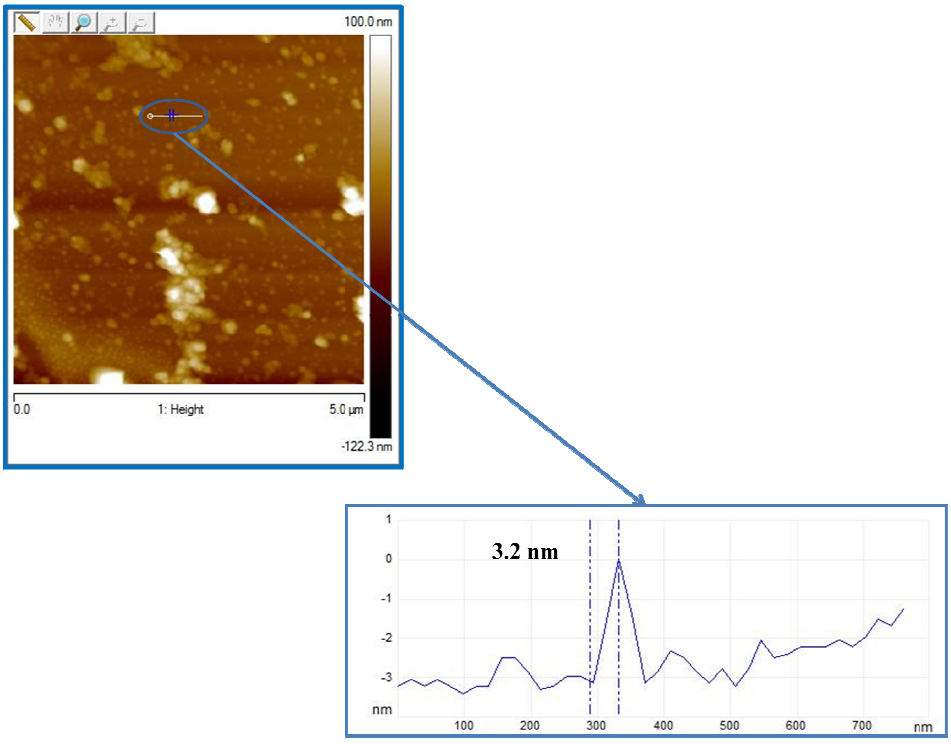

Figure 41. Section analysis of layered material obtained in NMP

In the case of the sample exfoliated in NMP (figure 41) we notice the presence of some pieces of deposit having thickness of approximately 3.2 nm. Considering that one layer of MoS_2 is thick around 0.6 nm these pieces corresponding to more or less 5 layers.

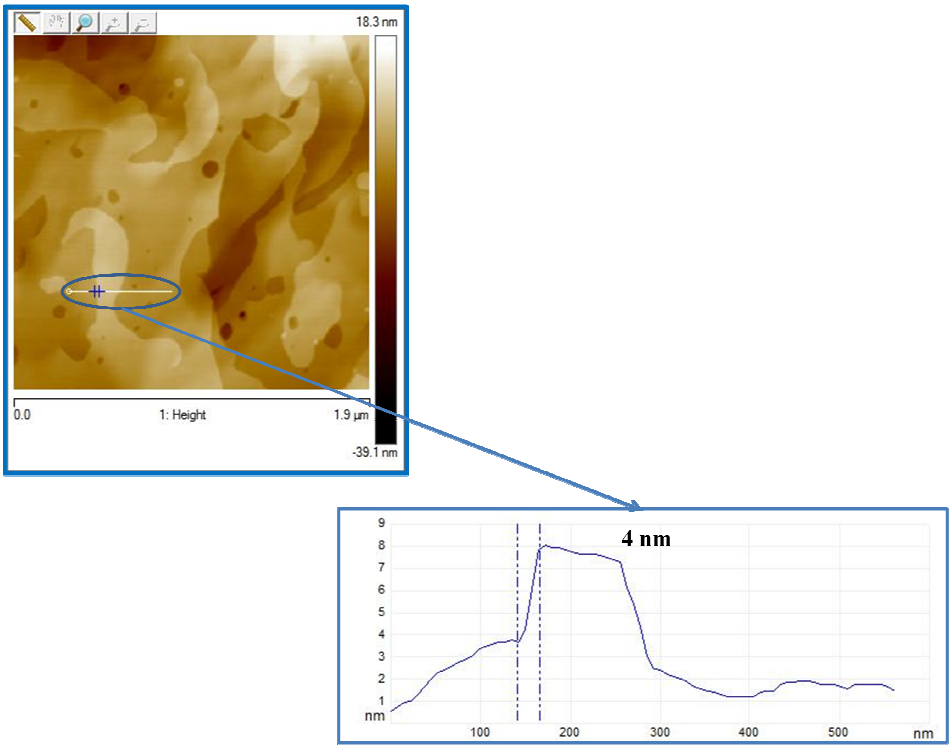

Figure 42. Section analysis of layered material obtained in H_2O+SDS

The sample exfoliated in water with surfactant (SDS) (figure 42) presents the most of the pieces produced with thickness of approximately 4 nm corresponding to 7 layers.

With this analysis we can conclude that the sample more thin is the sample produced in IPA.

For this reason we decided also to perform confocal Raman imaging analysis of this sample to verify the vibrational features and I reported the relative spectrum in the figure below (fig. 43) the two main signals relative at MoS_2 feature are nearer each other in the case of layer material

than the case of bulk as it's possible to understand through the work conduct by Najmaei et al. [25]

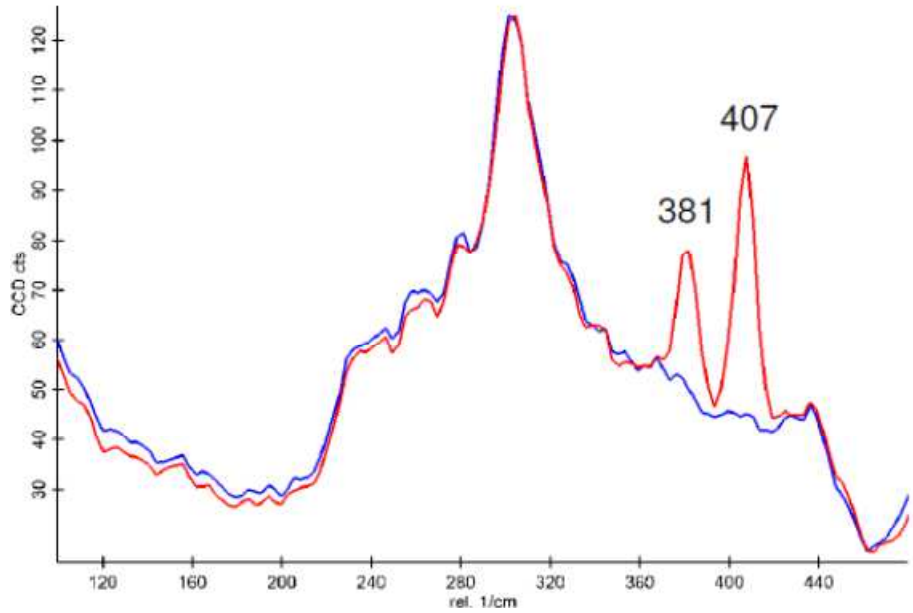

Figure 43. Raman spectra of MoS2 (red line) and the substrate (blue line)

If we paragon the relative distance between two typical MoS_2 signals in the case of bulk material and layered material we can notice that in our case we obtained layered material (fig. 44).

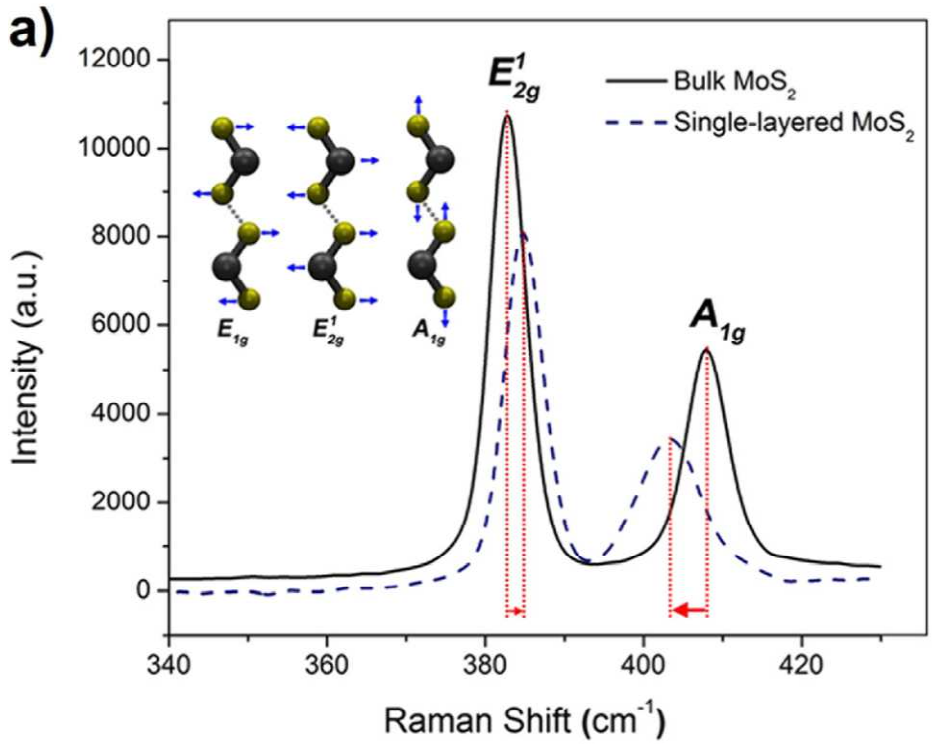

Figure 44. Raman spectra of bulk MoS_2 and a single-layer MoS_2 flake on SiO_2 substrate. Inset: illustration of the three Raman Active modes: E_{1g}, E^1_{2g}, and A_{1g}. Molybdenum atoms are in black and yellow represents sulfurs

Finally we demonstrated that the exfoliation assisted by ultrasound treatments and following centrifugation is a valid technique to produce layered materials. Moreover this method allow to produce pure material without any external reagent or sub products avoiding the purification cycles.

REFERENCES

[1] Lebegue et al. *Physical Review B*, (2009), **79**, 115409-1-115409-4

[2] Gmelin Handbook *Springer-Verlag*, (1995)

[3] Kin Fai Mak et al. Atomically thin MoS2: A new direct-gap semiconductor

[4] Novoselov et al. *Proceedings of the National Academy of Sciences U.S.A.,*(2005), **102**, 10451-10453

[5] Wu et al. *ACS Nano,* (2011), **5**, 1276-1281

[6] Remskar et al. *Advanced Materials*, (1998), **10**, 246-249

[7] Sajti et al. *Journal of Physical Chemistry C*, (2010), **114**, 2421-2427

[8] Yang et al. *Progress in Materials Science*, (2007), **52**, 648-698

[9] Ashfold et al. *Chemical Society Reviews*, (2004), **33**, 23-31

[10] Bekefi et al. Principles of laser plasmas. (1976) New York: Wiley

[11] Balasz et al. *Analytical Chemistry,* (1991), **63**, 314-320

[12] Peyer et al. *Journal of Applied Physics*, (2000), **30**, 498-501

[13] Berthe et al. *Journal of Applied Physics* (1999), **85**, 7552-7556

[14] Wiesel et al. *Nano Research*, (2009), **2**, 416-424

[15] Yin et al. *Material Letters*, (2007), **61**, 1303-1306

[16] Mafuné et al. *Journal of Physical Chemistry B*, (2001), **105**, 5114-5120

[17] Therese et al. *Solid State Science*, (2006), **8**, 1133-1137

[18] Zak et al. *Journal of American Chemistry Society*, (2000), **122**, 11108-11116

[19] Weber et al. *Journal of Physical Chemistry*, (1996), **100**, 14144-14150

[20] Moulder et al. *Handbook of X-ray Photoelectron Spectroscopy*, Perkin-Elmer Corp, Eden Prairie, MN, USA, (1992)

[21] Steudel et al. *Topics in Current Chemistry Springer*, (2003), 153

[22] Amendola et al. *Journal of Physical Chemistry C*, (2011), **115**, 5140-5146

[23] Coleman et al. *Science*, (2011), **331**,568-571

[24] Splendiani et al. *Nano Letters*, (2010), **10 (4)**, 1271-1275

[25] Najmaei et al. *Applied Physics Letters*, (2012), **100**, 013106-1-013106-4

3 SYNTHESIS AND CHARACTERIZATION OF CARBON NANOWALLS

As said before carbon nanowall is very interesting material because it's made of graphene layers and shows some intriguing properties in field emission, catalysis and electrochemical applications. Usually this material is prepared with plasma enhanced chemical vapour deposition and it's growth onto the substrate, prevalently silicon wafer. We employed the synthesis of this material through the using of laser ablation in liquid with an electric field in order to obtain these nanostructures in liquid phase and on all substrate.

We noticed the deposition of CNWs during a laser ablation experiment conducted in water in presence of a suitable electric field. The electric field is through to transport the charged particles produced in the plasma plume at the electrodes in a process which resembles electrophoresis. Indeed Electrical field-assisted Laser Ablation in Liquids (ELAL) has been recently proposed as a new approach to controllably fabricate oxide micro-and nanoparticles with various shapes which has been collected from the colloidal suspensions [1]. Here we demonstrate that the exotic carbon species formed during the ablation are able to reach the electrodes and form an uniform foils carpet.

In our experiments we have used a Nd:YAG laser beam (5 nsec pulse duration, 532 nm radiation wavelength, 10 Hz repetition rate) focused onto a polycrystalline graphite target (5 J/cm^2) which has been previously fixed at the bottom of a flask and submerged by a few centimetres of Millipore grade distilled water.

We decided to use this synthesis method because we know that during the ablation with a Nd-YAG of a target made of graphite in water the polyynes species are produced. Polyynes are linear carbon chains with a number of carbon atoms from 4 to 22. This materials, as reported in literature [2], are very unstable as reported in Raman spectra in figure 45.

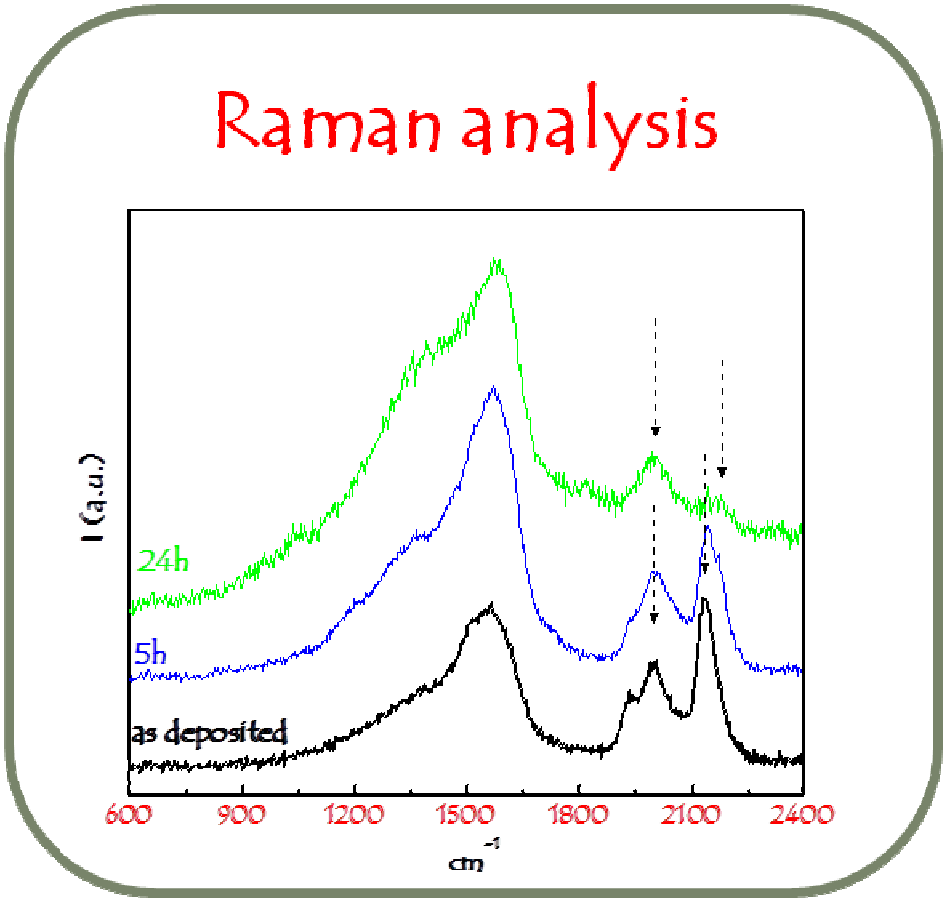

Figure 45. Raman analysis of polyynes stability

From the figure it's possible to know the instability of these systems indeed after 24 h the characteristic signals of polyynes at around 2100 cm^{-1} are disappeared. This instability means also reactivity and for this reason we decided to use this molecules like building blocks for the formation of some different nanostructures.

During the ablation two HOPG electrodes have been immersed in the liquid in such a way to face their basal planes (see fig.46).

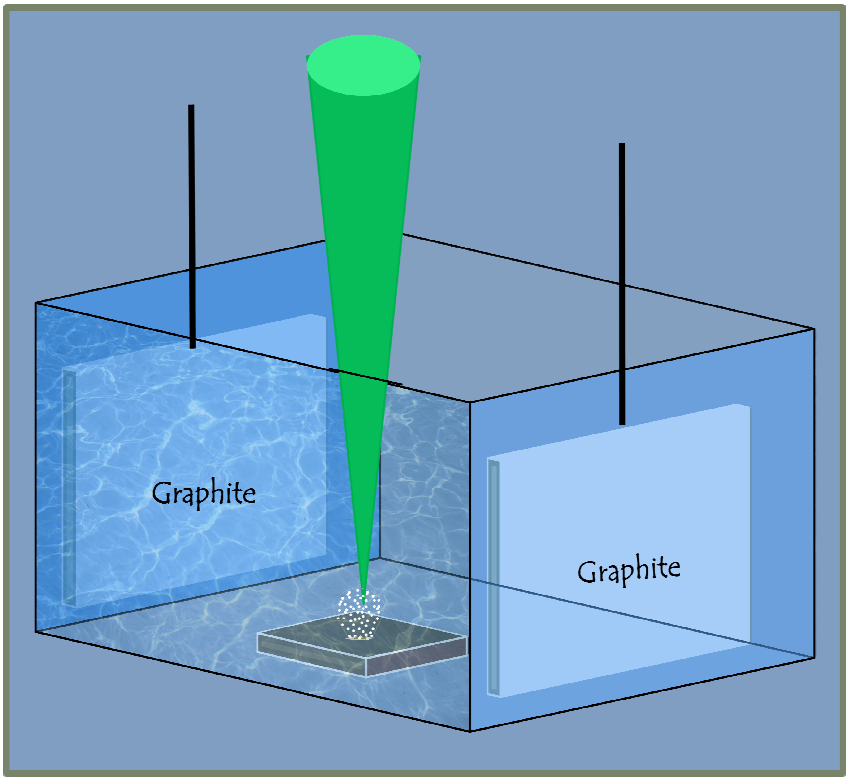

Figure 46. Typical experimental setup for an ELAL experiment

The two electrodes have been charged by applying a 30 V DC potential and, between them, the plume has been left to develop during the ablation. The experiments have been performed at different deposition times from a few minutes up to 2 hours and the electrodes temperature has been monitored both before and after the deposition. It has been

found a moderate increase during the overall process, compatible with the temperature increase of the liquid due to the ablation phenomena (less than 10 °C in two hours) [3].

Fig. 47 shows some electron microscopy images (SEM and TEM) taken on the positive electrode, after 20 min. and 2 hours ablation.

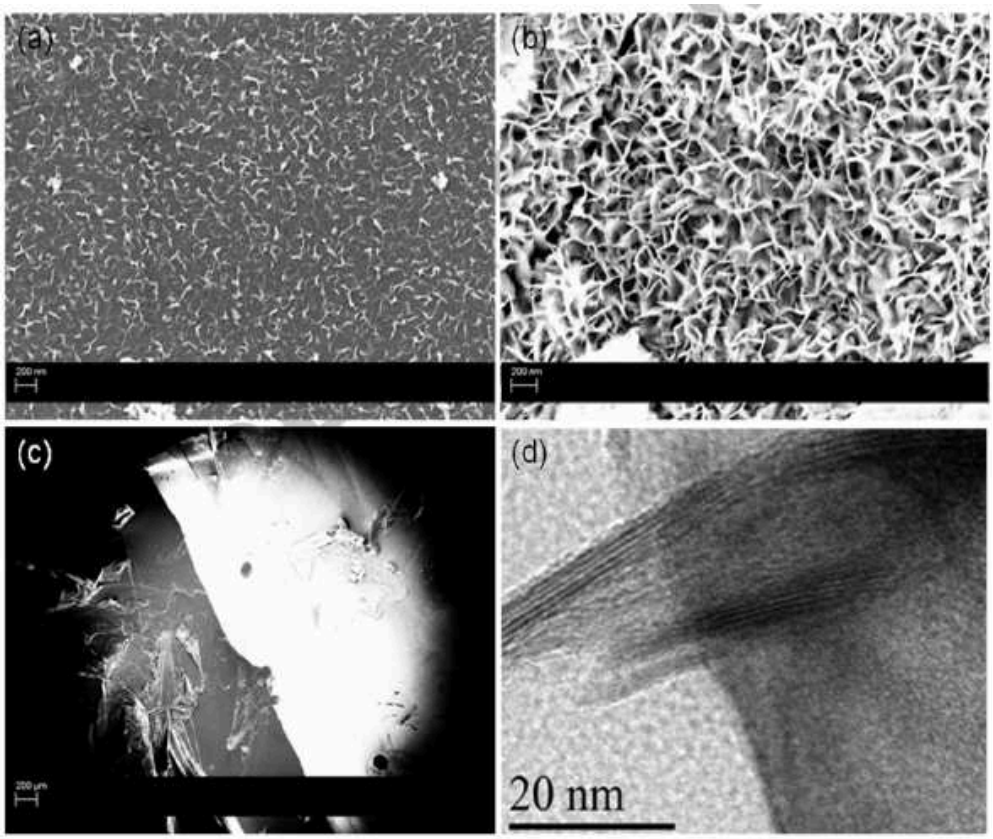

Figure 47. SEM of CNWs deposited after 20 min. (a) and 2h (b) ablation. We also report a the dipping interface and an HR TEM the image of the walls

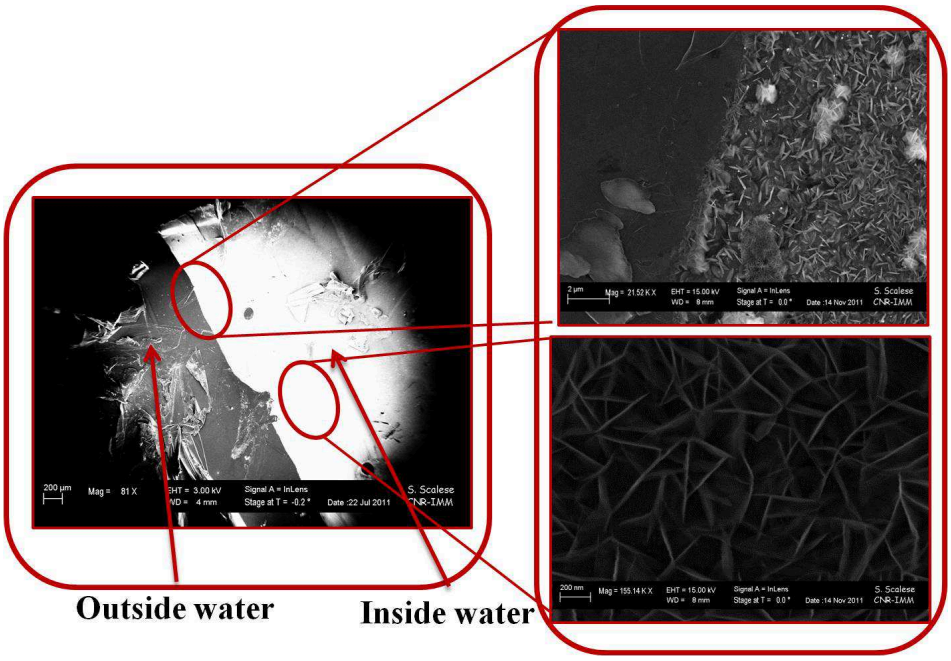

Figure 48. SEM analysis of positive electrode

In the figure 48 reported above It's shown on the left side the large area SEM of the positive electrode and on the right side the SEM of the particulars evidenced by red circles. On the top of left side it's possible to notice the front of the solvent. Outside from the solvent we have not nanostructures otherwise inside the solvent we have the presence of nanostructures. Another zoom of these nanostructures it's reposted in the bottom of the right side of the figure 48

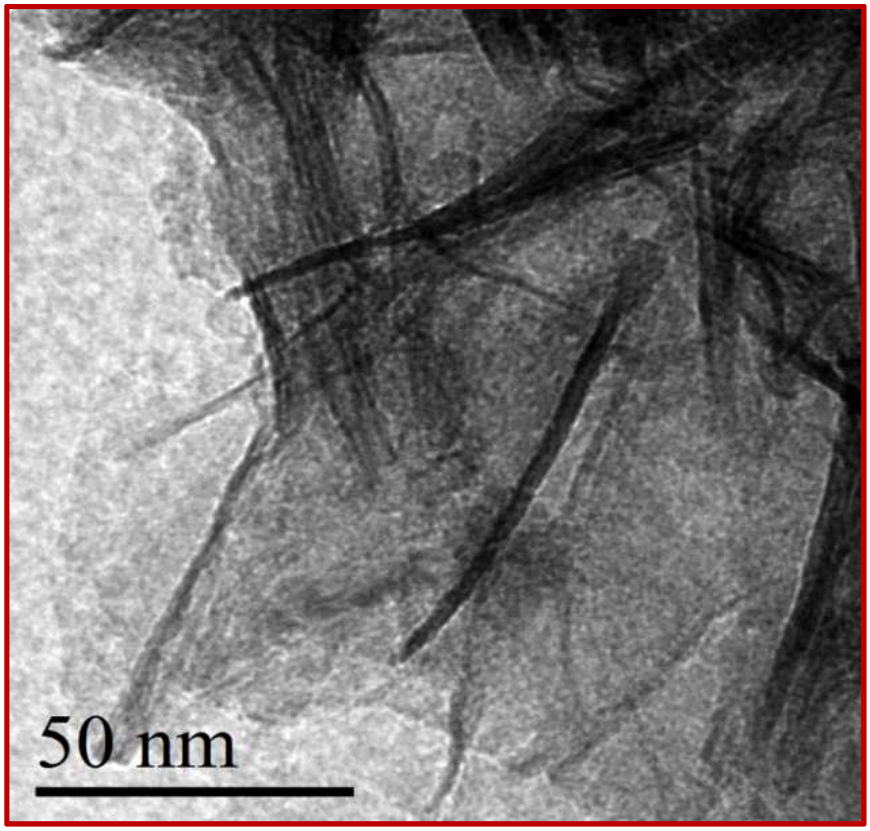

Figure 49. TEM analysis of CNWs

These images are related to the HOPG surface facing the ignited plasma plume and reveal that the electrode is uniformly covered by nanowalls (fig. 47a). By increasing the ablation time, the deposit continues to growth with a growth rate of about 2 nm/min. In particular fig. 47b reports the situation after 2 h ablation. The carbon foils, just grown after 20 min, are now more evident and form a uniform forest on top of the HOPG surfaces. This uniformity has been also evidenced at low magnification in fig. 47c. Here the borderline of immersion for the

positive electrode is clearly observed since the bright area represents the CNWs deposit. Finally, fig. 47d displays a high resolution TEM image of the walls showing the stacking of few high quality graphene layers. Another zoom of TEM image of this deposit is shown in figure 49.

At the negative electrode the presence of graphene-like structures is less clear and the surface seems to be covered by carbon particles, probably in the amorphous state fig 50.

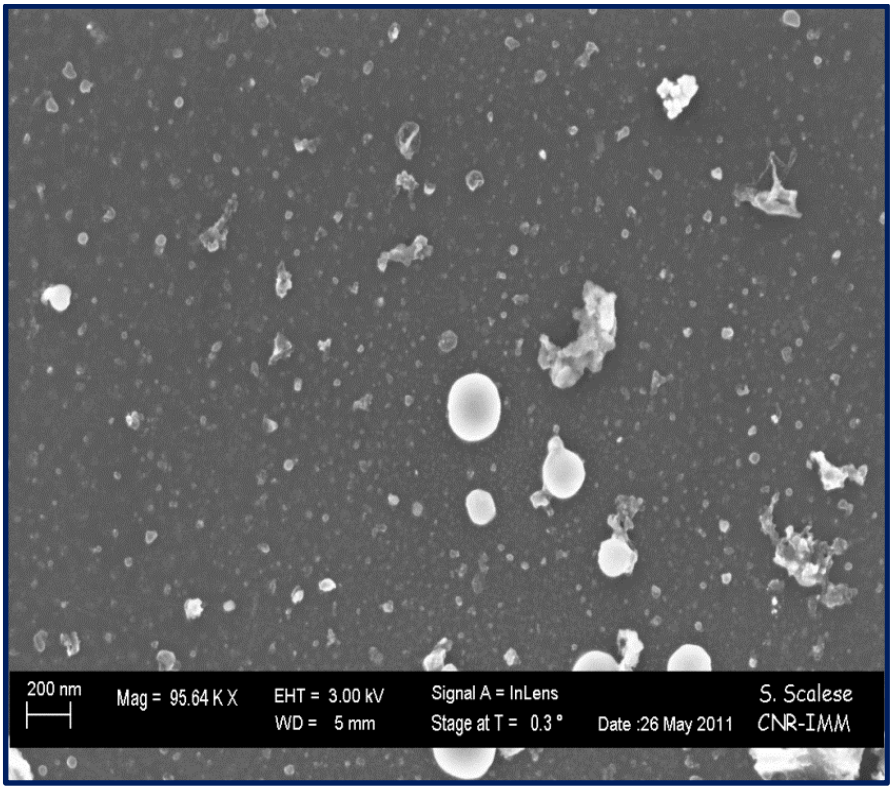

Figure 50. SEM analysis of negative electrode

This behavior can be explained considering the orientation of the solvent around the polyyne chains. The chains are rich of electrons and this phenomena produces a possible orientation of water molecules as reported in figure 51

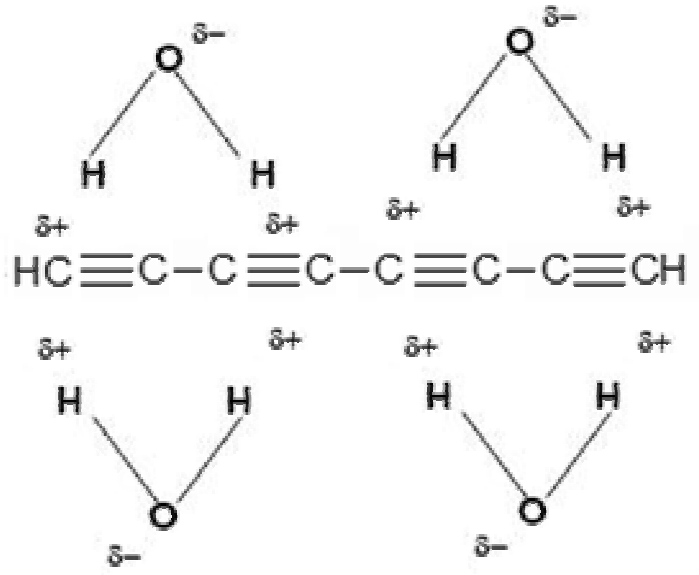

Figure 51. Hypothesis of water coordination of polyynes in solution

This orientation forms a partial negative change in the system and for this reason we noticed the deposit only on the positive electrode.

We performed Raman analysis of CNWs obtained with PLAL with EL and the results are shown in fig. 52. It's clear that the signals of CNWs are different than the signals of graphite materials and this is a proof of the formation of another material onto the electrode.

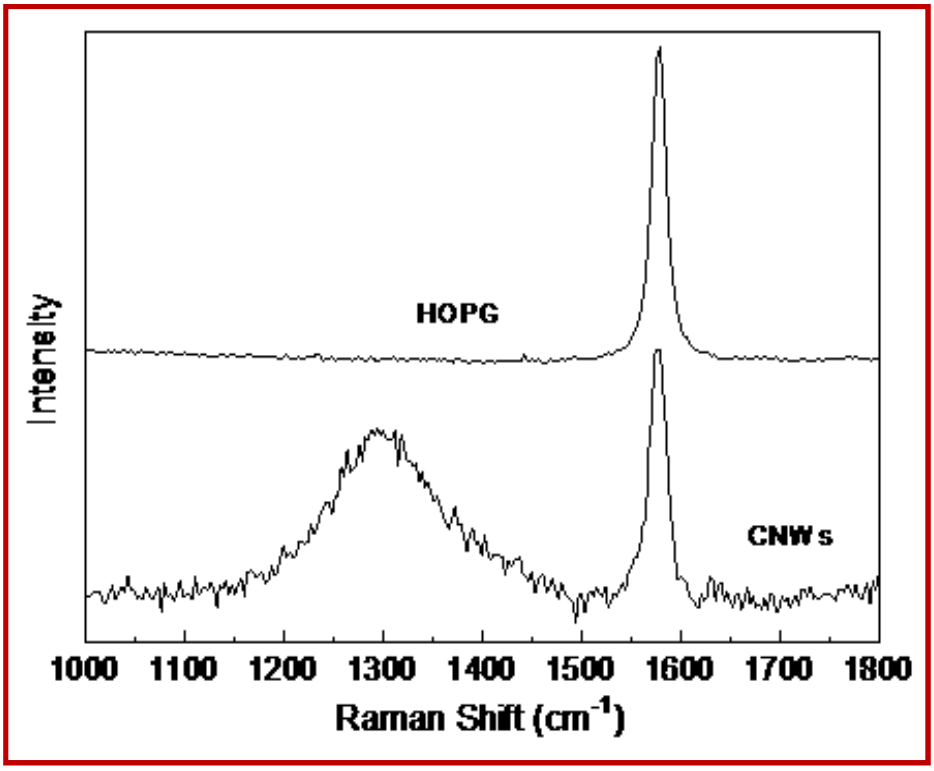

Figure 52. Raman analysis of the positive electrode

The signal at around 1300 cm^{-1} is representative of CNWs structures.

The chemical state and the structure of the nanowalls have been investigated by X-ray Photoelectron Spectroscopy (XPS) and Raman spectroscopy. The results are reported in fig. 53.

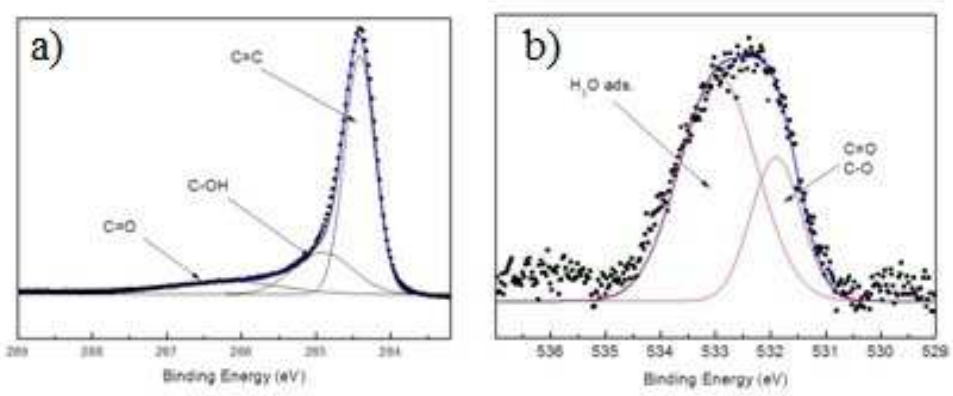

Figure 53. XPS analysis of the deposit onto the positive electrode

The C1s and O1s XPS spectra are shown in Fig. 53 a and b respectively. Curve fitting of the C1s and O1s spectra was performed using a Gaussian-Lorentzian peak shape after performing a Shirley background correction. The binding energy of the C–C is assigned at 284-284.5 eV and chemical shifts of +1 and +2 are typically assigned to C–OH and C=O functional groups respectively. These data reveals that CNWs are mostly reduced with negligible oxidation. Moreover the analysis of O1s region indicates the presence of adsorbed H_2O, probably trapped inside the walls.

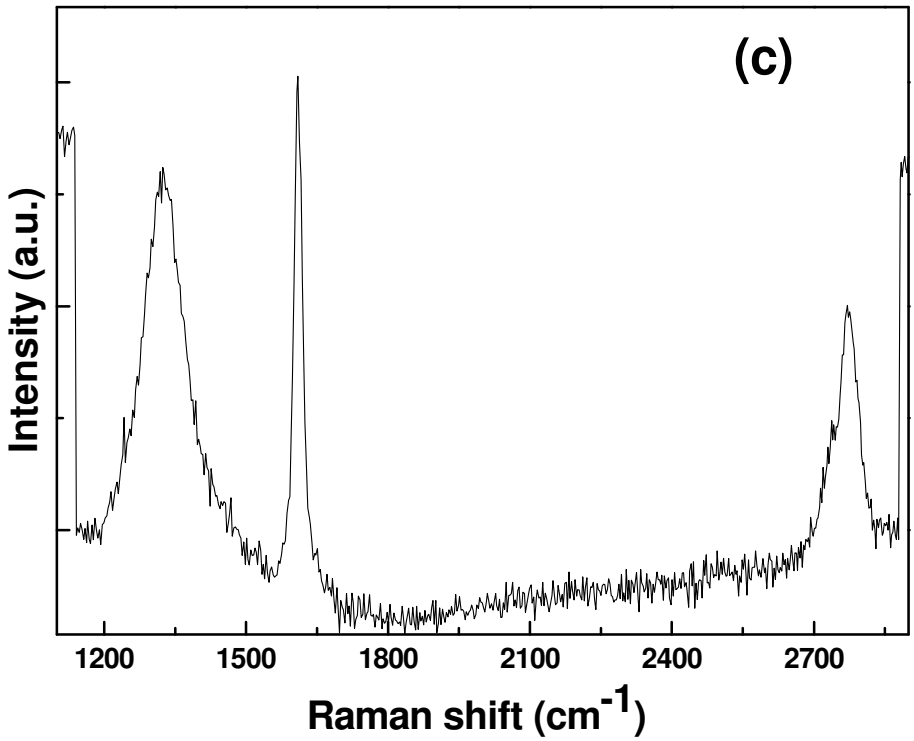

Figure 54. Raman analysis of CNWs

The structure of the deposit is well represented by the Raman spectrum reported in fig. 54. As already reported by Kurita et al. [4], the Raman spectra of CNWs exibit G and D bands at 1580 and 1350 cm^{-1} with a bandwidth relatively narrow, even when the ID/IG intensity ratio is significantly high. This feature is distinguished from those of typical graphitelike carbons [5] and suggest that the nanowalls are composed of small crystallites with a large degree of graphitization. Fig. 54 also

reports the presence of a 2D signal located at 2780 cm^{-1}, consistently with the presence of few layer graphene domains.

We want now comment on the possible mechanism of formation and deposition of the CNWs in such an electric-field assisted laser ablation in water which can be also useful for general considerations on the growth of CNWs using different deposition methods.

We start considering that the formation of exotic carbon species during the ablation of a graphite target in a liquid environment has been extensively reported by many authors in the last few years.

When the ablation is conducted in water the main species detected are hydrogen capped polyynes [6] while ablation in organic solvents leads also to the observation of polyynes together with polycyclic aromatic hydrocarbons and related structure [7].

As a matter of fact polyyne chains (generally stable only for few hours) are considered as precursors of a large number of carbon nanomaterials such as fullerenes and nanotubes. Moreover it is well known that nanoparticles and nanostructures produced by laser ablation in liquids are electronically charged either because of their generation or because of salvation processes which gives to the particles a certain z-potential. For instance it has been reported that oxidized CNT colloids are negatively charged and are attracted by the positive electrode. It is then plausible that negatively charged polyynes migrate at the anode and start to built up a complex structure such as that observed by electron microscopy.

This hypothesis is corroborated by a series of observations which have been done either on the water solution and on the electrodes after the

ablation. For instance it has been found that the concentration of the polyyne solution after the experiment in which the electric field is applied is much lower than that commonly observed [8] during a classical laser ablation experiment in water when no electric field is applied. As in the case of nanotubes growth during arc discharge, a key parameter is the presence of an electric field associated to the plasma. This has been widely discussed by Wu et al. [9], following Plasma Enhanced Chemical Vapor Deposition experiments. In those cases the presence of a plasma coupled with a CVD process enables the formation of carbon radicals similar to those which are assumed to initiate the growth of either polyynes and carbon nanotubes during laser ablation and arc discharge experiments [10].

We are actually investigating on the role of the electric field strength, the role of the negative electrode and the geometry on such a kind of experiments. Preliminary results indicate that the defects which naturally reside at the electrode surface (kinks, graphite plane edges, and so on) serve as nucleation sites for the growth of the nanostructures.

REFERENCES

[1] Pu et al. *ACS Nano*, (2011), **5**, 4748-4755

[2] Compagnini et al. *Journal of Raman Spectroscopy,* (2008), **39**, 177-181

[3] Menendez-Manjon et al. *Journal of Physical Chemistry C*, (2010), **114**, 2499-2504

[4] Kurita et al. *Journal of Applied Physics*, (2005), **97**, 114302-1-114302-11

[5] Compagnini et al. *Applied Physics Letters*, (1992), **61**, 1796-1798

[6] Compagnini et al. *Carbon*, (2007), **45**, 2456-2458

[7] Cataldo et al. *Carbon*, (2004), **42**, 129-142

[8] Matsutani et al. *Chemical Communications*, (2011), **47**, 5840-5842

[9] Yihong et al. *Nano Letters*, (2002), **2**, 355-359

[10] Scuderi et al. *Carbon*, (2009), **47**, 2134-2137

4 SYNTHESIS AND CHARACTERIZATION OF TWO DIMENSIONAL HYBRID SYSTEMS MoSI+Au

Metal-chalcogenide-halide nanowires belonging to the general formula$Mo_6S_{9-x}I_x$ (MoSI) have been so far successfully synthesized and purified indifferent stoichiometries [1]. These materials can be obtained by a single-step process and consist of subnanometer diameter nanowires that self-assemble into weakly bounded bundles. The major reason of interest for these quasi-one-dimensional objects lies in the fact that they nicely complement carbon nanotubes in many applications such as in the detection of biomolecules [2] and present identical (metallic) electronic properties which are believed to be independent of their structure, as suggested by both theoretical and experimental studies [3]. Moreover, the conductive bundles can easily be dispersed and debundled in common organic solvents down to individual nanowires [4]. For all of these reasons, MoSIs are considered promising for applications as field emission tips, nanotribological applications, and biological fields.

Recently, it has been shown that solution-processed attachment of gold nanoparticles (GNPs) to MoSI produces self-assembled inorganic

networks in a scale-free self-organized critical state [5]. This gives a great opportunity for exploring the novel properties of MoSI materials for the fabrication of nanodevices and foresees the possibility to make these nanonets candidates for sophisticated data processing systems such as the human brain [6]. Since the key construction element of the nets is given by the metal-nanowire chemical connectivity, a detailed study of the bonding state between them is of paramount importance.

The first step to obtain the nano-network is the synthesis of MoSI and gold nanoparticles. For the preparation of MoSI I went to the Josef Stefan Institute at Ljubljana where I studied the growth of this nanowires. Indeed this material, with standard synthesis parameter, grows in bundles with micrometric diameters, as shown in previous chapter. Dimensions of these systems are important parameters in nano applications. To use MoSI NWs in nanoelectronic, for instance, purification and extraction procedures are necessaries to obtain a material with proper characteristics for devices. However, after this treatment, only the 1-5% of the raw material is still useful. The amount of thin bundles obtained with the "classic" method is of a few percent. For this reason, the main goal of my mission was to find proper conditions of synthesis, which allow increasing the quantity of the thin bundles. The "classic" synthesis reaction is based on a thermal treatment at high temperature (1050°C) fig. 55.

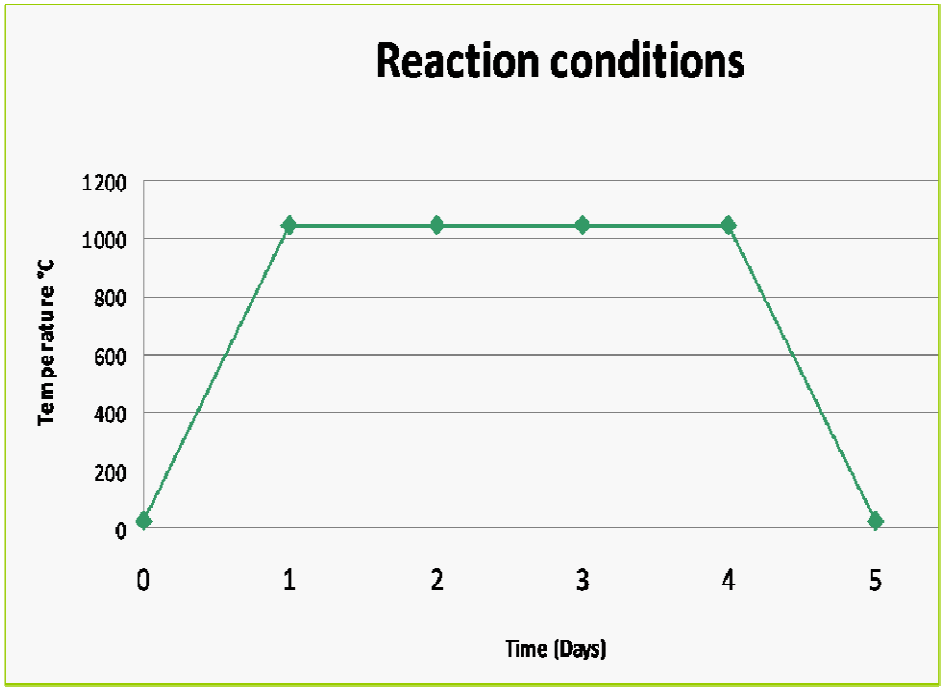

Figure 55. Diagram of standard reaction conditions

Main variables of reaction are the following: temperature of reaction, speed of heating, period of treatment, amount of starting material, and the stoichiometry of elements.

During my visit I prepared four sets of samples, changing the quantity of material inside the reaction vessel and their ratios in order to obtain different stoichiometries.

The first set is:

P1 = $Mo_6S_3I_6$ (1.85g)

P2 = $Mo_6S_{4,5}I_{4,5}$ (1.57g)

P5 = $Mo_6S_3I_6$ (0.37g)

The second set is:

P3 = $Mo_6S_3I_6$ (1.85g)

P4 = $Mo_6S_{4,5}I_{4,5}$ (1.57g)

P6 = $Mo_6S_{4,5}I_{4,5}$ (0.31g)

First set was prepared at 1050°C, while the second one was prepared at 850°C. The speed of heating was decreased respect to speed of the "classic" reaction in order to slow down the growing of these systems, obtaining thinner bundles. Final temperature was reached in two days, the reaction temperature was carried on for two days and the decreasing temperature ramp lasted for one day. (See Fig. 56)

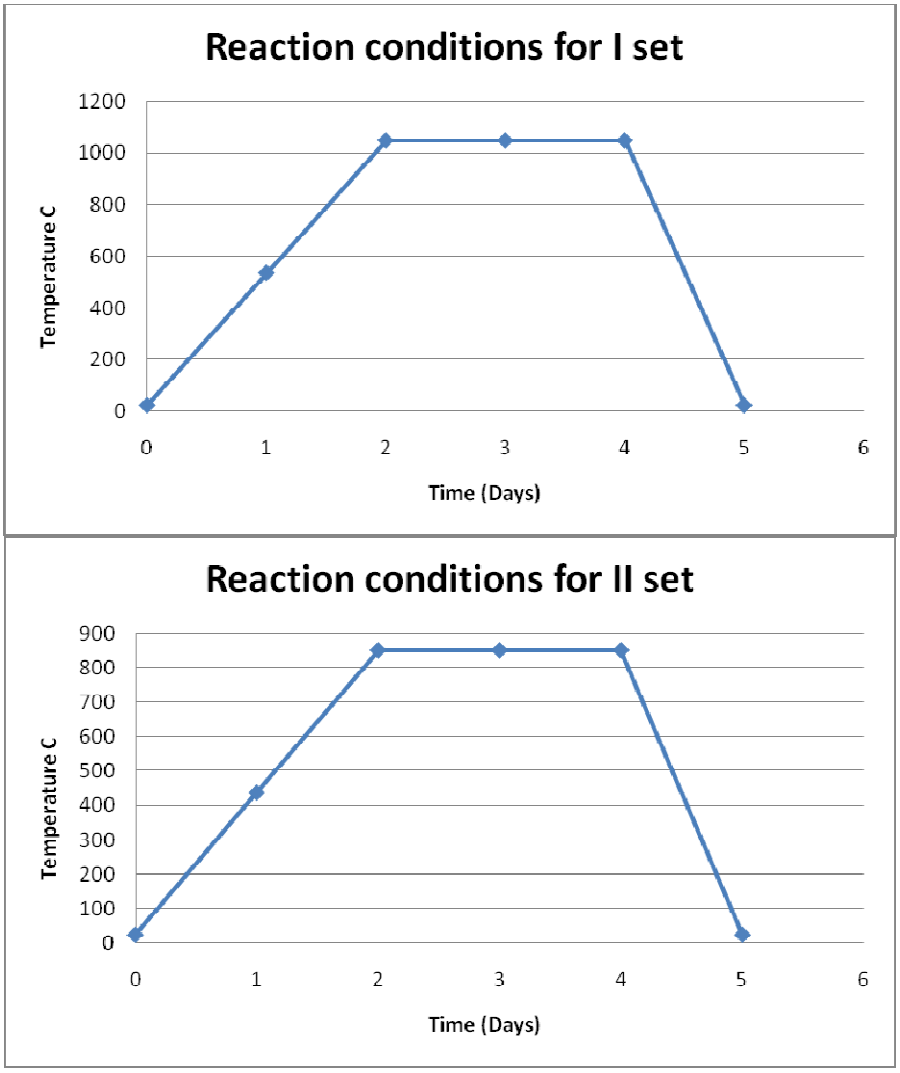

Figure 56. Diagrams of reaction conditions for I and II set

When the synthesis finished, opened reaction ampoules were kept under fume hood for one day in order to eliminate the excess of iodine. SEM analyses of raw material are showed in Fig.57 and Fig.58.

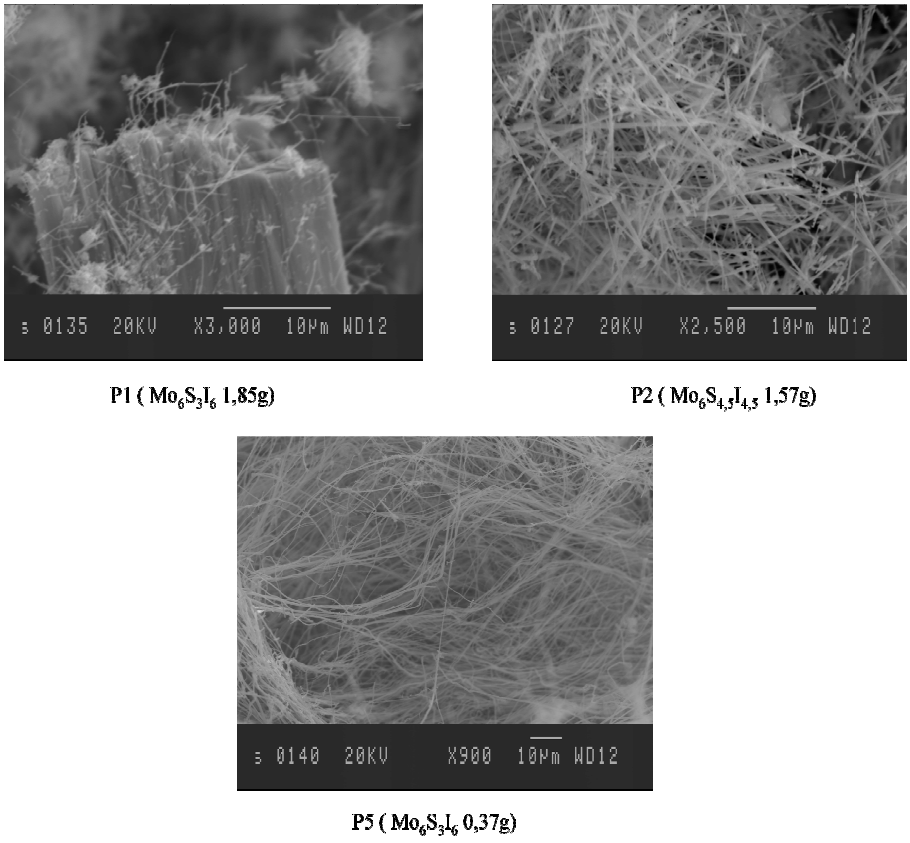

Figure 57. SEM pictures of the raw material of I set

It is possible to see that bundles in samples P1 and P2 are bigger and stiffer than bundles found in other samples. Samples P3 and P4 are constituted by rigid bundles and spherical impurities, while bundles in samples P5 and P6 seem to be thinner and longer than bundles in other samples.

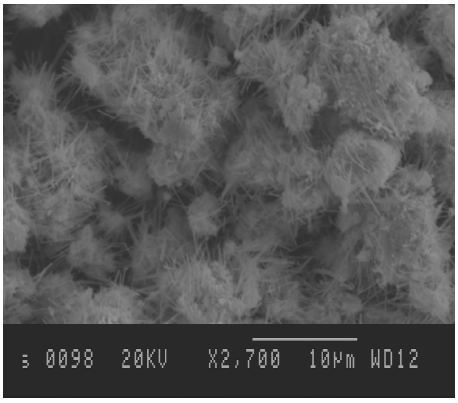

P3 ($Mo_6S_3I_6$ 1,85g)

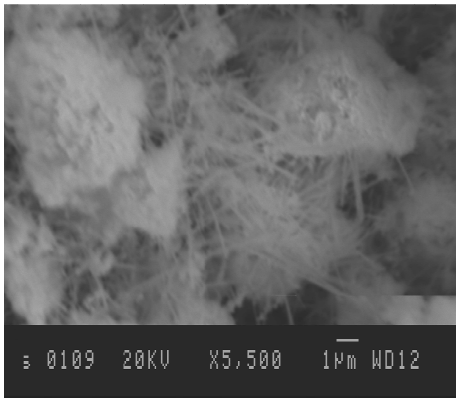

P4 ($Mo_6S_{4,5}I_{4,5}$ 1,57g)

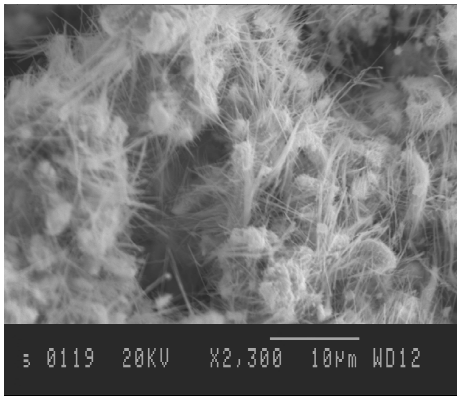

P6 ($Mo_6S_{4,5}I_{4,5}$ 0,31g)

Figure 58. SEM pictures of the raw material of II set

I also correlated the bundles diameter prepared with different parameters with the amount of material put inside the vessel (see fig 59.)

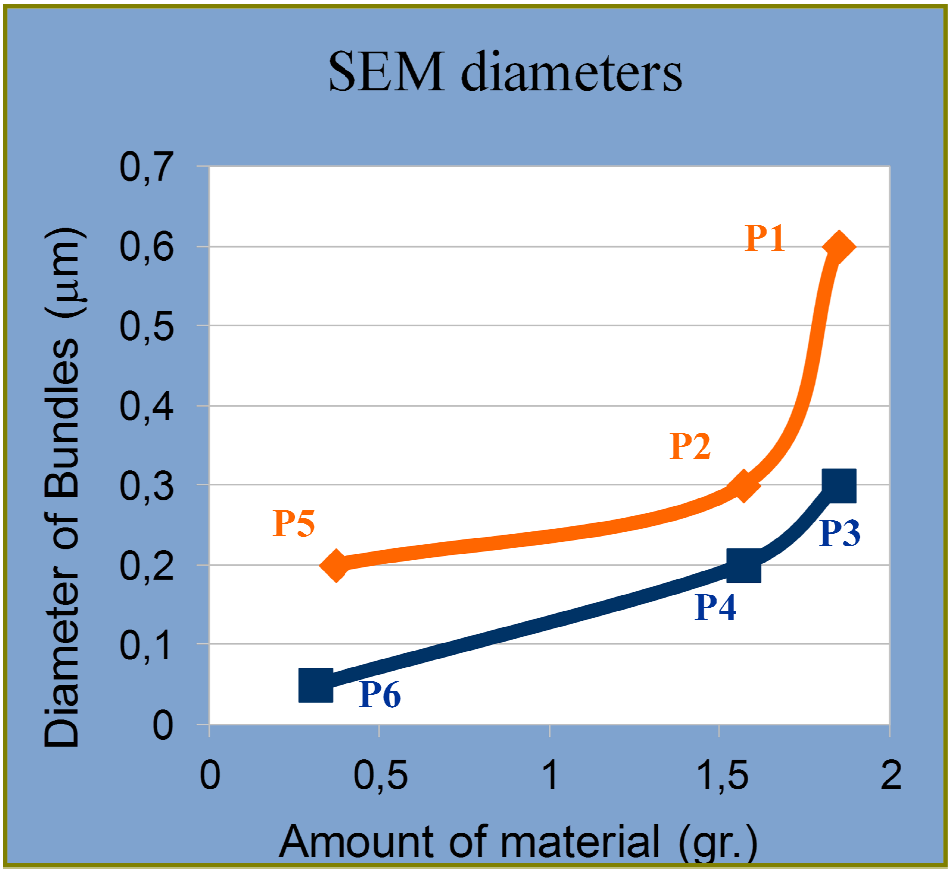

Figure 59. Correlation between bundles diameters and amount of material inside the vessel

First and second sets were dispersed by treatment in a sonic bath for ten minutes, respectively in acetonitrile and IPA, in order to purify systems

from bigger particles, impurities and to extract thinner bundles. Obtained samples were analyzed with SEM and Ultraviolet-Visible Absorption Spectroscopy (UV-Vis).

It is known that the position of the maximum absorption is correlated with the diameter of the bundles in solution Fig. 60. In particular decreases on the absorption wavelength corresponds to a decrease in the diameter of bundles [7].

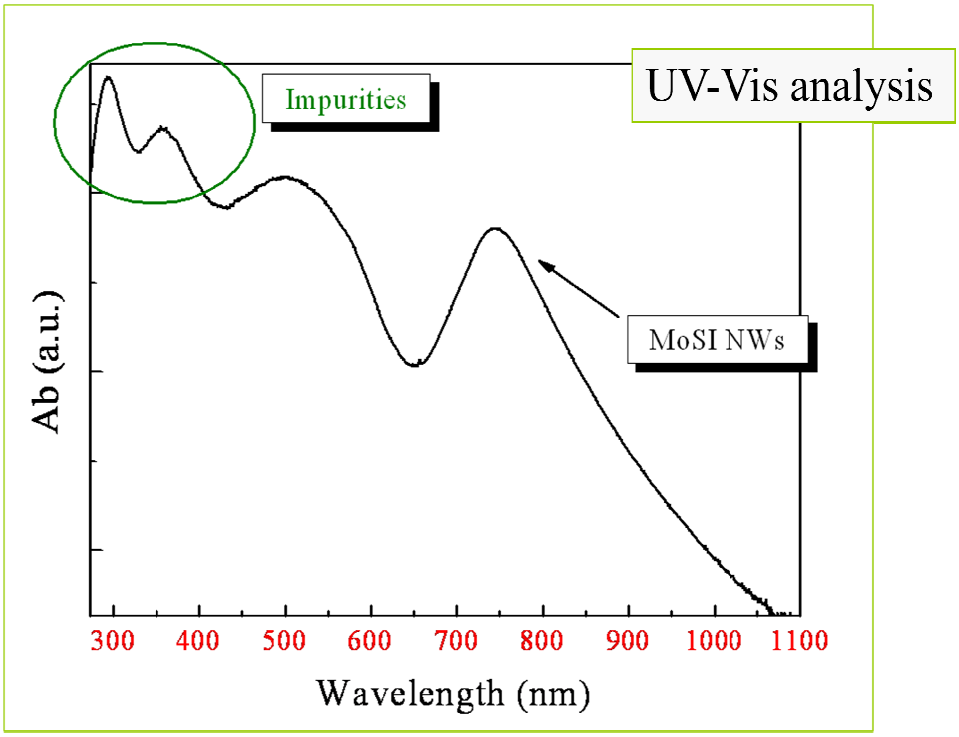

Figure 60. UV analysis of MoSI reported in literature

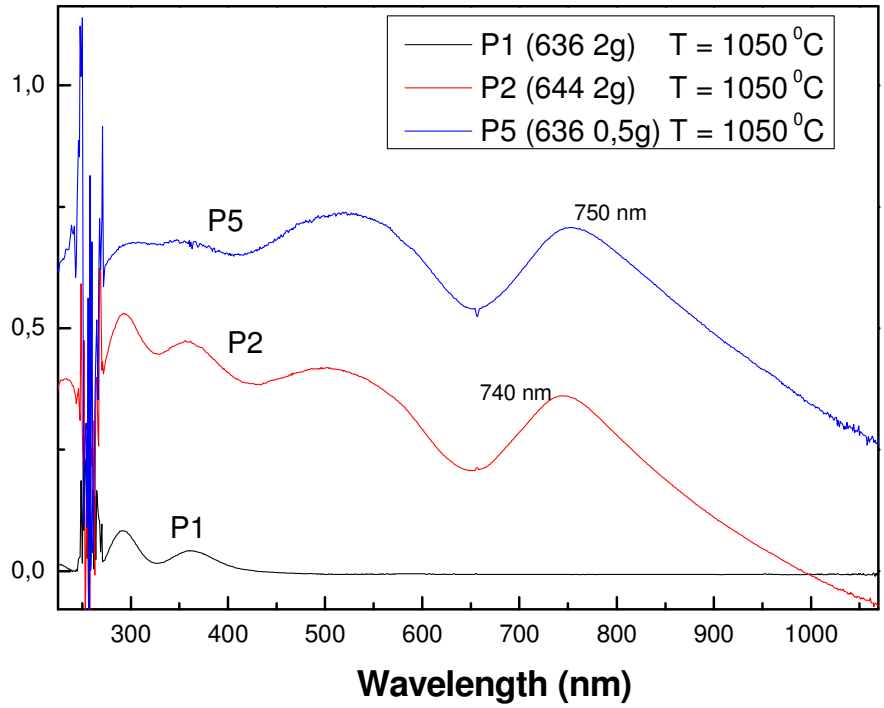

Figure 61. UV-Vis Spectrum of I set dispersed in acetonitril

Analyzing UV spectra fig. 61 and 62 it's possible to know that P1 and P3 don't show the characteristic signals of MoSI dispersed as thin bundles while for the other samples the signals at around 750 nm are present

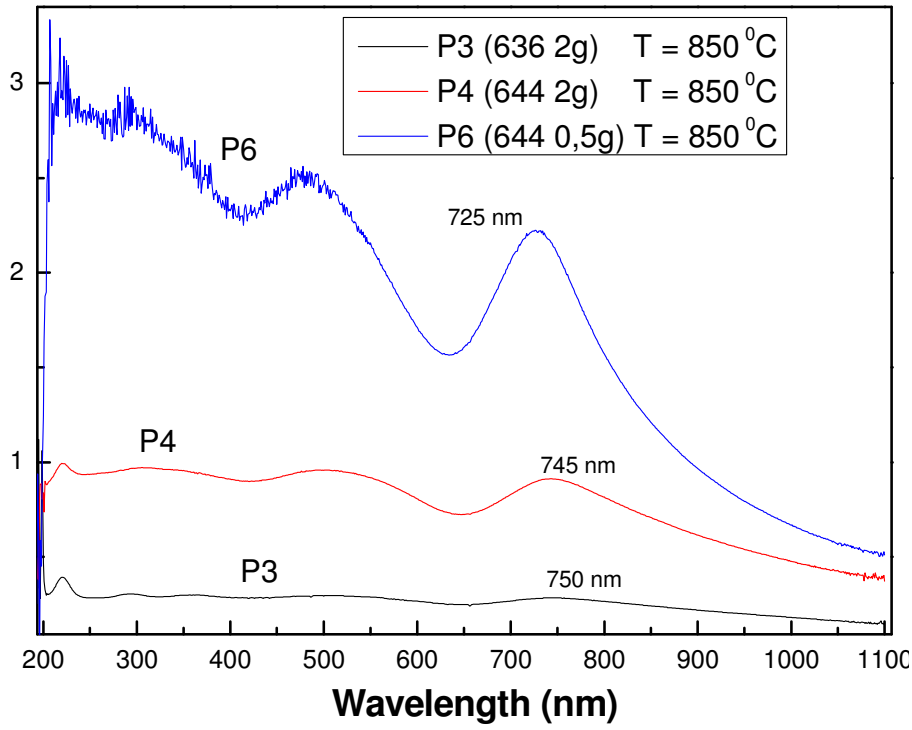

Figure 62. UV-Vis spectrum of II set dispersed in IPA

Moreover UV-Vis spectra shows that only sample P6 presents the characteristic peak of thin bundles at 725 nm, while other samples present a maximum of absorption at higher wavelengths. The presence of peaks at lower wavelengths in samples P1, P2, P3 and P4, shows that a larger amount of starting material inside the reaction vessel produces more impurities. Same considerations can be obtained by SEM analysis of the supernatant after dispersion in solvents. (see Fig.63)

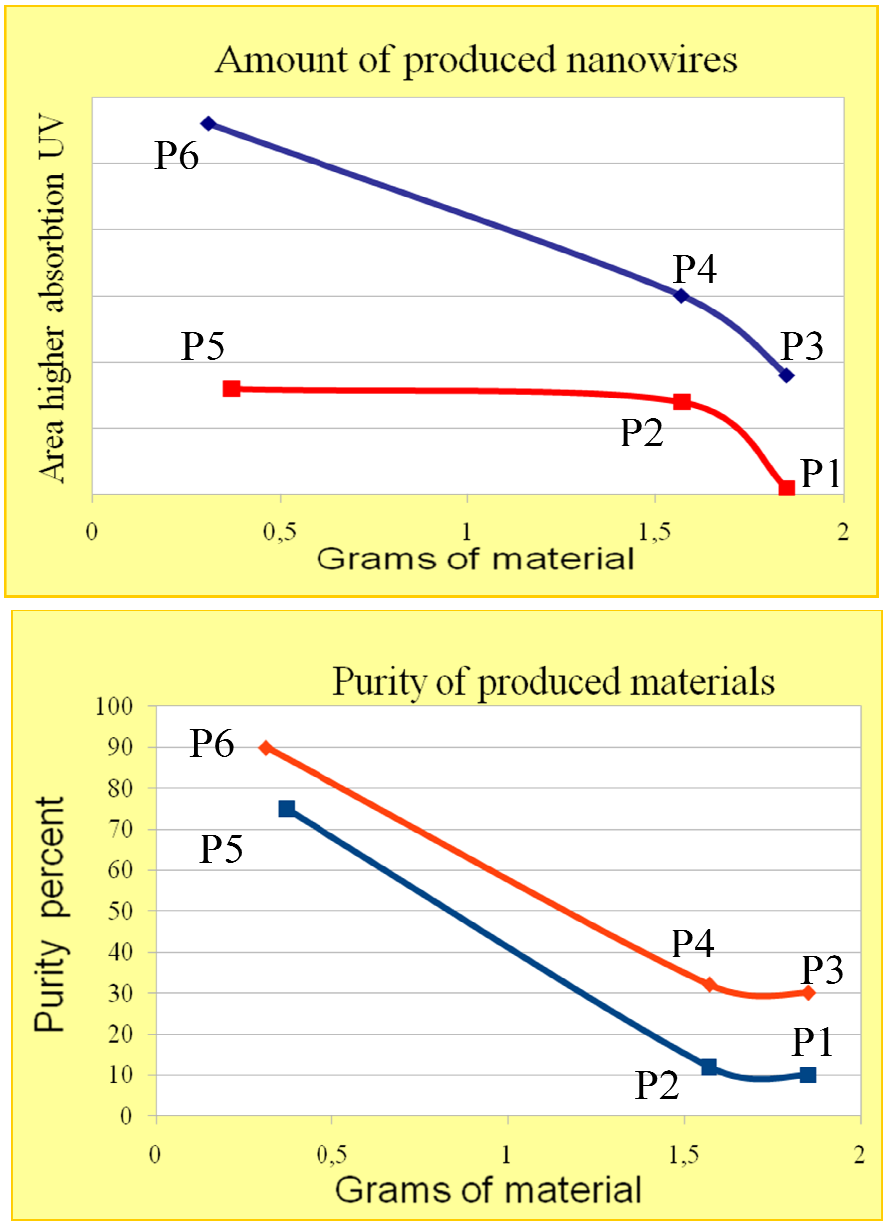

Figure 63. SEM analysis of the supernatant after the dispersion in solvents

In sample P1 there is a low amount of thin bundles, and these present short lengths. Sample P2 contain impurities, while sample P5 show a large amount of thin bundles but also impurities. In the case of the second set of samples, sample P3 presents some short and impure bundles, sample P4 presents impurities and short bundles, while sample P6 is constituted by thin and long bundles of $Mo_6S_{4,5}I_{4,5}$, NWs. So, the best result from these first tries is sample P6, which present large amount of thin bundles without any purification procedure. Moreover a small amount of impurities has been found in the sample. This is an important result because pure samples are required for application in nanoelectronic devices. The best result was obtained with a low concentration of iodine ($Mo_6S_{4,5}I_{4,5}$ instead of $Mo_6S_3I_6$) and a low quantity of material inside the ampoules. After the synthesis of MoSI we focused our attention on the production of gold nanoparticles. This material was prepared by Laser Ablation in liquid (water) using a Nd:YAG laser with a wavelength of 532 nm and with a 5ns pulse duration and a 10-Hz repetition rate. We ablated a gold target at the bottom of a vessel. The ablation time was maintained at around 15 min and the laser beam was focused on the target using a 10 cm focal lens in the same condition reported in figure 19. After 15 min of irradiation a pink solution is obtained. Used fluences ranged between 1 and 10 J/cm^2 in order to test the best production rate. Below TEM images of gold nanoparticles are shown (fig. 64) and it's possible to notice that the average dimension of these particles are fixed around 15 nm.

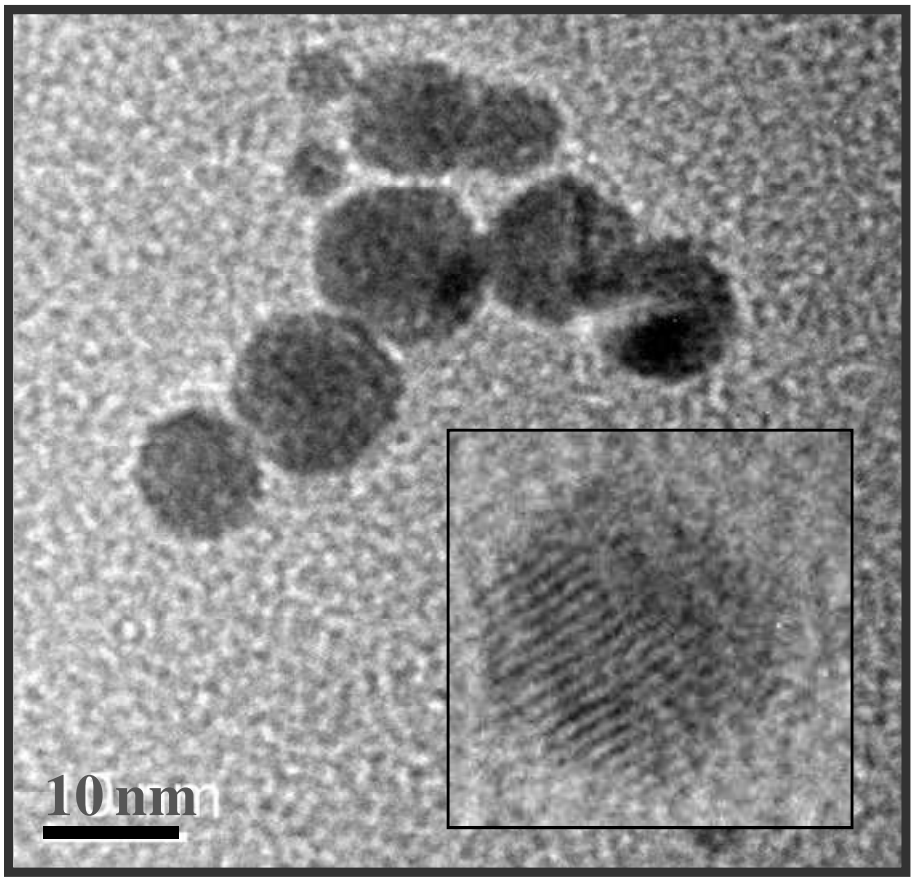

Figure 64. TEM images of gold nanoparticles used for the functionalization

After that we performed the functionalization of systems following the work of Strle et al. [8] in which nano-conductive networks are obtained (fig. 65)

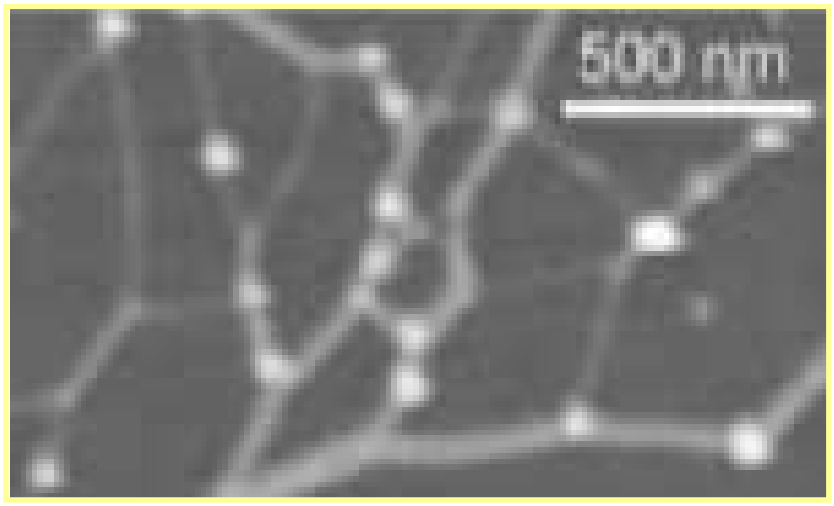

Figure 65. Nano-conductive networks obtained by Strle

In the picture reported above the white spots are made of gold nanoparticles and the lines are MoSI wires.

After the functionalization we studied by XPS the bonding state of each element constituting the nanostructure to verify the predominant interaction between the gold nanoparticles and the sulphur atoms [9].

Figure 66 shows the signals detected at the gold 4f binding energy region for both pure, drop cast GNPs and MoSI@GNPs mixed systems.

The comparison proposed in the figure allows distinguishing of differences between the signals coming from gold nanoparticles deposited onto a silicon substrate and the chemical state of the gold atoms at the surface after the interaction with the $Mo_6S_{4,5}I_{4,5}$ wires.

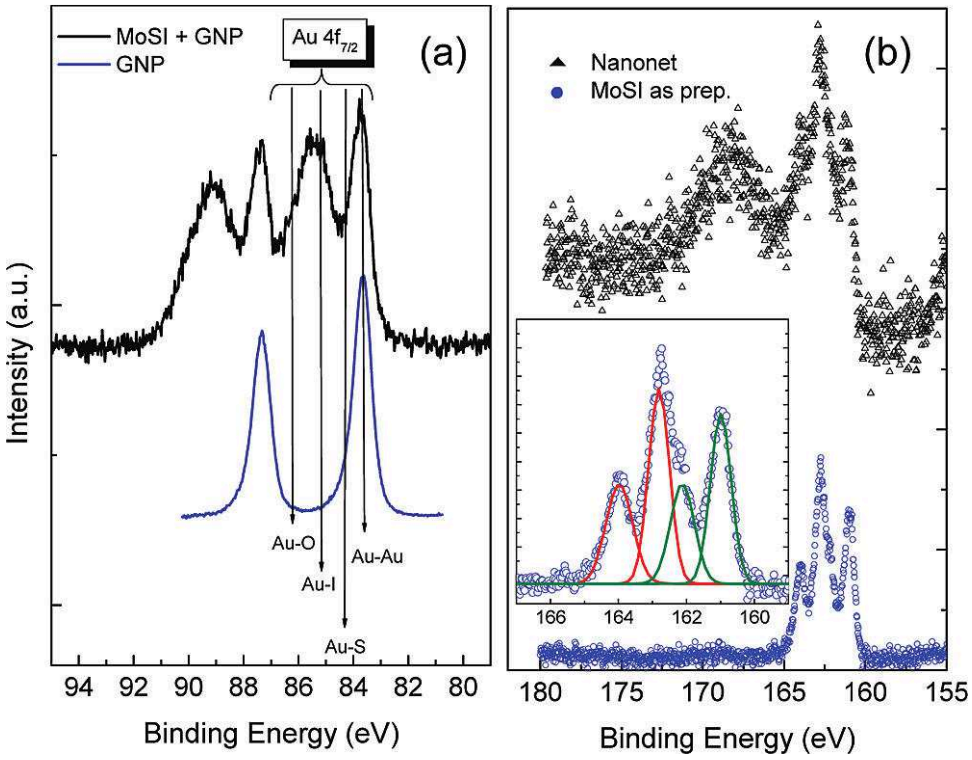

Figure 66. XPS spectra shown in the core Au4f (a) and S2p (b) spectral regions. Here we compare the chemical state for these two elements before and after the formation of the GNPs-NW network

In the first case, only two sharp peaks at 83.7 and 87.4 eV assignable to Au $4f_{7/2}$ and $4f_{5/2}$, respectively, are observed. When interaction between GNPs and MoSI takes place, a second doublet is detected at higher binding energies. This highlights an oxidative interaction between the two systems which can be attributed to the bonding of some gold atoms at the clusters surface with either sulfur or iodine belonging to the nanowire's structure. A survey of the available literature was used to

attribute [10] these components, and we report the suggested binding energies in the Figure 66. We believe that a detailed fitting could have generated confusion and misinterpretation; therefore, we preferred to leave the spectra as taken. Besides the presence of a small fraction of oxidized gold, these results indicate that there is a strong reactivity between MoSI nanowires and gold nanoparticles, as already predicted in previous works using AFM and TEM observations. We would like to point out that the nature of the interaction between the metallic nanoparticles and the nanowire's skeleton could not be exclusively due to Au-S bonds but might also involve iodine atoms constituting the sheath of the nanowire. Moreover, this interaction seems to be quantitatively strong since at least one-half of the Au4f signal is shifted. In principle, the interaction with sulfur should be detected through an investigation of the sulfur core levels, as evidenced in Figure 66b, where the XPS spectra for both the “as-synthesized” and the Au nanowires are shown. The two doublets ($S2p_{1/2}$ and $S2p_{3/2}$; see inset in Figure 66b) shown in the deconvolution can be attributed to the Mo-S bonds occurring in the isolated nanowires as well as to the S-I bonding occurring between the sulfur atoms in the structure of the nanowires and possible residual excess iodine atoms present at the interstitial position within the nanowire bundles.

After the interaction with gold nanoparticles, the spectrum presents less clear and intense features (this is probably due to the decrease in the effective number of bundles available on the substrate) but definitely shows signals which no longer belong to sulfur atoms in the original

bonding state, as suggested by the broad bump located at around 168 eV in binding energy. This signal is generally attributed to sulfuroxidized species such as sulphates. It is important to consider that Au-S signals should fall in a region between 161 and 164 eV, which is in the same region as for the as-synthesized samples. Then, we cannot exclude that such signals could contribute to and overlap with the original MoSI spectral pattern. TEM images reported in figure 67 represent two typical configurations in the network structure. Indeed, each gold nanoparticle appears to be bonded either to the end of the bundles (figure 67a) or to the side of them (figure 67b), allowing an interaction with external iodine atoms to be observed.

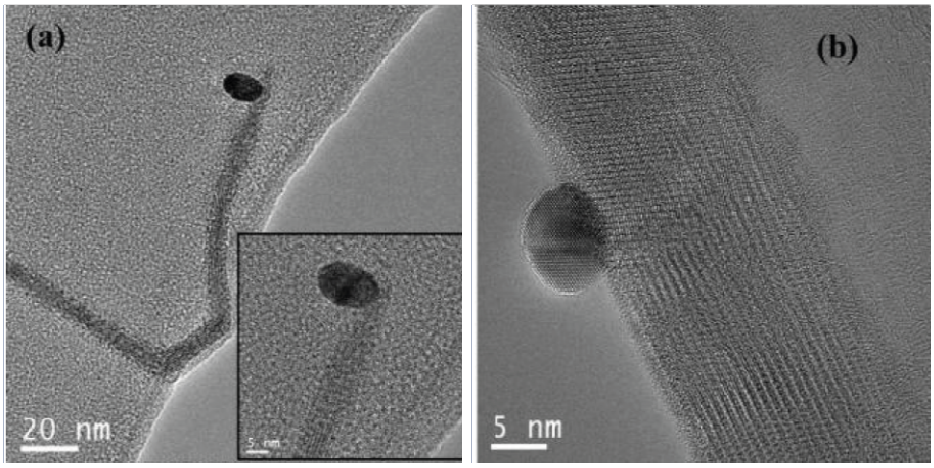

Figure 67. High-resolution TEM images of two typical different bonding configuration after the interaction between gold nanoparticles (a) and a MoSI bundles (b)

The same interaction is spectroscopically evident in Figure 68a, where the I3d core signals are shown. In the case of as synthesized MoSI bundles, two peaks at binding energies of 620.1 and 631.4 eV, corresponding to the iodine $3d_{5/2}$ and $3d_{3/2}$ respectively, are recorded. These are due to the nature of the bonding state(s) of iodine atoms in the nanotube structure. In the same spectrum, an additional doublet, accounting for the presence of I^-, I_2, and I^-_2 coming from residual molecular iodine, was also considered.

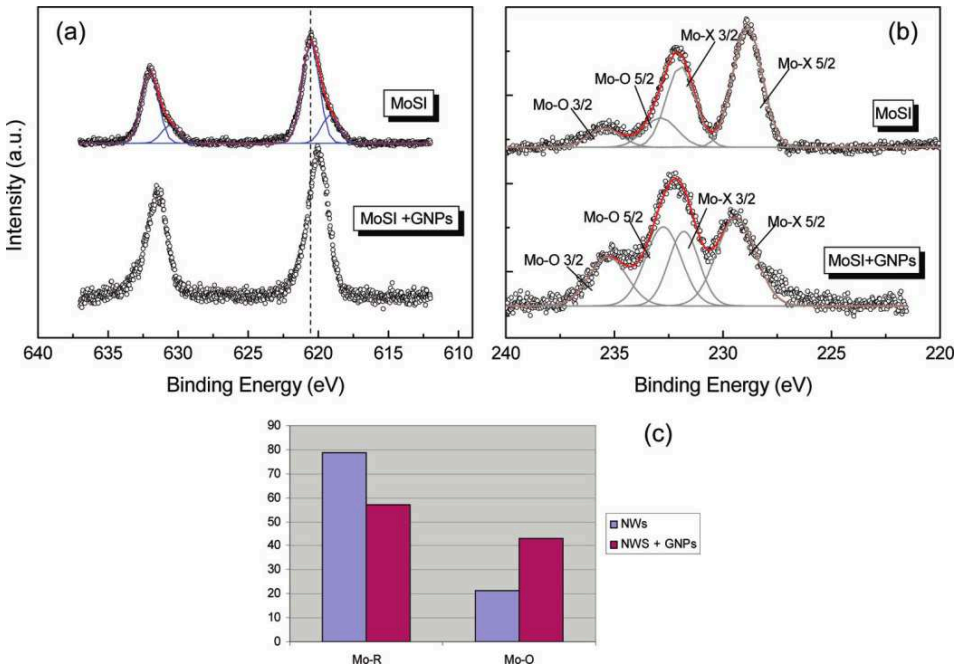

Figure 68. XPS spectra shown in the core I3d (a) and Mo3d (b) spectral regions. This is a comparison before and after the formation of the GNPs-NW network. The histogram (c) shows quantitatively an increased oxidation of the nanowires as a consequence of the interaction

We believe that these impurities can be trapped in each nanowire bundle. In this respect, free iodine molecules should easily sublimate under UHV conditions since the iodine vapor pressure at room temperature is around 0.1 Torr. We also found that the larger the mean bundle size in the sample, the higher the I_2 contribution. This strengthens our trapping hypothesis because larger bundles present many more cavities, as observed by TEM analysis. After the interaction with gold, we observe a consistent shift of the doublet, which reflects an electron enrichment of iodine atoms, related to the interaction with metallic gold, generally considered to be an electron supplier. The signals are also enlarged and present an asymmetric tail toward higher binding energies. Thus, we are led to believe that some nanowires could be partially damaged as a consequence of the network formation. In this respect, note also that the energy of formation for a Au-I bond (average) is lower than that for I-I by about 3.2 kJ/mol and that iodine ions have a different binding affinity to different gold crystalline facets (adsorb preferentially onto [111] facet). [11]. If damage occurs because of the interaction, this should have consequences in the bonding state of molybdenum atoms too, as seen in figure 67b. Molybdenum has $3d_{5/2}$ and $3d_{3/2}$ spin-orbit split contribution. In the case of the $Mo_6S_{4,5}I_{4,5}$ nanowires, molybdenum atoms are bonded with both iodine and sulfur, and this gives contributions in the range around 228 ($3d_{5/2}$) and 230 eV ($3d_{3/2}$). In the case of the as-prepared samples, this doublet contributes to 87% of the total Mo 3d signal, suggesting that the majority of Mo atoms have the same bonding configuration. Two smaller spin-split Mo 3d peaks, (13% of the signal)

observed at 228.9 and 231.9 eV can be attributed to $(Mo_6I_8)I_4$ clusters or to MoO_x impurities ($x \approx 3$). Once the interaction with GNPs occurs, the higher-energy component increases in intensity because of the above-mentioned degradation. The relative amount of oxidized molybdenum species is reported in figure 68c. We readily observe that the interaction of the bundles with gold clusters is responsible for the degradation of a part of the network. This is clear looking at the oxidation of molybdenum and sulfur components (Figures 66 and 68), and the exposure can be ascribed to atmospheric oxygen, possibly mediated by catalytic action of metal nanoparticles, in agreement with the well known catalytic effect of nano-Au on oxidation kinetics. Work is in progress to evaluate the kinetic of this process and to understand the mechanisms.

REFERENCES

[1] Mihailovic et al. *Progress in Material Science* (2009), **54**, 309-350

[2] Sun et al. *Analytical Chemistry* (2008), **80**, 3593-3597

[3] Meden et al. *Nanotechnology* (2005), **16**, 1578-1583

[4] McCarthy et al. *Journal of Applied Physics* (2007), **101**, 014317-014327

[5] Ploscaru et al. *Nano Letters* (2007), **7**, 1445-1448

[6] Lago-Fernandez et al. *Physical Review Letters* (2000), **84**, 2758-2761

[7] Vengust et al. *Synthetic Metals* (2010) , **160**, 2389-2392

[8] Strle et al. *Nano Letters* (2009), **9**, 1091-1095

[9] Compagnini et al. *Journal of Physical Chemistry Letters* (2010), **1**, 393-397

[10] Buttner et al. *Thin Solid Films* (2006), **495**, 180-185

[11] Grzelczak et al. *Advanced Functional Materials* (2008), **18**, 3780-3786

5 Conclusion

During my PhD thesis I worked to employ the synthesis of 2D nanostructures in order to promote some methods faster, easier and cheaper than the standard synthesis routes avoiding, moreover, the using of some dangerous reagents, for instance H_2S flow in the standard synthesis of IF-MoS_2.

In particular pulsed laser ablation of a polycrystalline MoS_2 target in water at room temperature allows the production of fullerene-like MoS_2 nanostructures in a safe, cheap and fast way. As demonstrated by TEM, EFTEM and XPS analyses, these nanostructures are formed together with a predominant formation of molybdenum oxide (MoO_3) and oxysulphate. A large quantity of external sulphur is evidenced, which is probably present in the form of polymeric sulphur with sulphate groups at the end of the chains. We have indicated that the MoO_3 formation plays a crucial role for the IF-MoS_2 production. In fact, the same experiment performed in an oxygen-free liquid (n-decane) reveals that no MoS_2 nanostructures are evidenced by the XPS analysis, while purging water using nitrogen the formation of oxides is limited as well as that of IF-MoS_2. Indeed ablation of MoS_2 targets in a poor oxidant medium (i.e. in water N_2 fluxed) leads to the formation of small quantity of Mo species, most of which are present in intermediate oxidation states.

I also worked on the exfoliation of MoS_2 in water and solvents environmental friendly to avoid the using of intercalators, like Lithium,

producing few-layers material dispersed in water and ready to manipulation in different application field.

In the case of CNWs we have combined the production of carbon units at the atomic/molecular level and the transport efficiency typical of electrophoretic experiments in a unique manner in order to obtain CNWs under atmospheric conditions. Compared to CVD based methods, the current approach has a simple and economic experimental setup and open new possibilities for scalable depositions ranging from large surface areas to the use on patterned electrodes.

In the field of functionalization, in the frame of a possible application of GNPs-MoSI nanonets in molecular-scale devices, we have studied the nature of bonds between GNPs and MoSI bundles after the network formation process. As a first consideration, we observed that the chemical interaction between the nanowire's structure and the metal nanoparticles is much heavier than that suggested a by simple microscopic recognition. Besides the formation of oxidized species with the partial degradation of the nanowires, we observed a peculiar interaction with sulfur and iodine, which could be of crucial importance for a correct use of the networks in applications where the electronic system plays a crucial role.

6 Future work

In the field of functionalization I'm employing the alternative method to functionalize CNWs with metallic nanoparticles, for instance silver, copper, for the application for SERS analysis.

SERS is a powerful surface technique that affords molecular specificity and extraordinary sensitivity for single-molecule detection [1]. SERS can amplify weak Raman signals by many orders of magnitude and can identify, in a nondestructive manner, biological and chemical materials. Recent studies have produced significant employments in designing SERS substrates in order to obtain fundamental understanding into this enhancement phenomenon. The most part of the recent SERS work has been conducted on Ag or Au films, chemical modification of substrate roughness or nanoparticle aggregations, which facilitate large enhancements of Raman scattering signals from labels that are in close proximity to noble metal surfaces [2]. In the work of Rout et al. [3], they report a new underlying SERS substrate, CNWs, that provides further enhancement.

The fundamental SERS effect is probably caused by the excitation of surface plasmon resonances on the metal surface that greatly strengthen the local electric field. To carry out ultrasensitive detection of molecules by SERS, the substrates should possess high surface area to adsorb molecules and should have a large density of 'hot spots' comprised of metal nanostructures to enhance the electric field [4]. SERS-active

surfaces can be produced by different procedures like electrochemical roughening of metal foils [5], nanosphere lithography followed by metal deposition [6], and self-assembled surface nanoparticles [7]. However, most SERS substrates, used in antecedent works, presents inconsistent surface area and for this reason give either limited sensitivity or nonreproducible and unstable Raman signals. Therefore, a further progress in improving the sensitivity and reproducibility of SERS substrates is necessary. Graphene, a single-atom-thick and two-dimensional honeycomb carbon lattice has attracted the attention of many researchers for its conspicuous electronic, mechanical and thermal properties [8]. Also, fewlayer graphene, thanks to its easily modified structure, can give a useful platform for studying the chemical enhancement in SERS and furthermore it can facilitate electron transfer with adsorbed surface molecules [9]. It's know that several characteristic properties of graphene can be enhanced if this material forms a heterojunction with noble metals, [10]. Similarly, CNWs, made of graphene layers, have potential application in energy storage [11-12] field emission [13-14] and electrodes for fuel cells [15]. The large surface area of aligned CNWs creates an ideal template for the fabrication of other nanostructured materials.

In the work of Rout et al. [3] they synthesized CNWs on flat Ti-coated Si(100) substrates which cleaned with acetone were placed in the chamber on an Mo puck and were kept at a height of 6 mm from the puck surface by ceramic spacers. Uniform growth of CNWs was obtained under microwave plasma chemical vapor deposition (MPCVD)

conditions of H_2 (50 sccm) and CH_4 (10 sccm), as the primary feed gases, at 30 Torr total pressure and 700 W plasma power with 900 °C substrate temperature.

CNWs were functionalized by electro-deposition of Ag by oxygen plasma treatment using inductively coupled plasma at a radio frequency of 13.56 MHz at 50 sccm (cubic centimeter per minute at STP) oxygen flow rate and gas pressure of 60 mTorr for 15 s.

In figure 69 it's shown field emission scanning electron microscopy (FESEM) images of the Ag-decorated CNWs after an increasing number of electro-deposition cycles. For 50 cycles, we can observe a homogeneous distribution of discrete and spherical Ag nanoparticles with diameters near 30 nm on the nanowalls with no agglomeration (figure 69(a)). On increasing the number of electro-deposition cycles to 100, the Ag nanoparticles grow larger, with diameters in the range 100–150 nm (figure 69(b)). Nanoparticle agglomerates were observed above 200 cycles of electro-deposition, as observed in figures 69(c) and (d). The shapes of nanostructured crystals depend by the driving force of crystallization and the rate of diffusion of reactants, as shown in figures 69(c) and (d).

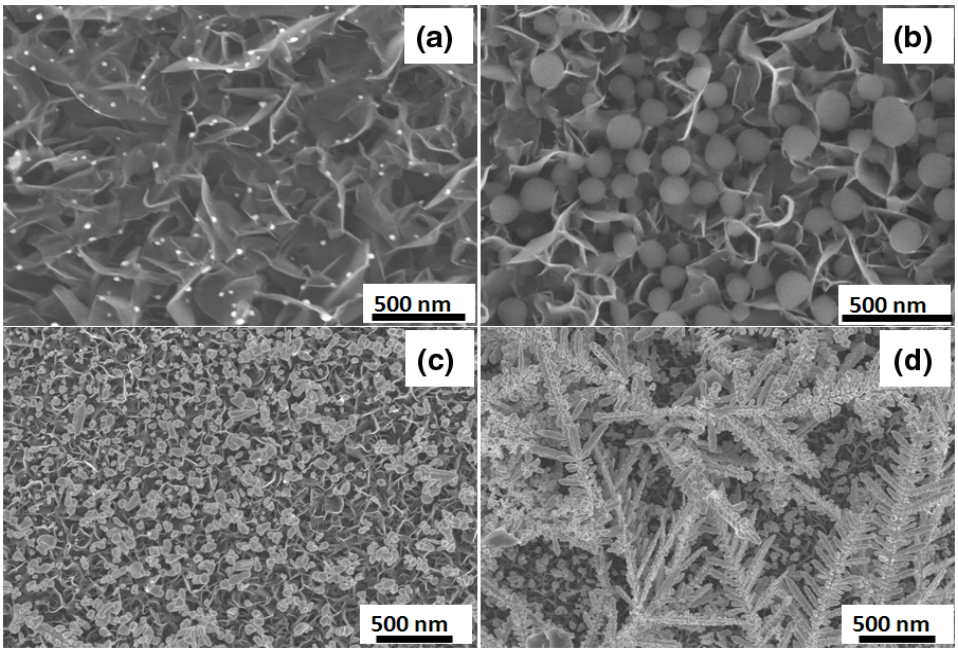

Figure 69. FESEM images of Ag-electrodeposited CNWs for (a) 50 cycles, (b) 100 cycles, (c) 200 cycles and (d) 300 cycles

In figure 70 are reported raman spectra of uncovered (a) and Ag-decorated nanowalls (b). From the comparison between raman peaks it's possible to notice that D peak in the case of Ag decorated is stronger that the case of CNWs without nanoparticles. The D-peak is attributed at the disorder of the system and for this reason a possible explanation for this behavior relates to the strengthening of the C–C bond because of the additional electron density provided by nanoparticles [16-17]

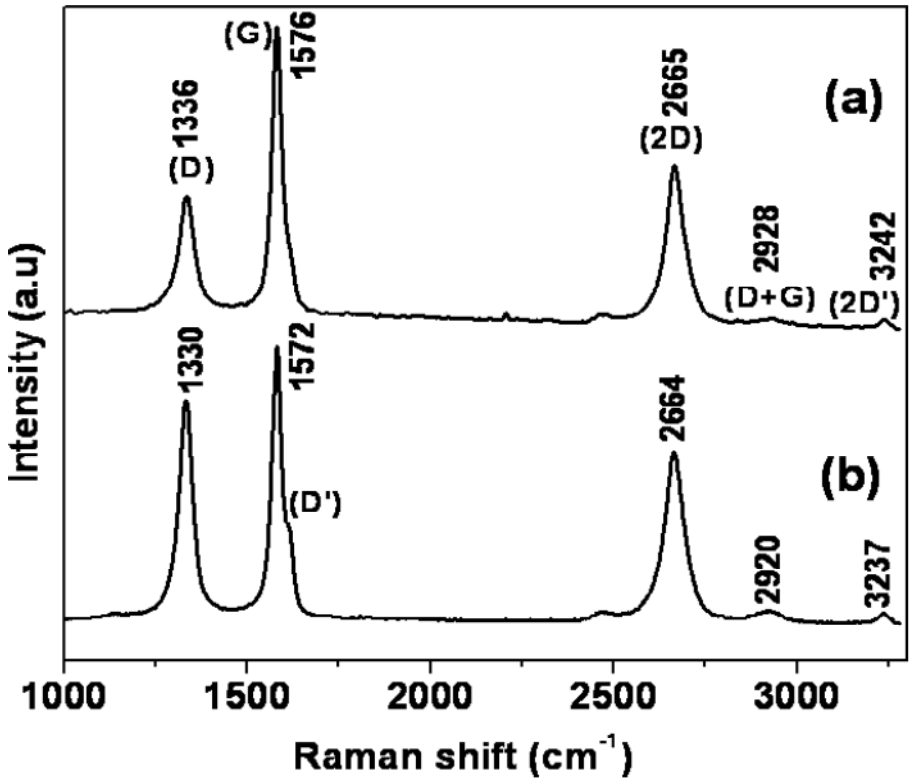

Figure 70. Raman spectra of (a) CNWs and (b) Ag nanoparticles decorated CNWs

After that the authors made some test on the SERS effects of this substrate and the relative Raman spectra are reported in figure 71.

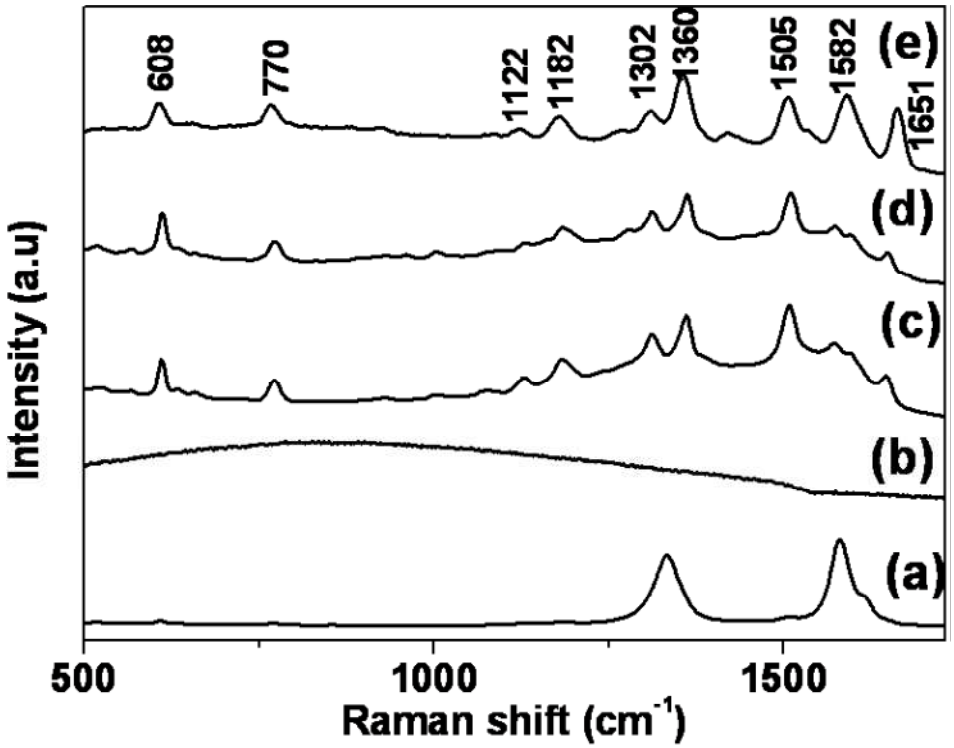

Figure 71. Raman spectra of 10−7 M R6G on (a) CNWs, (b) Ag deposited HOPG. Raman spectra of (c) 10−6 M, (d) 10−7 M and (e) 10−8 M R6G on Ag-decorated CNWs

The molecule test was the R6G molecule for SERS studies, because this shows a molecular resonance Raman effect when excited into its visible absorption band [18]. Analyzing the figure 71 it's clear that in the case of pure CNWs we can't observe SERS effect (spectrum a) while we notice it in the spectra c-d-e. This spectra are obtained by varying R6G concentrations (10^{-6}, 10^{-7} and 10^{-8} M) on Ag-decorated CNWs.

At lower concentrations, relatively intense SERS peaks were observed as compared to those for the more highly concentrated R6G solutions. The SERS results confirm that Ag-decorated nanowalls create a hybrid SERS substrate for detecting R6G as low as 10^{-8} M, a level that is difficult to detect through conventional Raman spectroscopy.

During my last period of PhD I tried to produced this SERS substrate using the PLAL with a electric field and I have been able to synthesized this nanostructures in an analogue method using for the formation of CNWs previously discussed.

I used PLAL to produce the building blocks, polyynes, for the growth of CNWs on the electrodes and after the synthesis I used silver electrodes instead of graphite electrodes. During the application of electric field the positive electrode, made of silver, undergoes an oxidation and silver ions move in solution. Polyynes and silver ions interacting each other grown on negative electrode producing CNWs silver decorated as reported in fig. 72.

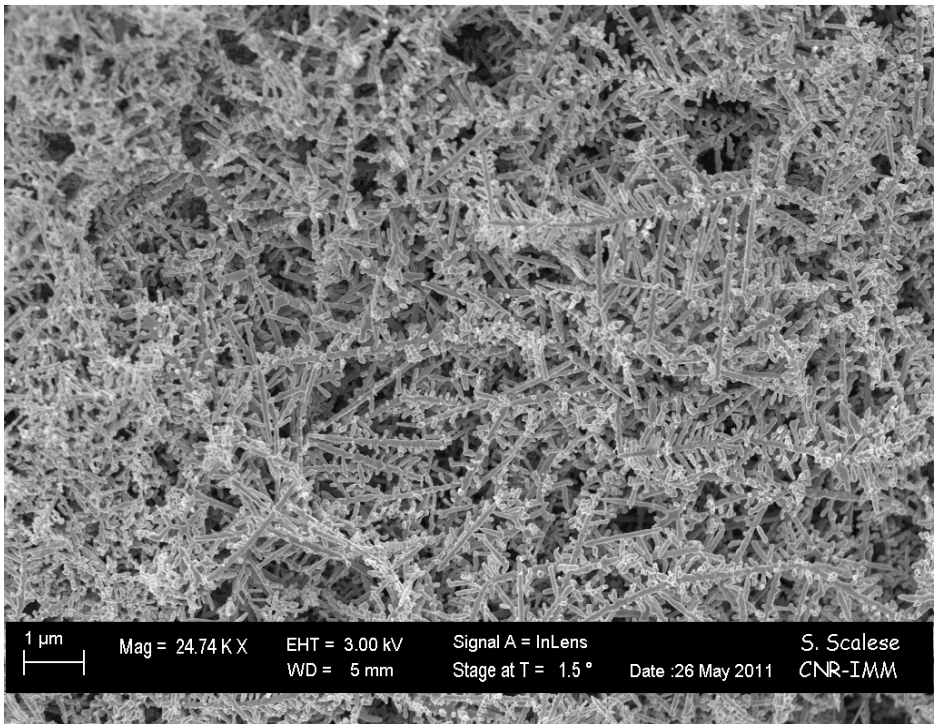

Figure 72. SEM analysis of negative electrode after the deposition through electric field

We also performed XPS analysis to verify the successful functionalization and indeed we noticed the formation of a component in the silver signals due to the formation of the bond between Ag-C (fig. 73).

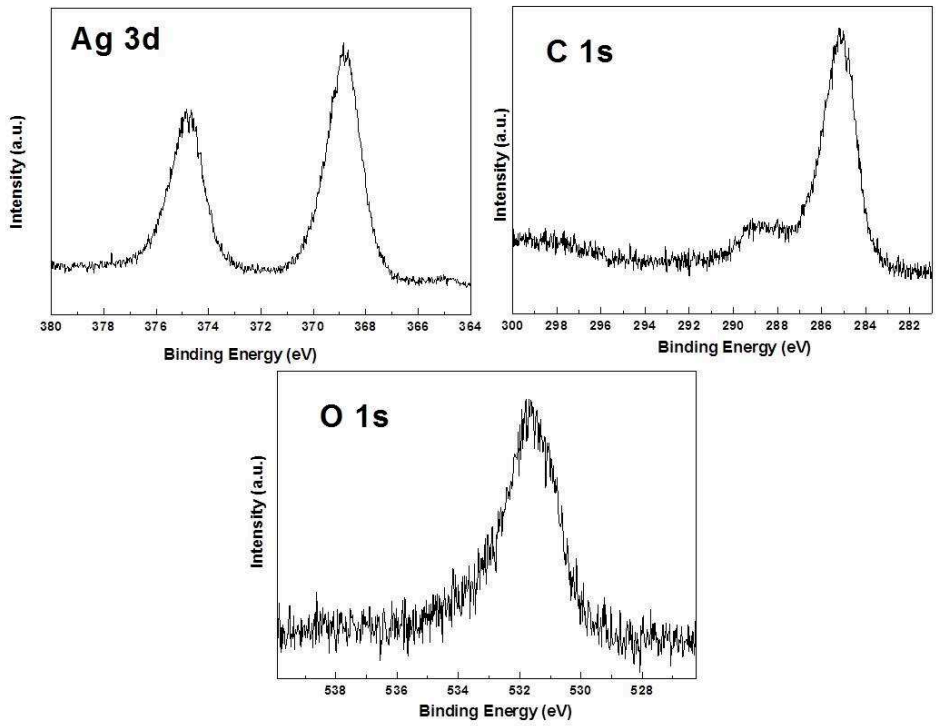

Figure 73. XPS analysis of CNWs decorated with silver nanoparticles

Also carbon signal present the component relative to the bond C-Ag. To perform the study SERS we have to find a way to remove CNWs-Ag from the electrode because the electrode, made of Ag after electro-deposition is already a SERS substrate and for this reason we have to separate two systems each other but this step is under investigation.

REFERENCES

[1] Alivisatos et al. *Nature Biotechnology* (2004), **22**, 47-52

[2] Albrecht et al. *Journal of American Chemistry Society* (1977), **99**, 5215-5217

[3] Rout et al. *Nanotechnology* (2011), **22**, 395704-1-395704-8

[4] Garcia et al. *Physical Review Letters* (1996), **77**, 1163-1166

[5] Jeanmaire et al. *Journal of Electroanalytical Chemistry* (1977), **84**, 1-20

[6] Sugawara et al. *Physical Review Letters* (2006), **97**, 266808-1-266808-4

[7] Freeman et al. *Science* (1995), **267**, 1629-1632

[8] Wu et al. *Chemistry Review* (2007), **107**, 718-747

[9] Yu X et al. *ACS Nano* (2011), **5**, 952-958

[10] Goncalves et al. *Chemistry of Materials* (2009), **21**, 4796-4802

[11] Hung et al. *Electrochemistry of Solid State Letters* (2009), **12**, K41-K44

[12] Tao et al. *European Journal of Inorganic Chemistry* (2010), 4314-4320

[13] Wang et al. *Applied Physical Letters* (2004), **85**, 1265-1267

[14] Srivastava et al. *Thin Solid Films* (2005), **492**, 124-130

[15] Tanaike et al. *Solid State Ionics* (2009), **180**, 381-385

[16] Yeh et al. *Journal of Nanotechnology* (2009), 217469-1-217469-7

[17] Kim et al. *Chemical Communication* (2010), **46**, 3185-3190

[18] Hassell et al. *Advanced Functional Materials* (2008), **18**, 1262-1265